Julius-Maximilians-
UNIVERSITÄT
WÜRZBURG

Single-molecule fluorescence microscopy in live *Trypanosoma brucei* and model membranes

Dissertation zur Erlangung des naturwissenschaftlichen
Doktorgrades der Julius-Maximilians-Universität Würzburg

vorgelegt von

Marius Glogger

geboren in Frankenthal

Würzburg, 2018

Eingereicht am:

Mitglieder der Promotionskommission:

Vorsitzender:

1. Gutachterin: Dr. Susanne Fenz

2. Gutachter: Prof. Dr. Markus Sauer

Tag des Promotionskolloquiums:

Doktorurkunde ausgehändigt am:

Contents

Summary

The eukaryotic parasite *Trypanosoma brucei* has evolved sophisticated strategies to escape the host immune response and maintain a persistent infection inside a host. One central feature of the parasite's defense mechanism relies on the shielding function of their surface protein coat. This coat is composed of a dense arrangement of one type of glycosylphosphatidylinositol (GPI)-anchored variant surface glycoproteins (VSGs) which impair the identification of epitopes of invariant surface proteins by the immune system. In addition to the importance of understanding the function of the VSG coat and use it as a potential target to efficiently fight the parasite, it is also crucial to study its biophysical properties as it is not yet understood sufficiently. This is due to the fact that microscopic investigations on living trypanosomes are limited to a great extent by the intrinsic motility of the parasite. In the present study, state-of-the-art single-molecule fluorescence microscopy (SMFM) is introduced as a tool for biophysical investigations in the field of trypanosome research. The work encompasses studies of VSG dynamics under the defined conditions of an artificial supported lipid bilayer (SLB). First, the impact of the lateral protein density on VSG diffusion was systematically studied in SLBs. Ensemble fluorescence after photobleaching (FRAP) and complementary single-particle tracking experiments revealed that a molecular crowding threshold (MCT) exists, above which a density dependent decrease of the diffusion coefficient is measured. A relative quantification of reconstituted VSGs illustrated that the VSG coat of living trypanosomes operates very close to its MCT and is optimized for high density while maintaining fluidity. Second, the impact of VSG N-glycosylation on VSG diffusion was quantitatively investigated. N-glycosylation was shown to contribute to preserving protein mobility at high protein concentrations. Third, a detailed analysis of VSG trajectories revealed that two distinct populations of freely diffusing VSGs were present in a SLB, which is in agreement with the recent finding, that VSGs are able to adopt two main structurally distinct conformations. The results from SLBs were further complemented by single-particle tracking experiments of surface VSGs on living trypanosomes. A high mobility and free diffusion were measured on the cell surface, illustrating the overall dynamic nature of the VSG coat. It was concluded that the VSG coat on living trypanosomes is a protective structure that combines density and mobility, which is supported by the conformational flexibility of VSGs. These features are elementary for the persistence of a stable infection in the host.

Different hydrogel embedding methods are presented, that facilitated SMFM in immobilized, living trypanosomes. The hydrogels were found to be highly cytocompatible for one hour after cross-linking. They exhibited low autofluorescence properties in the spectral range of the investigations, making them suitable for super-resolution microscopy (SRM). Exemplary SRM on living trypanosomes illustrated that the hydrogels efficiently immobilized the cells on the nanometer lever. Furthermore, the plasma membrane organization

was studied in living trypanosomes. A statistical analysis of a tracer molecule inside the inner leaflet of the plasma membrane revealed that specific membrane domains exist, in which the tracer appeared accumulated or diluted. It was suggested that this distribution was caused by the interaction with proteins of the underlying cytoskeleton.
In conclusion, SMFM has been successfully introduced as a tool in the field of trypanosome research. Measurements in model membranes facilitated systematic studies of VSG dynamics on the single-molecule level. The implementation of hydrogel immobilization allowed for the study of static structures and dynamic processes with high spatial and temporal resolution in living, embedded trypanosomes for the first time.

Zusammenfassung

Der eukaryotische Parasit *Trypanosoma brucei* hat komplexe Strategien entwickelt um der Immunantwort eines Wirtes zu entkommen und eine persistente Infektion innerhalb dessen aufrechtzuerhalten. Ein zentrales Element seiner Verteidigungsstrategie stützt sich auf die Schutzfunktion seines Proteinmantels auf der Zelloberfläche. Dieser Mantel besteht aus einer dichten Schicht aus identischen, Glykosylphosphatidylinositol (GPI)-verankerten variablen Oberflächenglykoproteinen (VSG). Der VSG Mantel verhindert die Erkennung der darunterliegenden, invarianten Epitope durch das Immunsystem. Obwohl es notwendig ist die Funktionsweise des VSG Mantels zu verstehen, vor allem um ihn als mögliches Angriffsziel gegen den Parasiten zu verwenden, sind seine biophysikalischen Eigenschaften bisher nur unzureichend verstanden. Dies ist vor allem der Tatsache geschuldet, dass die hohe Motilität der Parasiten mikroskopische Studien in lebenden Zellen bisher weitestgehend verhinderten.

In der vorliegenden Arbeit wird nun hochmoderne Einzelmolekül-Fluoreszenzmikroskopie (EMFM) als Möglichkeit für mikroskopische Untersuchungen im Forschungsbereich der Trypanosomen vorgestellt. Die Arbeit umfasst Untersuchungen der VSG Dynamik unter definierten Bedingungen künstlicher Membransysteme. Es wurde zuerst der Einfluss der lateralen Proteindichte auf die VSG Diffusion untersucht. Experimente mittels Fluoreszenz-Wiederkehr nach irreversiblem Photobleichen und komplementäre Einzelmolekül-Verfolgungs Experimente offenbarten, dass ein molekularer Diffusionsschwellenwert existiert. Über diesem Schwellenwert wurde eine dichteabhänige Reduzierung des Diffusionskoeffizienten gemessen. Eine relative Quantifizierung der rekonstituierten VSGs verdeutlichte, dass der Oberflächenmantel der Trypanosomen sehr nahe an diesem Schwellenwert agiert. Der VSG Mantel ist optimiert um eine hohe Proteindichte bei gleichzeitiger hoher Mobilität der VSGs zu gewährleisten. Des Weiteren wurde der Einfluss der VSG N-Glykosylierung auf die Diffusion des Proteins quantitativ untersucht. Die Messungen ergaben, dass die N-Glykosylierung dazu beiträgt eine hohe Mobilität bei hohen Proteindichten aufrechtzuerhalten. Eine detaillierte Analyse von VSG Trajektorien offenbarte, dass zwei unterschiedliche Populationen frei diffundierender VSGs in der künstlichen Membran vorlagen. Kürzlich wurde entdeckt, dass VSGs zwei strukturell unterschiedliche Konformationen annehmen können. Die Messungen in der Arbeit stimmen mit diesen Beschreibungen überein.

Die Ergebnisse der EMFM in künstlichen Membranen wurden durch VSG Einzelmolekül-Verfolgungs Experimente auf lebenden Zellen ergänzt. Es wurde eine hohe Mobilität und Dynamik einzelner VSGs gemessen, was die allgemein dynamische Natur des VSG Mantels verdeutlicht. Dies führte zu der Schlussfolgerung, dass der VSG Mantel auf lebenden Trypanosomen ein dichter und dennoch dynamischer Schutzmantel ist. Die Fähigkeit der VSGs ihre Konformation flexibel anzupassen, unterstützt das Erhalten der

Fluidität bei variablen Dichten. Diese Eigenschaften des VSG Mantels sind elementar für die Aufrechterhaltung einer presistenden Infektion eines Wirtes.
In dieser Arbeit werden des Weiteren verschiedene, auf Hydrogel basierende Einbettungsmethoden vorgestellt. Diese ermöglichten die Zellimmobilisierung und erlaubten EMFM in lebenden Trypanosomen. Die Hydrogele wiesen eine hohe Zytokompatibilität auf. Die Zellen überlebten in den Gelen für eine Stunde nach Beginn der Immobilisierung. Die Hydrogele erfüllten die Anforderungen der Superresolution Mikroskopie (SRM) da sie eine geringe Autofluoreszenz im Spektralbereich der verwendeten Fluorophore besaßen. Mittels SRM konnte nachgewiesen werden, dass die Hydrogele die Zellen effizient immobilisierten. Als erstes Anwendungsbeispiel der Methode wurde die Organisation der Plasmamembran in lebenden Trypanosomen untersucht. Die Untersuchung eines fluoreszenten Tracers in der inneren Membranschicht ergab, dass dessen Verteilung nicht homogen war. Es wurden spezifische Membrandomänen gefunden, in denen das Molekül entweder vermehrt oder vermindert auftrat. Dies führte zu der Schlussfolgerung, dass diese Verteilung durch eine Interaktion des Tracers mit Proteinen des zellulären Zytoskeletts zustande kam.
Die in dieser Arbeit präsentierten Ergebnisse zeigen, dass EMFM erfolgreich für verschiedene biologische Untersuchungen im Forschungsfeld der Trypanosomen angewendet werden kann. Dies gilt zum Beispiel für die Untersuchung von der VSG Dynamik in künstlichen Membransystemen, aber auch für Studien in lebenden Zellen unter Verwendung der auf Hydrogelen basierenden Zelleinbettung.

1. Introduction

1.1 Microscopy in life sciences

1.1.1 Historical review

Scientific progress in the field of modern biology is closely related to the ability to visualize objects and structures that are usually invisible to the naked eye. Two names are commonly associated with the early invention of microscopes for scientific studies, Robert Hooke and Antonie van Leeuwenhoek. Hook extended previously developed simple optical devices in the sixteenth century by including a stage, a light source and three optical lenses to his microscope. He was the first person to publish his microscopic observations in 1665 [1], which improved scientific theories on many subjects. Van Leeuwenhoek (1632–1723), acknowledged as the father of microbiology, refined optical lenses and his simple single-lensed microscopes could resolve details as small as one micrometer. He was the first scientist to describe life in droplets of water in the form of bacteria and protozoa in 1667 [2]. Another important step in the application of microscopy in life sciences was the establishment of histological staining methods. The accumulation of dyes at specific cellular compounds facilitated the discovery of many cytological phenomena in the late 1800s and early 1900s [3, 4, 5]. The properties of the staining dyes to change the light absorption properties of different cellular structures provided sufficient contrast for microscopic observations. However, it was the discovery of fluorescence and its diverse applications that facilitated microscopy at the sub-micrometer level. John Herschel's description of the fluorescent quinine sulfate in 1845 [6] is regarded as the modern discovery of fluorescence. Together with George Stokes, who published a collection of fluorescent probes in 1852 [7] and described fluorescence as the light emission induced by excitation, their discoveries are at the base of nowadays fluorescence microscopy. The development of synthetic fluorescent dyes in the following decades enabled the first fluorescence based studies in animal physiology by Paul Ehrlich [8]. Many important discoveries were made since than and the rapid development of fluorescent probes and imaging devices extended our knowledge in the field of biology substantially. The recently awarded Nobel prices for the discovery of GFP in 2008 and the application of super-resolution imaging in 2014 reflect the large impact of fluorescence based techniques.

1.1.2 Fluorescence and fluorescent probes

Fluorescence is a physical process that occurs when a photon of a specific wavelength is absorbed by an atom or a molecule, and consequently gets re-emitted as a photon of a longer wavelength [9]. Our understanding of this process has increased significantly since the first description by George Stokes in 1852 [7]. At the fundamental level, single photons are absorbed by ground state electrons of a fluorophore (S_0), which then undergo an excitation transition to a higher electronic singlet state (S_1', Figure 1.1). This process distinguishes fluorescence from chemiluminescence, in which the excited state is initiated by a chemical reaction. The transition during fluorescence based excitation is followed by a partial loss of energy due to intramolecular vibrations and the transition to a relaxed singlet excited state (S_1), from which fluorescence emission originates. This is accompanied by the return of the fluorophore to its ground state and the emission of a photon. The emitted photon exhibits a wavelength longer than the absorbed wavelength. Several other relaxation pathways are known that compete with the fluorescence emission process. The excited state energy can e.g. be dissipated as heat, in collision with another molecules to transfer energy, or can turn to a lowest excited triplet state via intersystem crossing. In the latter, transition to the excited singlet state yields a delayed fluorescence.

The difference in excitation light and emission wavelengths of a fluorophore is fundamen-

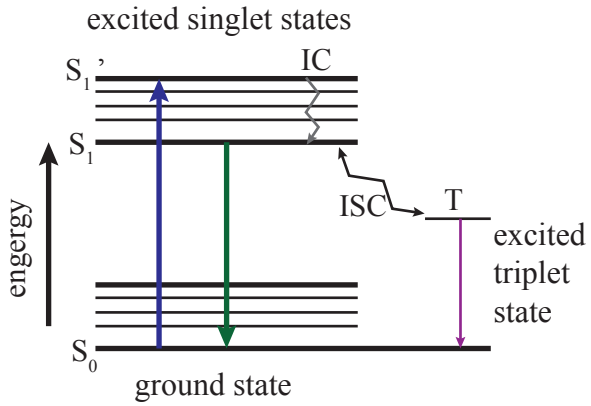

Figure 1.1: Scheme of a Jablonski diagram. Schematic presentation of the excitation transition to the S_1' state after the absorption of a photon (blue line), internal conversion (IC) to the excited S_1 state and fluorescence emission of a photon during the return to its ground state (S_0, green line). Intersystem crossing (ISC) to the excited triplet state (T) can occur followed by phosphorescence (magenta line).

tal to the principle of fluorescence microscopy. The excitation light is usually $\sim 10^6$ more intensive than the emission light. Thus, it needs to be efficiently suppressed in the image path to only detect the emission light at a camera. This can be achieved using appropriate optical filters (e.g. dichroic mirrors). This way, the contrast in e.g. biological samples can be enhanced, which allows to image individual structures.

The process of fluorescence is repeatable and single fluorophores can emit thousands of detectable photos, before they are irreversibly bleached. The collection of a multitude of emitted photons is fundamental for the high sensitivity of fluorescence techniques.
The principle of fluorescence was first practically applied in a microscope at the beginning of the twentieth century by physicists Otto Heimstädt and Heinrich Lehmann, who studied autofluorescence in bacteria, animal, and plant tissues [10, 11]. The ongoing success of fluorescence microscopy in life sciences is since then closely related to substantial technical improvements. This encompasses technical developments that facilitate a clear separation of the excitation and emission light (e.g. dichroic mirrors) and highly photon sensitive semiconductor devices (e.g. CMOS or EMCCD cameras) to detect low-light signals. The discovery of fluorescent proteins and organic dyes allows to specifically label molecules in living cells. Especially the discovery of the green fluorescent protein (GFP) in 1962 by Shimomura et al. [12], together with developments in molecular cloning technologies, facilitated modern scientific studies to investigate cellular processes and structures. Nowadays, a multitude of fluorescent proteins like eGFP, eYFP, eRFP and many more are available with absorption/emission spectra covering the range of visible light and beyond [13]. Newly engineered proteins exhibit enhanced quantum yields and photostability or can be photoactivated to undergo photoconversion to different emitting states [14, 15]. These fluorescent proteins are widely used and can be easily integrated into the genome of an organism to be expressed as a fusion protein together with the protein of interest. Disadvantages of fluorescent proteins are their relative large size, which might impair the physiological function of the labeled protein of interest due to steric hindrance and their limited brightness. Novel approaches to overcome these limitations include indirect specific labeling of proteins of interest via sequences like SNAP- or HALO-tags. They are usually co-expressed with a cellular protein and can then be specifically labeled by incubation with substrates that recognize the tag-sequences. These substrates are additionally labeled with small organic fluorophores [16]. This approach enables a brighter and more photostable labeling of proteins and can be of advantage when long-time observations or high localization precisions are required for the experiment [17]. However, with a molecular weight of $\sim$ 30 kDa these proteins are also reasonably large.
Many more labeling strategies were developed to specifically target molecules of interest in biological samples, all with specific advantages and limitations. Fluorescently coupled antibodies, for example, offer a high labeling accuracy. Intracellular staining, though, requires chemical fixation prior to labeling and is thus not suitable for microscopy in living cells [18]. Organic fluorophores comprise a large group of small dyes in the range of nanometers, of which some possess the ability to permeate cell membranes. They usually exhibit exceptional brightness and photostability [19]. Conjugated organic fluorophores (chemically modified with e.g. maleimide or NHS-ester) offer the general ability to label any molecules that possess suitable reactive side groups (e.g. primary amines, thiol groups

etc.). They are commonly used for *in vitro* labeling in purified protein samples (Figure 1.2). The specific labeling of a protein of interest in the complex nature of a cellular environment via conjugated organic fluorophores is usually difficult and limited to special conditions.

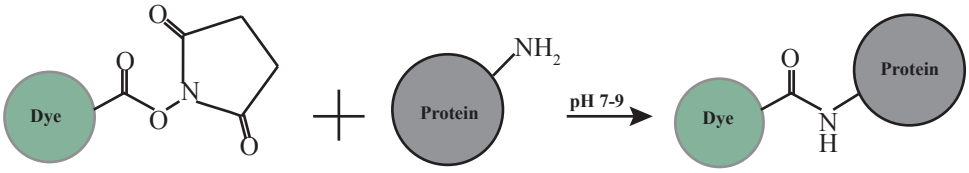

Figure 1.2: NHS-ester based protein labeling. A fluorescent dye is coupled to the NHS-reagent that readily reacts with target primary amines of a molecule (e.g. a protein) at a pH of 7-9 and forms a stable, covalent bond. The rate of reaction increases with the pH of the buffer.

Such conditions might be given, when the VSG coat of living trypanosomes is fluorescently labeled. Trypanosomes exhibit a dense VSG coat on their cell surface. About 95% of all surface proteins are VSGs [87] and small invariant surface proteins are hidden below the VSG coat. Each VSG is accessible to reactive dyes in alkaline buffer conditions due to primary amine groups [20] and the vast majority of labeled surface proteins are VSGs when reactive organic fluorophores are used [20].
The presented examples represent only a small selection of the available fluorescent dyes and labeling strategies. Nowadays a variety of fluorescent probes are available, covering a wide range of labeling procedures and photo-physical properties. The selection of suitable dyes depends on the experimental requirements and the scientific research question. The rapid development of new fluorescent probes with enhanced photo-physical properties and improved labeling accuracy constantly extends the repertory for prospective applications [19].

1.1.3 Fluorescence microscopy

Basic concepts and applications

Modern fluorescence microscopy is a powerful tool for cell and molecular biologists to investigate phenomena in life sciences. Concomitant with the development of fluorophore probes for the *in vivo* and *in vitro* visualization of structures and proteins, substantial technical improvements were achieved within the last decades. This facilitated the establishment of numerous novel microscopy methods and their application. Many of these techniques are now being commercialized and each technique provides specific advantages and limitations. Some of the main fluorescence microscope concepts and selected examples are introduced in the following section.
The simplest form of a fluorescence microscope setup includes a widefield excitation of

the fluorophores using a light source. Here, the emission signals are separated from the light source via a dichroic mirror. The emission light is then commonly detected using a sensitive camera. The usage of electron multiplying CCD cameras (EMCCD), for example, facilitates the detection of low-light fluorescence in a sample with little camera noise. In addition, many improvements were made in the production of light filters, mirrors and high numerical aperture objective lenses. The simple setup of widefield based microscopes results in relatively low costs, while still providing good lateral and very fast temporal resolutions ($\sim$ 200 nm and μs to ms) [21]. Hence, the concept is widespread in research.
In contrast to widefield microscopy, confocal laser scanning microscopy (CLSM) relies on a point-by-point illumination of the sample with a focused laser beam. The signal is detected sequentially from each point via a photomultiplier tube until an entire image is created. The method involves the usage of a spatial pinhole to block out-of-focus light and scanning of the specimen by moving either the stage or the laser beam in both lateral directions. In CLSM, high axial resolutions can be achieved ($\sim$ 500-700 nm) [22], but scanning of large samples can result in relatively slow acquisition cycle times. Most commercial systems offer multiple color-channels and variable pinhole sizing for selecting the desired optical section thickness. The two-photon fluorescence microscopy represents an adaptation to a confocal microscope and is particularly useful for imaging thick samples [23].
Widefield and confocal architectures are the basic concepts of fluorescence microscopy applications. The available literature provides a comprehensive overview of the established methods and their application to study cellular structures, molecular interactions and dynamic processes in the field of biology (e.g. [9]).
In this work, fluorescence recovery after photobleaching (FRAP) was used to study dynamic processes and will therefore be introduced in more detail. FRAP is a method, that provides insights into 2D dynamic processes of a molecule. It was developed already in the 1970s in W. W. Webb's laboratory [24] and is nowadays an established and widespread tool for researchers. FRAP represents an ensemble measurement method, that consists of two steps. First, a region of interest (ROI) is irreversibly bleached in e.g a cell, tissue or model membrane using a short, strong laser pulse. Second, the recovery of fluorescence in that region is monitored over time (Figure 1.3). Appropriate theoretical models can than be used to analyze the fluorescence recovery curve to extract e.g. diffusion coefficients or reaction times [25].
FRAP was used to study many protein interactions and dynamic processes, for example the diffusion of grana thylakoid membrane chlorophyll-protein complexes [26], the diffusion of GPI-anchored Variant Surface Glycoproteins (VSG) from trypanosomes [20] and many more [27]. In this work, FRAP was used to study the dynamics of VSG proteins reconstituted into an artificial lipid bilayer system at different lateral protein densities (see Section 2.1.2).

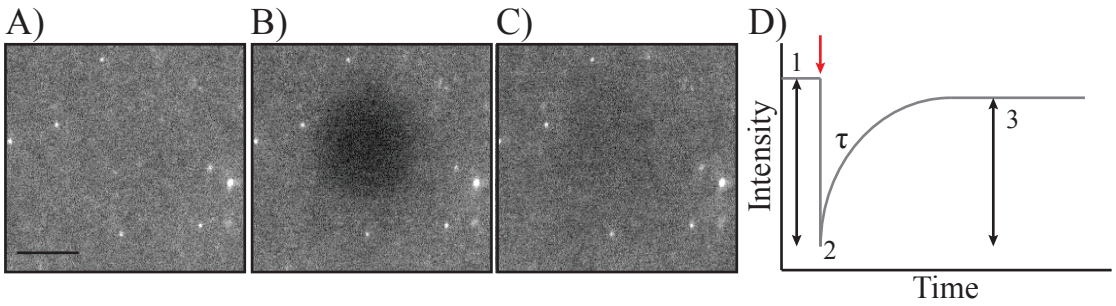

Figure 1.3: Principle of FRAP. Exemplary supported lipid bilayer covered with ATTO-488 labeled VSG M1.6. A) Pre-bleach reference frame. B) Irreversible bleaching of a ROI with a short laser pulse. C) The recovery of the fluorescence in the ROI is monitored over time. D) Schematic representation of a FRAP curve. The fluorescence intensity in the ROI before bleaching (1) and its recovery after bleaching (red arrow) are monitored (2-3). The diffusion coefficient can be calculated from the half recovery time, τ, and the difference between (1) and (3) equals the mobile fraction of the molecule. The scale bar is 5 μm and valid for A-C.

The diffraction limit

Biological systems are intrinsically heterogeneous and experimental investigations have usually been made on the population level. A main disadvantage of this approach is the potential loss of relevant information by averaging over a multitude of observed objects. In order to understand basic biological processes, it is necessary to investigate the properties of e.g proteins or lipids on the scale of a sub-cellular level and below. While a technique like electron microscopy can provide a very high resolution to study structures in this range, its applicability is restricted to static systems [28]. Biological systems, however, are highly dynamic. Therefore, alternative concepts were developed within the last years that provide high resolutions and also allow to study dynamic processes. Fluorescence based light microscopy is suitable for such studies and commonly applied in the field of life sciences. The observations, however, have physical constraints which are governed by the properties of light. These limitations were known before but were first fully described in a theoretical treatment by George Airy in 1835 [29] and later mathematically founded by Ernst Abbe in 1873 [30].

When light passes through an opening in a microscope, the spatial resolution is limited by diffraction and point-like emitters are blurred out as described by the point spread function of the microscope. When the opening is a circular aperture, the interference pattern of light results in so called 'Airy-disks'. The profiles of these patterns depend on the wavelength of the light and the size of the aperture. The central disk of a pattern exhibits a local maximum and is surrounded by concentric rings of less intensity (Figure 1.4).

The spatial resolution of an optical system can be estimated by the Rayleigh criterion,

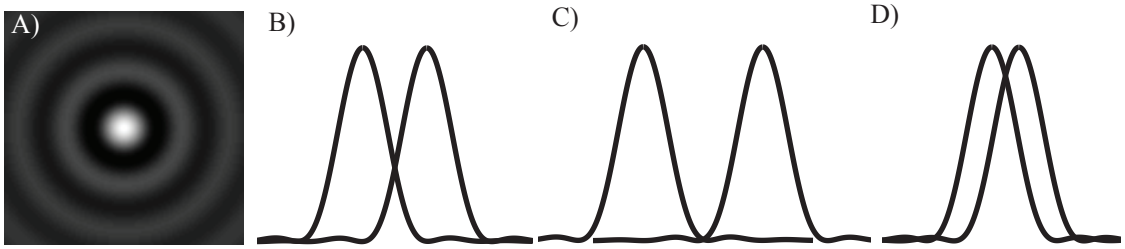

Figure 1.4: Resolution limit in an optical system as defined by the Rayleigh criterion. A) Computer-generated image of a diffraction limited field pattern of an Airy disk. B-D) Schematic presentation of the Rayleigh criterion: Two point source objects can be resolved if the central peaks of the two diffraction patterns are no closer than the radius of the Airy disk (B and C). If the Airy discs are physically closer, they cannot be resolved (D).

which states, that two point sources are resolved when the first diffraction minimum of the image of one point source coincides with the maximum of another point source. This is fundamental for the achievable resolution in light microscopy. In the spectrum of visible light (400-800 nm) the resolution lies in the range of 160 - 330 nm nanometers. These physical restrictions were generally accepted and somewhat prevented efforts to overcome the diffraction barrier in light microscopy for a century, despite the necessity to improve the visualization of cellular structures.

Point spread function and single-molecule localization

The precise localization of a single fluorescent object beyond the diffraction limit can be achieved because although the image of a point emitter is blurred, the maximum of the intensity distribution can be determined precisely, given a sufficient number of photons in the spot [31]. As described in Section 1.1.3, conventional light microscopy is limited by diffraction and point-like emitters are imaged in an optical system according to the PSF of the microscope. The center of the PSF represents the true position of the emitter and different fitting based algorithms were shown to be suitable to determine the position of single molecules [32]. The exact spatial intensity distribution of the PSF is given by:

$$PSF_{Airy} = \left[2 \frac{J_1(k_{em} NA \sqrt{x^2 + y^2})}{k_{em} NA \sqrt{x^2 + y^2}} \right]^2, \tag{1.1}$$

where $J_1(x)$ is the first-order Bessel function of the first kind and $k_{em} = 2\pi/\lambda_{em}$ for the emission wavelength λ_{em} [33]. As Eq. 1.1 is complex, fitting based single-molecule localization algorithms often apply a Gaussian approximation for the PSF. This usually leads to good results with low computational demands [33, 34]. The Gaussian approximation is

given by:

$$PSF_{Gaussian} = A\ exp\left(-\frac{x^2+y^2}{2\omega_{xy}^2}\right), \tag{1.2}$$

where ω denotes the Gaussian standard deviation and A the amplitude. In fluorescence based single-molecule imaging, the localization precision is essentially reduced by experimental conditions such as the limited number of detected photons from a single fluorophore, pixelation of the detector or noise sources in the detection process [33].
Three parameters can be derived from a Gaussian fitting approach, their respective intensity, signal width and position [35]. These informations can further be compared to e.g. predetermined single-molecule footprints in order to exclude false positive single-molecule localizations [36].
The localization of single molecules from an image sequence is the base of further data analysis and can be used to e.g. reconstruct super-resolution images or investigate molecular dynamics.

Single-molecule and super-resolution microscopy

Optical fluorescence imaging techniques that provide spatial information of point source objects beyond the diffraction limit are known as single-molecule or super-resolution microscopy methods. Within the last decades, two main techniques were developed to bypass the limitations of diffraction by applying either a stochastic or a deterministic approach.
The photoactivated localization microscopy (PALM) and the stochastic optical reconstruction microscopy (STORM) are representative for stochastic techniques. Both concepts were developed simultaneously in the earls 2000s [37, 38, 39]. They apply a spatiotemporal separation of fluorescence signals in a sample with a high label density by exploiting the photoconversion of fluorophores (photoactivation in the case of PALM and photoswitching in the case of STORM). This facilitates the detection of isolated, diffraction limited fluorescence spots. As explained in Section 1.1.3, the position of the emitters can be calculated with a high precision. Repetitive illumination cycles result in detecting a multitude of such single-molecule positions, even though they can be located physically closer than defined by the Rayleigh criterion (Section 1.1.3). The summation of all detected single-molecule positions from an image sequence allows then the reconstruction of structures with high spatial resolution. According to the Nyquist-Shannon theorem, a structural feature can only be fully resolved when the distance between two labels is less than half the feature size [40]. In PALM and STORM based imaging, the high label density and localization precision of individual molecules facilitate the generation of such super-resolution images that represent structural features. Nowadays, these methods are well established and commonly used by researches to study versatile biological phenomena (reviewed in [41, 42]).
The second prominent concept, the stimulated emission depletion microscopy (STED),

uses a deterministic approach to conduct super-resolution microscopy. It was developed in the 1990s [43, 44], and also allows investigations of biological structures at the level of single molecules down to the nanoscale precision. The enhancement of the resolution is mainly based on locally switching off the fluorescence of a dye molecule in the periphery of its diffraction limited profile by stimulated emission depletion using a ring patterned intense laser beam. The remaining fluorescence from the center of the fluorophore is smaller than the diffraction limit and allows the determination of a single molecule positions down to 20 nm [45] without the need of fitting-based single-molecule localization steps. Scanning of the specimen by moving either the stage or the laser beam in both lateral directions facilitates imaging a ROI and likewise to STED and STORM, super-resolution images can be reconstructed from the single-molecule positions.

Single-particle tracking and trajectory analysis

Fluorescence based super-resolution microscopy facilitates imaging structures with a high spatial resolution (see Section 1.1.3). Next to resolving static objects, single-molecule fluorescence microscopy can also be used to monitor the motion of single, dynamic molecules over time. Within the last years, robust tracking algorithms were developed to generate trajectories from single-molecule positions of dynamic particles in consecutive images [35, 46]. These methods are well established and can deal with e.g. high particle densities and arbitrarily large diffusion coefficients [47] as well as particle motion heterogeneity [48]. In a recent study, multiple tracking approaches from different laboratories were compared for different scenarios, highlighting the capabilities and restrictions of each applied method [49]. However, usually the restrictions from fluorophore photophysics and the labeling efficiency are rather limiting for studying dynamic processes in cells than the generation of trajectories from single-molecule positions.
Once trajectories are successfully generated they can be analyzed in detail to study the dynamics of the particles. This usually involves describing the molecular dynamics in terms of e.g. the diffusion coefficient or particle velocities.
The most fundamental form of a particle motion is diffusion. Diffusion is the Brownian motion of an object, that is driven by thermal energy. The lateral diffusion of a particle is characterized by the diffusion coefficient D, which is introduced by Fick's second law:

$$\frac{d}{dt}p(\vec{r},t) = D \bigtriangledown^2 p(\vec{r},t), \tag{1.3}$$

where $p(\vec{r},t)d\vec{r}$ denotes the probability of finding a particle within a given volume $(\vec{r},\vec{r}+d\vec{r})$ at a time point t. Solving Fick's second law in space followed by integration, yields the

radial probability, which is for two dimensions:

$$p(r,t) = \frac{2\pi}{4Dt} r * exp\left(-\frac{r^2}{4Dt} \right), \tag{1.4}$$

where r_0 denotes the starting position of a particle and $r^2 = (r - r_0)^2$. The frequency distribution of diffusion steps from a given a trajectory can be used as an approximation for the probability distribution function, however, binning in the process might introduce bias. Alternatively, the cumulative distribution function (P_{cum}) can be analyzed, which is in case for two dimensions:

$$P_{cum} = 1 - exp\left(-\frac{r^2}{4Dt} \right). \tag{1.5}$$

Analyzing the probability distribution can provide reliable information about the diffusion coefficient of an object. Further, the presence of additional populations with different diffusion coefficients within a sample can be analyzed using multi-exponential curve fitting of the probability distribution function.

Many more concepts were developed to determine the diffusion coefficient of a molecule, with the mean squared displacement analysis (MSD) being the most prominent. A general definition of the MSD is:

$$MSD(n\Delta t) = \frac{1}{N-1-n} \sum_{i=1}^{N-1-n} \{[x(i\Delta t + n\Delta t) - x(i\Delta t)]^2 + [y(i\Delta t + n\Delta t) - y(i\Delta t)]^2\}, \tag{1.6}$$

where N denotes the consecutive steps at a time lag $\tau = n\Delta t$, x and y the position of a particle within a trajectory at a discrete time lag t, and Δt the smallest time interval resolved. The MSD is calculated for each trajectory and averaged to estimate the population MSD as a function of time. In case of free diffusion, the MSD results in a straight line, with the slope proportional to the diffusion coefficient. For Brownian diffusion in 2D, this results in $MSD(t) = 4Dt$.

The precision of a MSD analysis for highly dynamic particles benefits from resolving the dynamic processes at short time lags and the overall number of individual trajectories that contribute to the average MSD [50]. As the error in the estimation of the MSD increases for larger time lags, usually 1/4-1/10 of the time lags are used for a linear fit [51, 52]. The MSD can further be corrected for limitations in temporal and spatial resolution [53, 54, 55].

For a molecule diffusing in a natural system like a cell membrane, many boundaries and obstacles can be present, preventing unhindered diffusion. These physical barriers might be represented by immobile protein complexes or fence structures. They can result from interactions with cytoskeletal components and can permanently or only transiently influence the mobility of a molecule [56]. Further, energy dependent processes can lead to the active transport of e.g. cargo or molecules inside a cell [57]. Many models have been

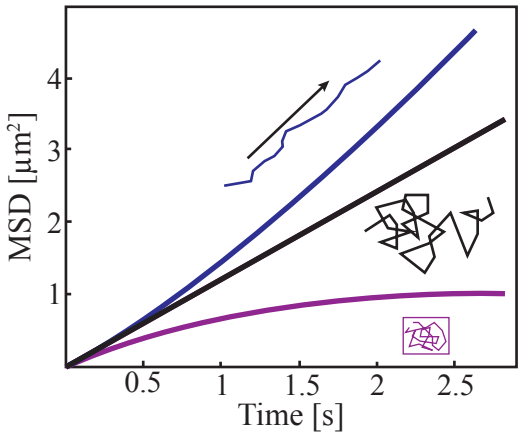

Figure 1.5: Schematic representation of MSD plots for different types of motion. The linear plot (black line) indicates normal Brownian motion, whereas the the asymptotic behavior of the MSD curve illustrates restricted particle motion within a given area (magenta line and box) and is called confined diffusion. A quadratic dependence (blue line) can arise from directed, active transport of a molecule.

proposed to consider such situations, with relatively simple forms being described by the confined diffusion or the directed transport of a molecule [36].
In the case of confined diffusion in a square with reflecting boundaries of side length L, the MSD is given by:

$$MSD(t) = \frac{L^2}{3}\left[1 - exp\left(\frac{-12Dt}{L^2}\right)\right]. \tag{1.7}$$

Next to the local trapping of a molecule, energy driven processes can influence the diffusion of a molecule and result in a mixed mode of motion. Under these conditions, the resulting MSD contains both a diffusive and a transport term, which depends on the velocity v:

$$MSD(t) = 4Dt + v^2t^2. \tag{1.8}$$

Deviations from the linear growth of the MSD with time are generally termed anomalous diffusion. While free Brownian motion results in $MSD(t) = Dt^{\alpha}$ with $\alpha = 1$, confined diffusion and active transport are characterized by $\alpha < 1$ and $\alpha > 1$, respectively. α can be determined from a fit to $MSD(t)$ and thus allows to draw conclusions about the diffusion behavior of a molecule.

1.1.4 Single-molecule microscopy in living organisms and model membranes

The establishment of fluorescence based super-resolution and single-molecule microscopy within the last decades allowed researches to study dynamic processes and structures in biological systems with high resolution. While it is impossible to give a comprehensive overview of all achievements, this section will focus on some examples to highlight the diversity in the research field.

The applicability of single-molecule microscopy has already been demonstrated by Schmidt et al. in 1996 [35], where the authors measured the diffusion of fluorescently labeled lipids in a supported lipid bilayer (SLB). Since then, many studies were employed to study dynamic properties of e.g. membrane associated proteins. Most studies focused on membrane systems, especially because localization in a two-dimensional system is rather simple to achieve compared to the three-dimensional localization of dynamic proteins in e.g. the cytosol or a tissue. Sako et al., for example, monitored the dynamic formation of epidermal growth factor receptor dimers on a cell membrane upon binding of the epidermal growth factor [58]. G-protein coupled receptor homodimerization was also revealed at the nanometer resolution on living cells [59]. The potential link of protein mobility to compartmentalization of the plasma membrane was investigated within the last years [60, 61]. Using single-particle tracking, Bakker et al. have shown that the actin cytoskeleton regulates the lateral mobility of the integrin receptor [62] and Weigel et al. have proven receptor interaction with other membrane components, such as clathrin-coated pits and the glycocalyx matrix using a multi-color single-molecule approach [63].

These studies illustrate that cell membranes are complex and can be highly occupied by membrane proteins. The simplified model of a cell membrane as postulated by Singer and Nicolson in 1970 [64] only insufficiently represents the true nature cell membranes. A myriad of protein interactions can effect the mobility, localization and behavior of a membrane protein in the dynamic environment of a cell. Hence, the complexity of a plasma membrane is better described by the model of fences and pickets [56].

Next to monitoring dynamic objects in living cells, single-molecule microscopy further facilitated imaging cellular structures with a high spatial resolution. Lee et al. used the intrinsic blinking behavior of eYFP molecules to construct super-resolution images and studied the distribution of a nucleoid-associated protein in *Caulobacter crescentus* [65]. Direct stochastic optical reconstruction microscopy (*d*STORM) was e.g. applied to visualize the symmetry of the nuclear pore complex with a nanometer precision [66].

These examples show, that single-molecule and super-resolution microscopy enables the direct observation of molecules in a cellular environment, which can significantly improve our understanding of the fundamental principles in a cell. However, due to the immanent complexity of biological systems, it can be challenging to investigate the behavior of

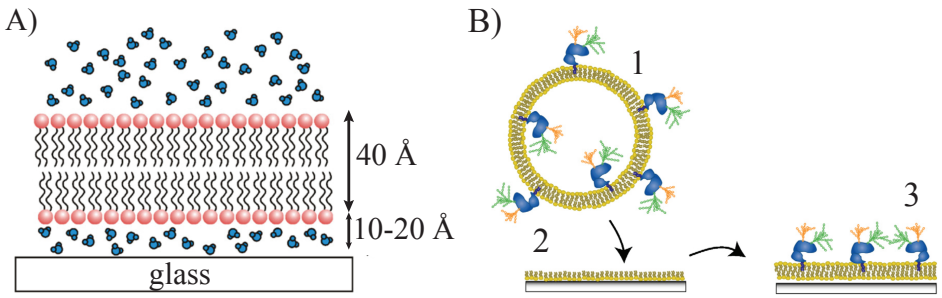

Figure 1.6: Schematic presentation of a solid supported phospholipid bilayer. A) The fluid lipid bilayer is ∼40 Å thick and is separated from the glass support by a 10–20 Å thick layer of water. B) SLB with integrated membrane proteins. Preparation of a supported membrane by spreading of proteoliposomes (1) on a pre-deposited lipid monolayer above a glass support (2). After vesicle fusion, a fluid lipid bilayer forms that includes membrane proteins (3). The figure is adapted from [70, 71].

single molecules. In order to reduce the environmental impact for the molecule of interest, experiments were also performed in model membranes. Model membranes were developed to mimic a cell membrane under defined conditions and reduced complexity. They can be made from variable lipid compositions and can be used to integrate lipids or membrane associated proteins. The most common forms of model membranes are lipid vesicles and planar systems like the supported lipid bilayers, which are ideally suited for microscopy-based investigations. Supported lipid membranes consist of a fluid lipid bilayer above a hydrophilic solid support (Figure 4.2.7, A). They can be formed via the fusion of lipid vesicles [67] or a Langmuir-Blodgett transfer based formation of lipid bilayers [68]. A variety of studies on lipid and protein dynamics were performed in SLBs. Ladha et al., for example, used ensemble FRAP measurements to study the diffusion of fluorescent lipids in a planar lipid bilayer system [69] and single-particle tracking was performed to study the dynamics of GPI-anchored prion proteins [70]. Atomic force microscopy has also become a well-established method for imaging reconstituted proteins at a nanometer resolution [72] and reflection interference contrast microscopy was recently applied to study cadherin domain formation in a cell-free system [73]. The possibility to reconstitute membrane proteins into SLBs at different protein concentrations further facilitates studies on protein dynamics in highly occupied environments [74, 75] (Figure 4.2.7, B).
These selected exemplary studies illustrate, that SLBs are well-established and commonly used to study protein dynamics and interactions under defined conditions. Investigations in model membranes can significantly contribute to our understanding of the fundamental properties of membrane associated processes, especially when combined with complementary *in vivo* measurements.

1.2 The parasite *Trypanosoma brucei*

1.2.1 Trypanosomes and disease

African trypanosomes are eukaryotic unicellular parasites and the causative agents of sleeping sickness (human African trypanosomiasis, HAT) in humans and nagana in cattle. They can infect a wide range of vertebrates and are transmitted via the tsetse fly (*Glossina* spp.), which limits their prevalence to the sub-Saharan regions of Africa. They are extracellular parasites, occurring and proliferating primarily in the bloodstream of their host and the course of the disease is lethal if left untreated. The species with the greatest effects on cattle and livestock are *Trypanosoma vivax*, *Trypanosoma congolense* and *Trypanosoma brucei*. Humans are naturally immune against most trypanosome species. However, two subspecies of *Trypanosoma brucei* are able to infect people and cause disease. These subspecies are named *Trypanosoma brucei rodesiense* and *Trypanosoma brucei gambiense*. They have evolved strategies to overcome the resistance mechanisms in humans [76, 77], and hence, represent a danger to a wide population resident in central and sub-Saharan Africa. Today, HAT is considered as a neglected tropical disease with more than 3700 reported cases of infection in 2014. The treatment is difficult due to severe side-effects or toxicity of the available drugs (pentamidine, suramin, melarsoprol, eflornithine and nifurtimox) [78], as well as accessibility to medical treatment for people in affected regions [79]. The course of an infection can be divided into two stages and the time courses are specific for the individual subspecies. After infection via the tsetse fly vector, trypanosomes proliferate in the bloodstream and the lymphatic systems of the host, and symptoms like fever, headache, and weakness are commonly observed in patients. Trypanosomes have evolved sophisticated strategies to maintain a persistent infection inside a host despite the constant attack from host immune system. The host immune response and cellular adaption processes result in regular periodic waves of parasitaemia. The trypanosomes can also cross the blood-brain barrier and infect the brain and central nervous system. This step is accompanied by typical neurological symptoms and can lead to coma and finally the death of affected patients.

1.2.2 *T. brucei*: life cycle, cell architecture, and proliferation

Trypanosomes posses a complex life cycle, which is adapted to the different environmental conditions in the mammalian host and the tsetse fly vector. It includes alterations in metabolism, cell morphology, and the repertoire of plasma membrane proteins. Seven distinct trypanosome stages have been identified in the fly, of which the procyclic form (PCF) is the best known and most tractable to study. Two common forms are present in the mammalian host, the bloodstream form (BSF) and the short stumpy form. BSF and

PCF trypanosomes are relatively easy to cultivate *in vitro* and hence, are commonly used as model organisms for experimental studies. BSF trypanosomes are the proliferative stage and are responsible for the level of parasitaemia. They can differentiate into short stumpy cells, which are arrested in the G1/G0-phase of the cell cycle. This arrest limits their lifespan to 2-3 days. The transition of BSF to short stumpy forms occurs at high BSF concentrations in the bloodstream and is triggered by a secreted factor, the stumpy induction factor [80]. This mechanisms is thought to limit the number of proliferating trypanosomes and thereby keep the parasitaemia at a level that is yet not lethal for the host. The uptake of short stumpy trypanosomes during a bloodmeal of the tsetse fly is also the basis for the transition to a PCF in the fly. PCF trypanosomes undergo diverse morphological changes during their route through the insect and the parasite life cycle is completed after a tsetse injects metacyclic trypanosomes into the skin of the host, which subsequently undergo a transition to BSF trypanosomes.

Taxonomically, African trypanosomes are flagellated protists that belong to the order Kinetoplastida. Kinetoplastida are characterized by the presence of a complex circular DNA network (the kinetoplast) that comprises the genome of the cell's single mitochondrion. The kinetoplastid group includes a number of species that are responsible for diseases in humans, animals and plants (e.g. *Trypanosoma cruzi*, *Leishmania* or *Phytomonas*). The most widely studied kinetoplast is *T. brucei brucei*, which exhibits a high similarity to human-infective trypanosomes, but to which humans are naturally immune. Various laboratory strains are nowadays available for research and cell populations can be cultivated relatively easily *in vitro*. Genetic modifications have become routine within the last years, which facilitated the establishment of *T. brucei brucei* as a model organism to study fundamental cellular processes. The possible positioning of trypanosomatids (trypanosomes and Leishmania) near the root of the eukaryotic tree of life makes them an interesting point of comparison to study basic cellular mechanisms in an evolutionary context relative to the more intensively-studied animals (e.g. *Drosophila* spp. or *Caenorhabditis elegans*) [81]. Further, the coevolution of *T. brucei* with its mammalian hosts can be studied to increase our understanding of parasite-host relationships [82].

Trypanosomes possess all the major eukaryotic organelles such as a nucleus, a Golgi apparatus, an endoplasmatic reticulum, endosomes, lysosomes and a mitochondrion (Figure 1.7). Furthermore, they have a highly polarized cell architecture. Microtubules extend from the anterior pole to the posterior end of the cell and form a highly ordered sub-pellicular corset that is connected to the plasma membrane [83]. The single flagellum emerges from an invagination of the plasma membrane near the cell's posterior pole called the flagellar pocket. The flagellum is attached to the plasma membrane via the flagellum attachment zone and extends beyond the anterior end of the parasite. The flagellar beat is at the origin of any cellular movement and *T. brucei* achieves velocities of up to 24 μm s^{-1} in the blood of their host [84]. The main features of the flagellar architecture

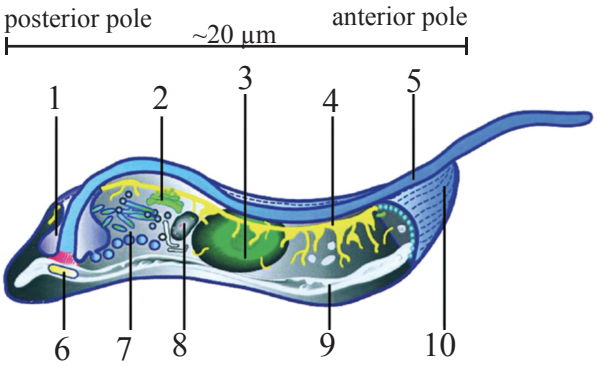

Figure 1.7: *T. brucei* cell architecture. Schematic overview of the bloodstream form (BSF) cell architecture including all major organelles and their respective localizations: 1) flagellar pocket 2) Golgi apparatus 3) nucleus 4) endoplasmatic reticulum 5) flagellum 6) kinetoplast 7) endosomes 8) lysosome 9) mitochondrion 10) surface VSG coat. The cell's posterior pole is located near to the flagellar pocket, whereas the anterior pole is near the flagellar tip. The scheme is adapted from [87].

are the axoneme, which includes canonical arrangement of 9+2 microtubules, and the paraflagellar rod, a lattice-like filament that extends along the flagellum and is physically connected to the axoneme [85]. The flagellar pocket represents a specialized region of the plasma membrane and is the only side of endo- and exocytosis in trypanosomes [86]. In the bloodstream of the mammalian host, the trypanosome's plasma membrane is covered with a dense layer of GPI-anchored variant surface glycoproteins (VSG), that forms a protective barrier over the cell surface. *T. brucei* bloodstream form cells duplicate every 6-8 hours via cell division. The process starts with a duplication of all major organelles, followed by fission of the plasma membrane, beginning at the anterior end of the cell. The physical segregation proceeds along the longitudinal axis until the posterior end of the cell is reached. Each resulting daughter cells possesses a single copy of all organelles and the duplication process repeats.

BSF trypanosomes are of great importance for the parasitaemia in the mammalian host, since they represent the proliferating stage form. As trypanosomes are exclusively extracellular parasites, they are permanently exposed to the host immune system. As a first defense mechanism against the immune response, BSF trypanosomes exhibit a dense layer of VSGs on their cell surface.

1.2.3 The VSG coat of *T. brucei*

The surface coat of *T. brucei* forms a dense layer and VSGs comprise more than 95% of the overall cell-surface proteome [88, 89]. The VSGs are GPI-anchored, which facilitates a high mobility on the cell surface. The dense arrangement of VSGs impairs the identification of epitopes of invariant surface proteins by the immune system [90]. VSGs form homodimers on the cell surface with a total number of approximately 5 x 10^6 dimers covering the whole trypanosome [91]. Even though trypanosomes possess a large genomic repertoire of several hundred different VSG-encoding genes [92], only one VSG gene is expressed at any given time [93]. This expression occurs at a specific genomic locus,

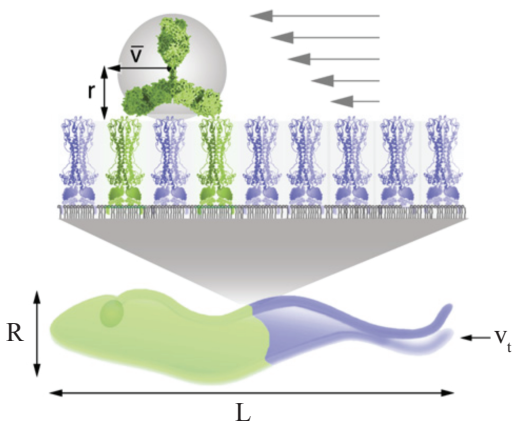

Figure 1.8: Schematic representation of hydrodynamic flow mediated sorting of VSG-antibody complexes on the cell surface of *T. brucei*. The complexes are directed towards the region of the flagellar pocket, where they are internalized. The drag forces can be determined from the radius of the antibody (r), the mean swimming velocity (v_t), the viscosity of the liquid (η) and the mean diameter of the cell (R). The scheme is adapted from [97].

the VSG expression site (ES) and hence, the VSG coat consists nearly exclusively of only one type of VSG. The VSG itself is highly immunogenic and rapidly detected by the host immune system, which will produce antibodies specific for the expressed VSG isoform. This facilitates an effective clearance of the infection in a host [94]. However, trypanosomes have evolved sophisticated strategies to maintain a persistent infection.

Strategies to escape the host immune response

One long-term mechanism exploited by *T. brucei* to maintain a persistent infection is based on antigenic variation, a stochastic event of switching the gene expression to an antigenically distinct VSG and its presentation on the parasite cell surface. This leads to a complete replacement of the former VSG coat and forces the host immune system to adapt to the novel antigen type. This adaptation provides sufficient time for the proliferating parasite to establish a new wave of parasitaemia while the immunologically detected population is cleared by the immune response. Switching the expression of VSG can occur by different mechanisms. In an *in situ* switch, the previously active ES is silenced and another ES is activated. Other mechanisms encompass the recombinational exchange of a VSG gene within an active ES or the exchange of telomers [95]. The subsequent replacement of the surface coat during a VSG switch is a passive process and primarily determined by dilutions during the cell division process and protein degradation, recycling and shedding [96].

Another strategy to evade the host immune response in the short term involves the rapid endocytosis of antibodies that are bound to surface VSGs. The mechanism relies on a passive sorting of the VSG-antibody complexes, which is mediated by hydrodynamic drag forces [97]. These forces are generated by the permanent forward cellular propulsion and causes a directional movement of bound VSGs towards the posterior end (Figure 1.8). A rapid internalization at the flagellar pocket followed by an intracellular degradation ensures that the antibodies are not exposed to the host immune system long enough to induce an

effective response. This is effective at low to moderate antibody concentrations, but cannot protect the cells at high antibody titers. Nevertheless, it is believed that hydrodynamic sorting is particularly important for the survival of the non-proliferating stumpy form, since it might provide the cells with sufficient time for the transmission to the tsetse vector before they are cleared by the immune response [97]. This assumption is supported by the finding that endocytosis rates were found to be even higher in short stumpy form trypanosomes [97].

Fundamental for the efficiency of both mechanisms is the high mobility of individual VSGs and the overall fluidity of the VSG coat. Any interference with this conditions could result in a stronger immune detection and lead to a rapid clearance of the whole cell population. Thus, there must be a strong selective pressure for maintaining the mobility of the VSG coat. However, at the same time the coat has to be extremely dense to fulfill its shielding function. This appears contradictory, since protein crowding was found to substantially decrease the diffusion coefficient of proteins [98].

Experimental determinations of VSG endocytosis and recycling rates illustrated the exceptionally high turnover rate of the VSG surface coat [99]. One trypanosome surface coat equivalent was found to be endocytosed every $\sim$ 10 min. This is surprisingly high, considering that the whole cell surface is covered with VSGs and the flagellar pocket is the sole side of endo- and exocytosis yet contributes only to $\sim$ 5% of the plasma membrane surface area. This feature is reminiscent of the narrow-escape problem, where a Brownian particle is confined to a domain with reflecting boundaries, except for a small opening, through which the particle can escape.

Previous measurements of the VSG diffusion coefficients in living trypanosomes supported the idea of a high surface coat mobility [100, 20]. The authors performed FRAP on surface VSGs of immobilized trypanosomes and measured diffusion coefficients for diverse VSGs of 0.01 - 0.03 $\mu m^2\ s^{-1}$ and mobile fractions of $\sim$ 80%. However, the measured VSG dynamics cannot solely explain the previously determined surface coat turnover rates and it remains unclear how trypanosomes maintain the protective barrier of the VSG coat.

Studying the biophysical properties of VSG is an essential element of this work. VSG dynamics are studied under defined conditions of model membranes and on the plasma membrane of living trypanosomes. To this end, FRAP and single-particle tracking experiments are performed.

VSG structure

VSGs are homodimeric proteins with a total size of 100-120 kDa. The proteins are integrated into the outer leaflet of the plasma membrane and extend $\sim$ 12 - 15 nm from the cell membrane [101]. The monomers consist of one or two small C-terminal domains (CTD) of 20-40 residues that are connected to a larger N-terminal domain (NTD) via a flexible linker region [91]. The NTD domain usually comprises 350-400 amino acids and can be grouped

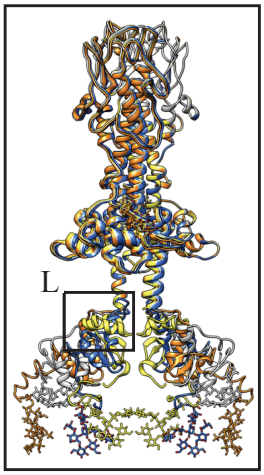

Figure 1.9: Model of a complete VSG structure. The structure of VSG M1.1 was calculated from a superposition of different models for the NTD from VSG M1.1 and includes the flexible linker region (L). The figure is adapted from [91].

into two classes (type A and B) by the position and number of conserved cysteine residues. VSGs are usually modified by one or more N-glycosylation sides [102]. The amino acid sequences between NTDs of different VSGs can vary significantly, which renders them antigenically diverse. However, the protein tertiary structure appears conserved within the classes, suggesting an important structure-function relationship on the cell surface.

1.3 Immobilization of *T. brucei*

Trypanosomes are intrinsically fast moving flagellates and their flagellar beat is the origin of their cellular motility. This complicates microscopy studies of living cells and requires cytocompatible cellular embedding prior to imaging. Previous attempts to immobilize trypanosomes include embedding in thermo-gelling agarose or gelatin gels [100, 20], the use of optical tweezers [103] or global energy depletion by replacement of glucose with 2-deoxy-D-glucose [104]. The low melting temperature of agarose and gelatin facilitated reversible immobilization and the cells showed high viability after embedding. However, these methods exhibit substantial disadvantages such as a temperature dependency of the gelation process or, in the case of glucose replacement, possible side effects due to global ATP depletion. While optical trapping of trypanosomes resulted in a limited motility, a strong shape deformation and rotation was still observed [103]. These remaining movements might be prevented by applying a slit trap or holographic optical tweezers. However, it remains questionable whether complete immobilization can be achieved on the nanometer level. Nevertheless, agarose or gelatin immobilization facilitated the studies of VSG dynamics in living trypanosomes on the ensemble level using methods like FRAP [100, 105].

State-of-the art single-molecule microscopy makes it possible to resolve biological structures and dynamic processes with high spatial and temporal resolution beyond the regime applicable to FRAP measurements. To achieve these high resolutions multiple illumination cycles are a prerequisite. This precludes substantial cellular movements during the recording procedure and excludes highly motile cells like trypanosomes from such studies. Further, the immobilization methods applied so far could not eliminate residual flagellar movement and hence are not suitable for the requirements of single-molecule microscopy. Novel, *in situ* cross-linked hydrogels might offer an interesting alternative for the immobilization of trypanosomes. Hydrogels constitute a group of polymeric materials which form three-dimensional structures and are capable of holding large amounts of liquid solutions [106]. The stiffness of these hydrogels depends on the polymer concentration and is thus adjustable [107]. Different hydrogels with various compositions have been developed within recent years, motivated by the growing interest to use them as cell culture materials to mimic native cellular milieus. Hydrogels based on polymers like alginate and gelatin are widely available and often used as scaffolds [108], however, many more materials have been tested. Various chemical gel formation processes are known to be cytocompatible with thiol-ene reactions being one of the most prominent mechanism [109].
The fast gelation, stiffness and high cytocompatibility of hydrogels make them an interesting candidate for their application as embedding material for trypanosomes. In this work, different hydrogels were tested for their suitability as immobilization reagents for single-molecule microscopy of living trypanosomes.

2. Results

The defense mechanisms of trypanosomes against recurring host immune responses in the bloodstream relies among others on the shielding function of the VSG coat. The biophysical properties of this dense and dynamic structure are not yet understood in detail and of major interest of this work. Previous studies used fluorescence recovery after photobleaching (FRAP) in living trypanosomes and artificial bilayers to address this issue [100, 105]. The method, however, averages information of a multitude of VSGs to an ensemble result and provides limited insights into the detailed behavior of single VSGs. Furthermore, the resolution of the technique is restricted to the micrometer and second range. To overcome these limitations, state-of-the-art single-molecule fluorescence microscopy was introduced as a tool for a more precise analysis of VSG dynamics *in vivo* and in artificial lipid bilayers. The high spatial and temporal resolution of the technique could provide novel insights into the biophysical properties of single VSGs and the VSG coat.

2.1 Single-molecule microscopy in artificial lipid bilayers

2.1.1 Single-particle tracking of VSGs and lipids in artificial lipid bilayers

In order to verify the capability of the microscope setup for the detection of single molecules, fluorescently labeled VSGs M1.6 and lipids (DOPE488) were integrated into preformed SLBs and their lateral motion was recorded. To this end, membrane proteins were extracted from living trypanosomes using a trifluoroacetic acid based assay (Section 4.2.6) and the membrane form VSGs M1.6 were purified from these extracts via HPLC. Specific VSG M1.6 antibodies were used to confirm the purification (see Supplementary Figure 7 in [91] for an example western blot of VSG detection), with typical yields of 0.5-1 mg of VSGs M1.6 per 3-5 x 10^9 *T. brucei* cells. The purified VSGs M1.6 were fluorescently labeled via ATTO647N-NHS-ester (DOL< 0.1, VSG M1.6 ATTO647N) and subsequently integrated into preformed SOPC bilayers at low protein densities (Section 4.2.7). The samples were illuminated at λ_{640} nm (VSG M1.6 ATTO647N) or λ_{515} nm (lipids) for 10 ms at a mean intensity of 2 kW cm^{-2} with a time lag of 36 ms between consecutive frames. Multiple movies with in total 20000 frames were recorded at various positions in the sample. A sequence of exemplary background subtracted images showed diffraction limited spots spatially distributed within the ROI (19.2 x 19.2 μm) at varying positions of VSGs M1.6 ATTO647N (Figure 2.1, a-d) or lipids (Figure 2.1, f-i) in consecutive images. The 3D-intensity profiles of individual spots illustrated that specific fluorophore signals were considerably more intense than the image background (Figure 2.1, e, j). Image processing was performed in order to localize single molecules with high precision as described in Section 4.2.9. False-positive signals were removed from the data

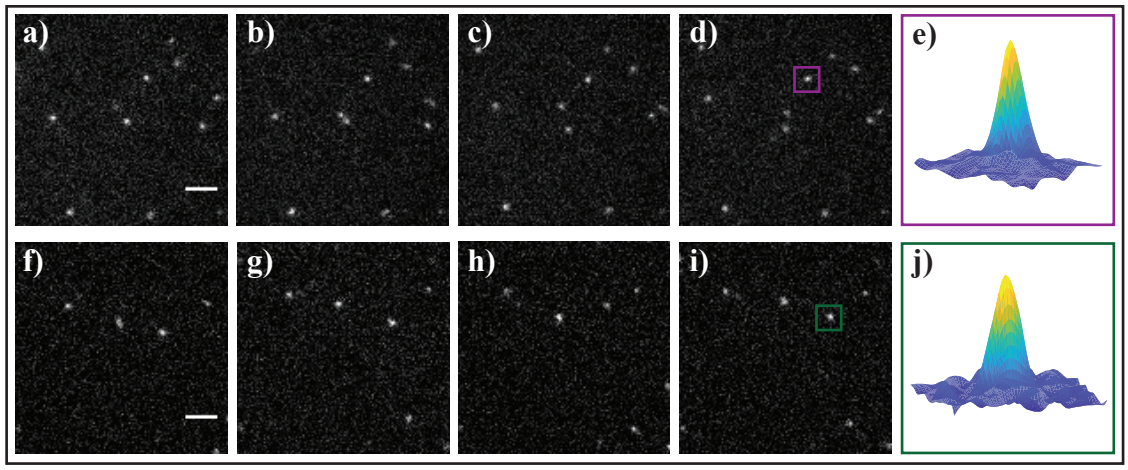

Figure 2.1: Exemplary fluorescence snapshots of fluorescently labeled VSGs and lipids in SLBs. Single-molecule spots of VSG M1.6 ATTO647N (a-d) and DOPE488 (f-i) integrated into preformed lipid bilayers at low densities. 3D-intensity profile of a single VSG M1.6 ATTO647N (e) and DOPE488 (j) marked by a red square and green square, respectively. The time lag between consecutive images was 36 ms. The scale bar is 3 μm and valid for a-d) and f-i).

set by setting thresholds at 200 counts (VSG M1.6 ATTO647N) and 20 counts (DOPE488). In total, $\sim$ 8.9*10^4 VSG M1.6 ATTO647N were localized in all image sequences with an average of 4.5 molecules per frame. The intensities of all peaks were found to be approximately described by a Gaussian distribution (Figure 2.2, purple bars) with a mean value of 517 counts and a standard deviation (s.d.) of 60 counts. A comparison to signals that resulted from the camera noise or sample background (Figure 2.2, inset: purple bars) illustrated that ATTO647N signals were clearly distinguishable from background noise. The signal-to-noise ratio was calculated from the mean value of the signal intensities distribution and the standard deviation of the background noise and was found to be 67. Summation of all single-molecule profile widths further yielded a value of 0.36$\pm$0.02 μm (mean $\pm$ s.d.). Overall, single VSG M1.6 ATTO647N molecules diffusing in the SLBs could be localized with a precision of 15$\pm$6 nm.

For lipid samples, $\sim$7*10^4 molecules were localized in all image sequences (3.5 DOPE488 molecules per frame). The intensities of all DOPE 488 molecules were also found to be approximately described by a Gaussian distribution with a mean value of 253 counts and a s.d. of 45 counts (Figure 2.2, green bars). The background noise was measured to be generally low in the green image channel with a mean value of 7 counts and a s.d. of 2 counts (Figure 2.2, inset: green bars). The mean profile width of all DOPE488 molecules was determined to be 0.33$\pm$0.06 μm. A high signal-to-noise ratio (55) resulted in a mean localization of precision of 20$\pm$6 nm.

The presented data showed, that single VSGs M1.6 ATTO647N and DOPE488 lipids were successfully detected at the microscope setup and quantified with respect to their

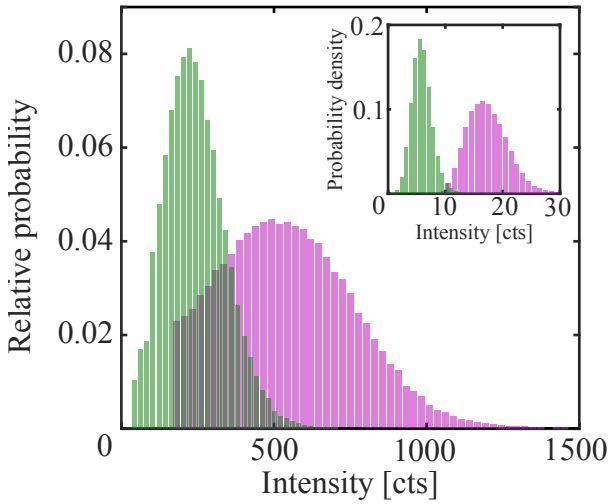

Figure 2.2: Single-molecule intensities of VSG M1.6 ATTO647N and DOPE488 in SOPC bilayers. The histograms show the relative probability of intensities derived by Gaussian fitting of single-molecule peaks. Thresholds were set at 200 counts (VSG M1.6 ATTO647N) and 20 counts (lipids) to remove false-positive background signals from further analysis. Inset: histogram of background intensities measured in the dark-red (purple bars) and green (green bars) color channel in SOPC bilayers.

single-molecule footprint. Further, a high signal-to-noise ratio facilitated the localization of individual molecules with high spatial precision. In order to confirm the reliability of the single-molecule detection method, single-molecule positions were plotted over a fluorescence movie. Usually, good results were achieved (see Figure 6.1).

In a next step, individual trajectories were generated from single-molecule positions. The tracking algorithm applied, calculates the probability of a molecule in an image to be related to a molecule in the consecutive image (Section 4.2.9) based on an initial guess of the particle diffusion coefficient (D_{in}). In order to chose the correct diffusion coefficient as an input parameter for the analysis, a preliminary, repetitive tracking of one data set with varying D_{in} values was performed using 15-20 successive steps in the range of 0.01-3.5 $\mu m^2\ s^{-1}$ (Figure 2.3, A). For each case the D_{out} was calculated and the correct D_{in} was chosen in a range where the calculated D_{out} values became independent of D_{in}.

Increasing the D_{in} values stepwise from 0.01-1 $\mu m^2\ s^{-1}$ affected the calculated diffusion coefficients strongly and resulted in D_{out} values of 0.01-2 $\mu m^2\ s^{-1}$ for lipids and 0.01-1.3 $\mu m^2\ s^{-1}$ for VSG M1.6 ATTO647N (Figure 2.3 A). The further increase of D_{in} up to 3.5 $\mu m^2\ s^{-1}$ increased the resulting D_{out} only $\sim$1.5 x in both samples. This relative independence of the input variable on the resulting output was an indication for the correct estimation of the diffusion coefficient. Thus, final D_{in} values of 2 $\mu m^2\ s^{-1}$ and 2.8 $\mu m^2\ s^{-1}$ were chosen for VSG M1.6 ATTO647N and DOPE488, respectively. The tracking algorithm was repeated for both data sets to generate the final trajectories. $\sim$2400 trajectories of variable length were derived from the initial VSG M1.6 ATTO647N

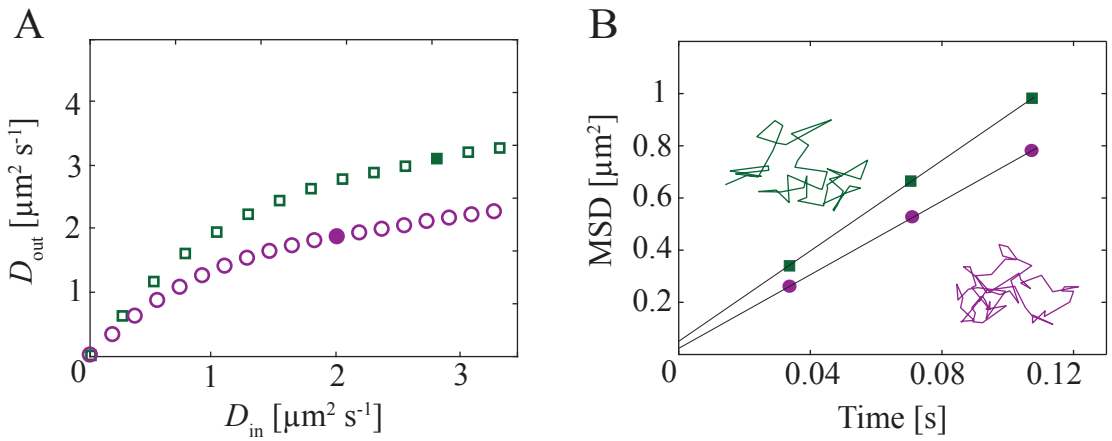

Figure 2.3: D_{in} versus D_{out} analysis of VSG M1.6 ATTO647N and DOPE488 and calculation of D via MSD analysis. A) Repetitive D_{in} versus D_{out} analysis for the estimation of VSG M1.6 ATTO647N (magenta circles) and DOPE488 (green boxes) diffusion coefficients. The final D_{in} values chosen for the generation of particle trajectories are marked as a filled circle and box, respectively. B) MSD analysis of VSG M1.6 ATTO647N and DOPE488 trajectories (magenta and green, respectively) and linear fit to the first three data points.

localizations with a weighted mean trace length of 54 localizations. For the lipid samples, ∼3600 trajectories were obtained with a weighted mean trace length of 13 localizations. The shorter trace length in the lipid case resulted from early bleaching of DOPE488 molecules. In order to verify the tracking algorithm, example trajectories were further plotted over fluorescence movies together with the previously determined single-molecule localizations (see Figure 6.1). Usually, good agreement of single-molecule positions and derived trajectories was obtained.

Next, a mean-square displacement (MSD) analysis was performed as explained in Section 4.2.9. The trajectories were categorized as immobile or mobile by comparing their MSDs with the achieved localization precision and the percentage of the mobile fraction was determined on the level of trajectories. The mobile fractions were found to be high for VSG M1.6 ATTO647N (97%) and DOPE488 (99%). This indicated homogeneous, defect free underlying SLBs that allowed a high mobility of the incorporated molecules. A close inspection of the MSD analysis showed, that the MSD increased linear with time, as expected for free particle diffusion (Figure 2.3, B). The diffusion coefficients were calculated from a linear fit to the first three data points and found to be 1.75±0.03 μm^2 s^{-1} for VSG M1.6 ATTO647N and 2.22±0.03 μm^2 s^{-1} for DOPE488.

The presented results show, that the fluorescence microscope setup was successfully applied to detect and quantify single VSG M1.6 ATTO647N and DOPE488 integrated into SLBs. Image processing and data analysis facilitated the generation of single-particle trajectories and allowed the determination of the mobile fraction and diffusion coefficient for both molecules.

2.1.2 Impact of N-glycosylation on the diffusion of VSG in SLBs

VSGs expressed on the surface of living trypanosomes are modified by one ore multiple N-linked glycan chains. The impact of this modification on lateral diffusion *in vivo* was studied by Andreas Hartel as a part of his doctoral thesis using the method of fluorescence recovery after photobleaching (FRAP) [118]. He found that removing N-glycans in trypanosomes which expressed VSG M1.6 or VSG M1.4 did not alter the VSG diffusion coefficients on the cell surface but reduced their mobile fractions [105, 118]. This study was further extended to an artificial lipid bilayer system, where purified VSG M1.6 or its N-glycan deficient mutant form (VSG M1.6$_{mut}$) were reconstituted at different protein densities. Indications for a density depended decrease of the VSG diffusion coefficient were found with N-glycosylation facilitating VSG mobility at high protein densities.
To verify these results, the measurements were repeated for a broad range of reconstituted protein concentrations. Furthermore, to study VSG diffusion *in vitro* beyond the resolution limits of FRAP, state-of-the-art single-molecule tracking experiments were performed on the same samples.
First, VSG M1.6 and VSG M1.6$_{mut}$ were extracted from living trypanosomes and subsequently purified as explained in Section 4.2.6. The trypanosomes expressing the N-glycan deficient form were generated by Nicola Jones using site directed mutagenenis (Jones *et al.*, in preparation). Purified VSG M1.6 ATTO488 and its N-glycan deficient form were each reconstituted into supported lipid bilayers at variable protein densities (Section 4.2.7). Ensemble VSG M1.6 ATTO488 diffusion coefficients and the mobile fractions of the individual samples were then determined using FRAP. The average free protein distances in the reconstituted VSG M1.6 ATTO488 samples were calculated from the determined lipid-to-protein ratios (Section 4.2.7). The results of these measurements are presented as a plot of the diffusion coefficients against the average free protein distances (d_{free}) (Figure 2.4).
The diffusion coefficients of VSG M1.6 ATTO488 were found to be around 1.10 $\mu m^2\ s^{-1}$ at d_{free} > 7 nm (Figure 2.4, A). Upon further increase of the lateral VSG M1.6 ATTO488 concentration, the diffusion coefficient decreased linearly to a minimum of 0.10$\pm$0.09 $\mu m^2\ s^{-1}$ at the maximum protein density studied. The critical density at which the diffusion became strongly dependent on the protein density corresponded to a d_{free} of 5-7 nm and was named the molecular crowding threshold (MCT) for VSG M1.6 ATTO488. A density depended decrease was also measured for the mobile fraction of VSG M1.6 ATTO488, which was > 80 % below the MCT and decreased to 39 $\pm$11 % at the maximum density (Figure 2.4, B). The diffusion coefficients of N-glycan deficient VSGs M1.6 ATTO488 were comparable to those measured for VSG M1.6 ATTO488 in samples of low protein concentration (D = 1.0$\pm$0.2 $\mu m^2\ s^{-1}$ for distances > 14 nm). The MCT, however, was already reached at a d_{free} of 12-14 nm and the diffusion coefficient was strongly reduced

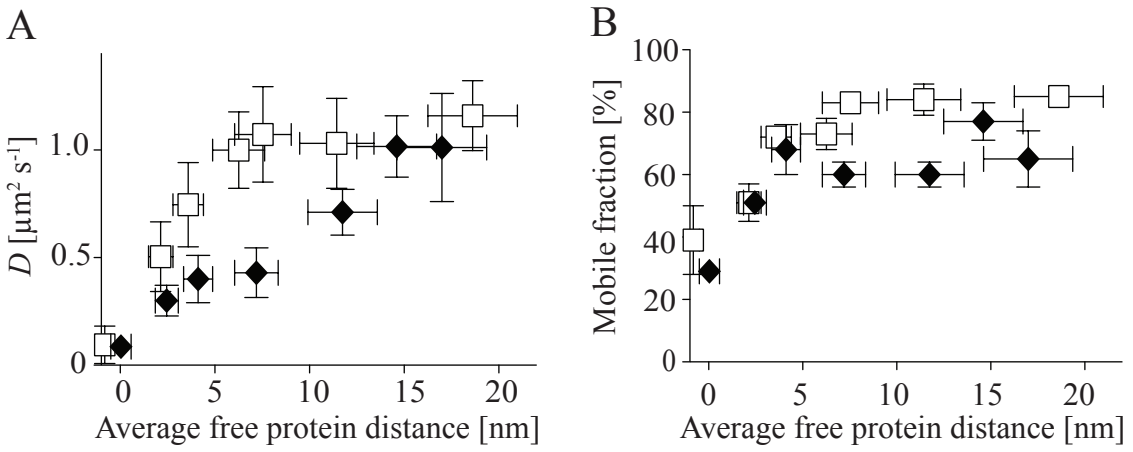

Figure 2.4: Impact of N-glycosylation on the diffusion of VSG in SLBs. A) Impact of the lateral protein density of reconstituted VSG M1.6 ATTO488 (grey boxes) and its N-glycosylation deficient mutant (black diamonds) on the diffusion coefficient (*D*). B) Mobile fraction of the reconstituted protein samples. The error bars represent the standard deviation of the mean (y-axis) or depict the range (x-axis).

upon further increase of the protein concentration. In the regime of the MCT of VSG M1.6 ATTO488, the diffusion coefficient of VSG M1.6$_{mut}$ ATTO488 was already reduced 2.5 x (D = 0.43±0.12 μm^2 s^{-1}) and was measured to be 0.09±0.02 μm^2 s^{-1} at the maximum density. The mobile fraction of the VSG M1.6$_{mut}$ ATTO488 was generally low in diluted samples (∼60%) and decreased to 29±2 % in the densest samples.

These results show that VSGs were successfully reconstituted into SLBs at various proteins concentrations. Measurements of the diffusion coefficients revealed that a critical VSG concentration exists, above which a density dependent decrease of the diffusion coefficient and mobile fraction was observed. Further, the removal of N-linked glycans from VSG M1.6 affected this threshold and a reduced diffusion and mobility were already measured at lower protein concentrations. Hence, N-glycosylation facilitates high mobile fractions at low protein concentrations as well as high diffusion coefficients in the range of the MCT. In order to determine whether the observed effects are relevant for BSF trypanosomes, the densities of the reconstituted VSG coats were compared to the *in vivo* situation. An immuno-histochemical approach was performed to convert the protein densities of reconstituted coats into surface equivalents (SE) of live cells (Section 4.2.7). A value of SE = 1 thereby corresponds to the surface VSG concentration found *in vivo*. Reconstituted VSG M1.6 ATTO488 and VSG M1.6$_{mut}$ ATTO488 samples with the lowest protein concentration were equivalent to 0.6±0.1 and 0.9±0.2 SE, respectively (Figure 2.5). Samples with the highest protein concentration contained each around twice the amount of VSG found on the cell surface. The tested concentration regime represented a broad range of VSG concentrations, equivalent to either diluted or over-expressed SE. The previously determined MCT of VSG M1.6 ATTO488 (Figure 2.4, A) was found to be equivalent to

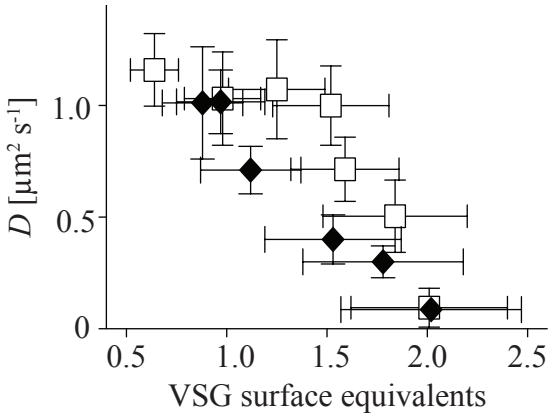

Figure 2.5: VSG diffusion as a function of VSG surface coat equivalents. The impact of lateral VSG M1.6 ATTO488 (white boxes) and VSG M1.6$_{mut}$ ATTO488 (black diamonds) densities on the previously determined diffusion coefficient, *D*, (Figure 2.4) were quantified in relation to the VSG concentrations on the cell surface. A relative concentration of 1 corresponds to the concentration found *in vivo*. The error bars represent the standard deviation (y-axis) of the mean or depict the range (x-axis).

1.5 x SE. This illustrates that the VSG coat operates close to its MCT. As it was shown, the MCT of VSG M1.6 ATTO488 corresponds to a highly dense VSG arrangement. This is in good agreement with the general accepted view of the VSG coat as a dense barrier that shields underlying proteins [90]. Further, the presented data illustrate that trypanosomes could actually harbor 50 % more VSG on their cell surface before a density dependent decrease of VSG diffusion would occur. It would indeed make sense for trypanosomes to transiently adjust the VSG density on their cell surface without affecting the diffusion coefficient of VSGs, e.g. in the case of antigenic variation. In such a scenario, two distinct VSG populated the cell surface simultaneously. Experiments showed, that ectopic VSG overexpression raised the level of surface VSG to roughly 140% [105]. The FRAP measurements illustrated, that the diffusion coefficient is yet not impaired at such concentrations (Figure 2.5). For the N-glycan deficient mutant, the MCT was close to one SE. This suggests that a further increase in VSG concentration would directly impair protein mobility. In the case of antigenic variation, the diffusion coefficient would transiently be reduced to $\sim$ 50% of its initial value.

To study the lateral diffusion of VSG in SLBs beyond the spatial and temporal resolution limits of FRAP ($\sim$1 μm and $\sim$1 min), complementary single-molecule tracking was further performed. To this end, the same proteins samples that were measured via FRAP were further incubated with trace amounts of VSG M1.6 ATTO647 or VSG M1.6$_{mut}$ ATTO647. The incorporation of single VSGs from the membrane supernatant was monitored at the microscope and the membranes were washed thoroughly as soon as the desired protein concentration was reached. Image acquisition was then performed as described in Section 4.2.8. For VSG M1.6 ATTO647 a ROI of 19.2x19.2 μm was recorded at 28 Hz, the diffu-

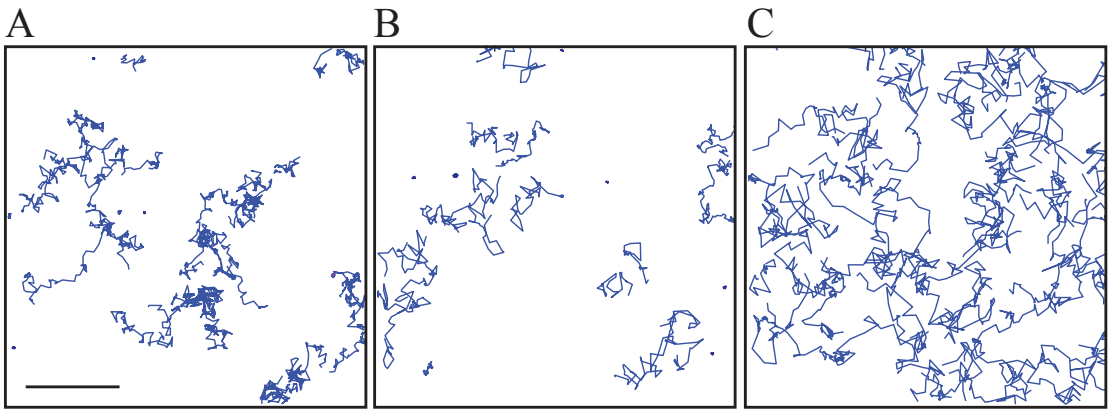

Figure 2.6: Example trajectories of laterally diffusing ATTO647N labeled VSG M1.6$_{mut}$ in reconstituted VSG M1.6$_{mut}$ samples of different protein densities. The protein concentrations correspond to average free protein distances of ∼0 (A), 2.5 (B) and 17 (C) nm as presented in Figure 2.4. The trajectories include immobile particles, which were removed from further data analysis. The scale bar is 5 μm and valid for A-C).

sion of VSG M1.6$_{mut}$ ATTO647 was monitored at 42 Hz in a ROI of 10.2x10.2 μm. More than 10 movies with each 1000 frames were recorded using identical sample illumination times (10 ms) and intensities (2 kW cm^{-1}) for both samples. Single-VSG molecules were localized in all frames as described previously (Section 4.2.9) and trajectories were generated after a D_{in} versus D_{out} analysis (Section 4.2.9). Figure 2.6 depicts example trajectories of single VSG M1.6$_{mut}$ ATTO488 diffusing laterally in membranes of different protein densities. The protein concentrations correspond to average free protein distances of ∼0 (A), 2.5 (B) and 17 (C) nm as presented in Figure 2.4.

In total, 3.1*10^5 VSG M1.6 ATTO647 molecules were localized with a precision of 14±9 nm. From these, 2523 trajectories were generated. For each condition, a minimum number of 200 trajectories were obtained and analyzed further. The weighted mean trace length of all trajectories was found to include > 70 localizations. In reconstituted VSG M1.6$_{mut}$ ATTO647 samples, 9.9*10^5 molecules could be localized with a precision of 14±8 nm. Trajectories were generated (N = 12074) from single-molecule localizations and a weighted mean trace length of > 70 localizations was determined. Immobile proteins were detected and removed from further analysis. The diffusion coefficients were finally calculated for the remaining mobile particles in a MSD analysis by averaging the information of all trajectories. The analysis method summarized a set of observations and only insufficiently characterizes the dynamics of a single trajectories. However, it facilitated the comparison to the previously obtained results from FRAP measurements. The results were plotted against the average free protein distance previously determined for the FRAP experiments (Figure 2.7).

The diffusion coefficients calculated from the MSD analysis were in good agreement with the diffusion coefficients previously determined via FRAP (compare Figure 2.4 A

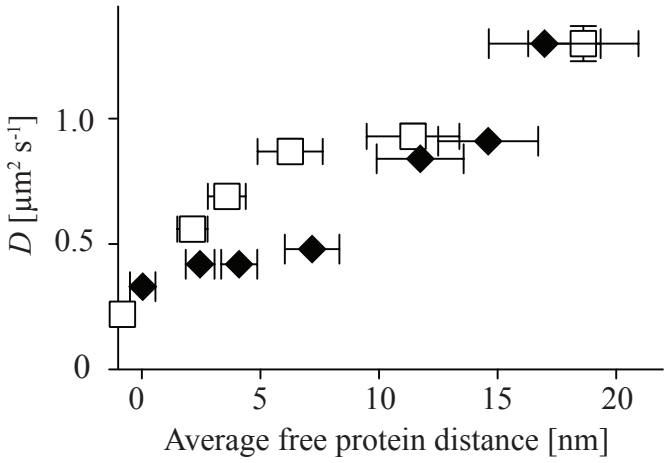

Figure 2.7: Impact of N-glycosylation on the diffusion of VSG in SLBs analyzed by single-particle tracking. The same VSG samples that were measured via FRAP were further doped with trace amounts of ATTO647N labeled VSGs. The diffusion coefficients of VSG M1.6 ATTO647N (white box) and VSG$_{mut}$ ATTO647N (black diamonds) were calculated for the freely diffusing populations. The error bars represent the standard deviation of the mean (y-axis) or depict the range (x-axis).

and Figure 2.7). In the most dilute situations, diffusion coefficients of 1.3 $\pm$0.07 μm^2 s^{-1} and 1.3 $\pm$0.02 μm^2 s^{-1} were calculated for VSG M1.6 ATTO647 and VSG M1.6$_{mut}$ ATTO647, respectively. An increase in the protein concentration decreased the diffusion coefficients of both proteins. In the most dense samples, they were measured to be around 0.22-0.33 μm^2 s^{-1}. At of the previously determined MCT of VSG M1.6 ATTO488 a two-fold higher diffusion coefficient was measured for VSG M1.6 ATTO647 compared to VSG M1.6$_{mut}$ ATTO647. Interestingly, the mobile fraction of both proteins was high (>90%) and independent of the protein concentration (data not shown).

The results from SMFM confirm the previously measured effect of the lateral protein density on the VSG diffusion coefficient. The difference in the diffusion coefficients of VSG M1.6 and its N-glycosylation deficient form at the MCT of VSG M1.6 emphasizes the importance of N-glycosylation for the lateral VSG mobility. The constant diffusion coefficient of VSG M1.6 at lateral protein densities of 5-12 nm appears to be an important feature of surface VSGs because this range was found to be equivalent $\sim$ 1-1.5 SE (Figure 2.5) and thus, represents the VSG concentrations found on the surface of living trypanosomes. In contrast to the results form FRAP experiments, the measured diffusion coefficients in SMFM above the MCT were not purely independent of the protein concentration. VSGs in the most diluted samples exhibited the highest diffusion coefficients ($\sim$ 1.3 μm^2 s^{-1}). The results from single-molecule tracking experiments presented in Section 2.1.1 suggest that a further dilution might lead to higher VSG diffusion coefficients. The mobile fractions determined in SMFM were high (> 90%) and independent of the protein density. This was not observed in FRAP experiments. Further, M1.6$_{mut}$ ATTO488 exhibited generally

reduced mobile fractions above the MCT of VSG M1.6 ATTO488. It it questionable whether this finding is attributed to the limitations of FRAP or represents a general feature of N-glycosylation. In order to fully extract the additional information accessible with single-molecule experiments (e.g. information about protein populations with different diffusion behavior or dynamic changes of the behavior within one trace) the trajectories have to be analyzed in more detail. This analysis is performed in collaboration with Mislav Cvitković and Ana-Sunčana Smith and is work in progress. Preliminary results of the analysis are discussed in Section 3.1.4.

2.1.3 VSG conformation and lateral diffusion

The VSG coat is the most prominent defense mechanism of trypanosomes against the host immune system. Despite the importance of the VSG coat for the parasitemia of trypanosomes, no structure of a complete VSG has been reported so far. Attempts to crystallize a full size VSG failed because of the high accessibility of the flexible linker region between C- and N-terminal domains region to protease activities. Recently, Thomas Bartossek and Nicola Jones used small-angle X-ray scattering to combine the information of individual high-resolution structures to elucidate the first complete VSG structure [91]. This was performed for VSG M1.1 and VSG I1.24 (ILTat1.24: Protein Database ID: 2VSG and 2JWG, 2JWH). They found, that the linker region allows great flexibility between the domains and suggested that VSGs can adopt two main protein conformations. This flexibility of the protein might be relevant for the protein to be able to avoid obstacles on the cell surface and to adjust to different surface protein densities, while still maintaining a protective function on the cell surface.

In order to test this hypothesis, single-molecule tracking experiments were performed on VSG M1.1 ATTO647 diffusing in SLBs. The experiments were carried out at low protein densities ($\sim$0.09 VSG per μm^2) to minimize protein-protein interactions. As a control for the quality of the SLBs, DOPE488 lipids were further integrated into the same bilayers. SMFM was performed in both color channels, followed by single-molecule localization and the generation of trajectories as described before (Section 4.2.8 -4.2.9).

VSGs M1.1 ATTO647N and DOPE488 lipids were localized with a precision of 16$\pm$7 nm and 19$\pm$6 nm, respectively. From all single-molecule positions, a total number of 2969 trajectories with variable lengths ($20 < n_{steps} < 1263$, $\langle n_{steps} \rangle = 49$) were generated for the proteins. For the lipid sample, 1890 trajectories ($9 < n_{steps} < 84$, $\langle n_{steps} \rangle = 13$) were obtained. The single-molecule trajectories were analyzed by collaboration partners (for details see [91]). In a first step, the quality of the lipid bilayer was evaluated by analyzing the diffusion of single DOPE488 lipids. After excluding trajectories that showed non-Brownian characteristics (immobile particles), a single lipid population remained that exhibited a mean diffusion coefficient of 2.688$\pm$0.005 $\mu m^2\ s^{-1}$. The mobile fraction of the lipid was high (> 95%), suggesting a lipid bilayer free of substantial membrane defects. The analysis was then performed for VSG M1.1 ATTO647N. First, immobile particles were removed from the set of all VSG M1.1 ATTO647N trajectories. The immobile fraction was found to be low and in the same range as for DOPE488 lipids. In contrast to DOPE488, more than one population was detected for VSG M1.1 ATTO647N. The plot of the square step length (l^2) of exemplary mobiles particles clearly suggested the existence of two mobile subpopulations of VSG M1.1 ATTO647N in a SLB (Figure 2.8).

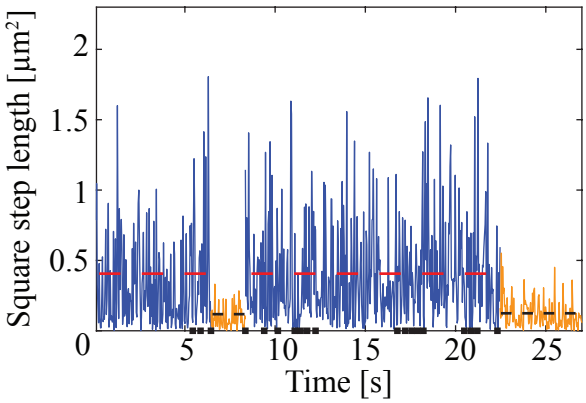

Figure 2.8: The square of measured VSG M1.1 step length as a function of time. A representative set of 22 VSG M1.1 ATTO647N trajectories is presented after the removal of immobile molecules. Fast (blue) and slow (orange) diffusion of VSG M1.1 ATTO647 were detected. The mean square step length is indicated with a dashed red (fast) and dashed orange (slow) line. Individual trajectories are separated by black squares on the x-axis.

Distinct mean values of l^2 were found for fast ($l^2 = 0.41\ \mu m^2$) and slow ($l^2 = 0.12\ \mu m^2$) diffusing VSG M1.1 ATTO647N (Figure 2.8, dashed red and black lines, respectively). Summarizing these information in a MSD analysis as performed in Section 2.1.2 would inevitably lead to a loss of information on the dynamics of such subpopulations. Hence, the trajectories were further analyzed in order to classify VSG M1.1 ATTO647N trajectories as fast or slow. The method included among others thresholding and the calculation of probability likelihoods (for a proper description of the analysis method see [91]). For each data set a MSD analysis was then applied (i) for individual trajectories to generate the probability density distribution of diffusion coefficients (Figure 2.9, A) and (ii) for a single cumulative trajectory to calculate the time-averaged MSD (Figure 2.9, B).
From the probability density distribution a mean diffusion coefficient of 2.87±0.03 (1.08) $\mu m^2\ s^{-1}$ and 0.81±0.05 (0.3) $\mu m^2\ s^{-1}$ were derived for the fast and slow population, respectively. The numbers in brackets represent the standard deviation of the distribution. A clear overlap in the diffusion coefficients of both populations was observed from the plot of probability density distributions. Nevertheless, the applied analysis method facilitated a clear classification of individual VSG M1.1 ATTO647N trajectories and allowed the calculation of the specific population diffusion coefficients.
The time-averaged MSD analysis revealed similar diffusion coefficients. They were found to be 2.716±0.005 $\mu m^2\ s^{-1}$ and 0.848±0.002 $\mu m^2\ s^{-1}$ for the fast and slow population, respectively. The diffusion coefficients were in good agreement with the results from the probability density distribution of diffusion coefficients. The time-averaged MSD analysis is analog to the analysis method applied in Section 2.1.2.
In conclusion, the analysis of single VSG M1.1 ATTO647 trajectories revealed that two distinct populations of the protein can exist in a SLB. The molecules from both popu-

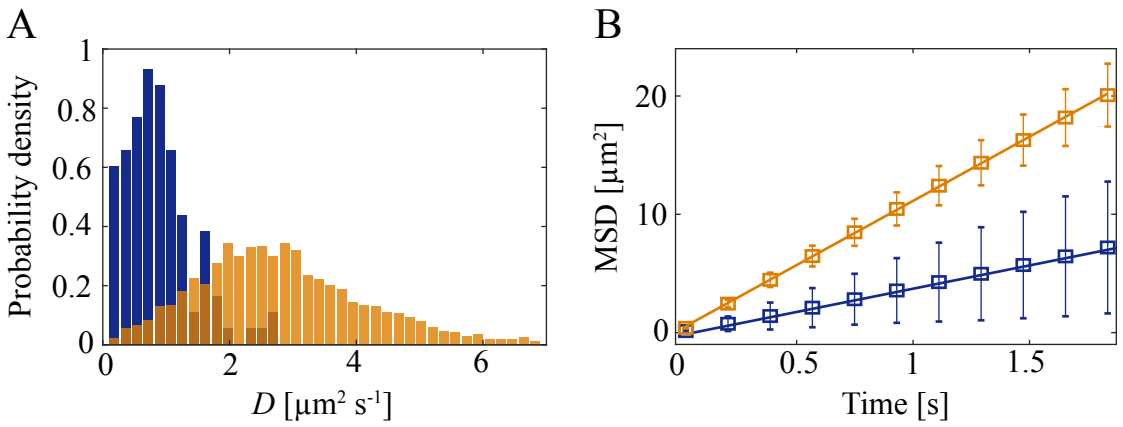

Figure 2.9: Diffusion characteristics of VSG M1.1 incorporated into SLBs. A) Histogram of VSG M1.1-ATTO647N diffusion coefficients of the fast (orange) and slow (blue) free moving populations. The diffusion coefficients were derived from a MSD analysis of individual trajectories. B) Mean square displacement as a function of time for the fast (orange) and slow (blue) free moving populations, calculated from a single concatenated trajectory for each population.

lations showed Brownian diffusion characteristics and exhibited distinct mean diffusion coefficients, which were in the same order of magnitude. The analysis method facilitated a clear categorization of individual VSG M1.1 ATTO647N trajectories, even though a significant overlap in the diffusion coefficients existed for trajectories from individual populations. The analysis method provided novel insights into the biophysical behavior of single VSG molecules in a membrane. Notably, the mean diffusion coefficient of the fast population was considerably higher than the diffusion coefficient calculated for VSG M1.6 at low lateral protein densities (1.75 ± 0.03 μm^2 s^{-1}, Section 2.1.1). The discrepancy might be explained by the differences in the analysis methods. In Section 2.1.1 VSG M1.6 ATTO647N trajectories were not examined for the existence of subpopulations. The MSD analysis was performed for all trajectories and hence, represents the mean value of the diffusion coefficient of potential subpopulations. Further, the mean diffusion coefficient of the fast population is similar to that calculated for DOPE488. This is surprising, since Hartel et al. have shown that the size proteinaceous part clearly affects the diffusion coefficient of GPI-anchored proteins [20]. VSGs posses a large protein domain and hence, a diffusion coefficient slower than that of a lipid would be expected.

Nevertheless, the appearance of two distinct populations is reflective for the structural findings of Bartossek et al. [91]. The authors presented two major conformations for VSG M1.1 attached to a membrane. A compact conformation with an extended structure, and a relaxed conformation that protrudes less wide from the membrane but occupies larger areas. The compact VSG conformation is believed to appear in dense protein arrangements and facilitate a high protein mobility in such a scenario. Both conformational states might posses individual characteristics (e.g. interaction with the membrane) that affect the diffu-

sion of VSGs. The distinct populations of diffusing VSGs determined in this section are reflective for such properties.

2.1.4 Simultaneous two-color single-molecule fluorescence microscopy

Two-color fluorescence imaging can be performed by separating the emission light of individual types of fluorophores in space or time. Traditionally, electronic filter changers are used to detect specific emission signals. The switching speed of such devices substantially limits the temporal resolution of the imaging process. Alternatively, sequential sample illumination with different laser lines can be applied using an acousto optic tunable filter (AOTF) and the emission light can be detected separately in time. The switching speed of AOTF sates is substantially faster then the change of filter positions in a microscope and facilitates faster acquisition times. However, the consecutive imaging of multiple color channels results in imaging cycle times that are limited to the maximum frequency divided by the number of color channels. For highly dynamic processes, fast imaging types can be a prerequisite and sequential imaging of different types of fluorophores might be of disadvantage. Further, the lag in time between the images limits quantitative studies of a temporal correlation between different types of molecules. Such studies might provide information about e.g. the temporal interaction between two molecules. As an example, the interaction of VSGs and specific antibodies could be studied in a SLB. Further, two distinct VSG types could be integrated into the same SLB and they could be monitored simultaneously. Such an experiment would mimic the situation of early antigenic variation on the cell surface.
As a solution, emission lights from different fluorophores can be separated using an appropriate beamsplitter in combination with a second camera. The arrangement facilitates simultaneous two-color fluorescence microscopy but adds significant extra costs to the user. In order to facilitate simultaneous two-color single-molecule fluorescence microscopy without the disadvantage of such extra costs an experimental set up was chosen that allows to simultaneously image two color channels spatially separated on one EMCCD camera chip. To this end, an emission light image splitter (Optosplit II) was implemented into the microscope setup. The device was mounted in front of the EMCCD (see Figure 4.1). The central component of the device is a dichroic mirror with a cutoff in the range of 640 nm that facilitates the separation of the emission light. The separated light paths were projected onto specific areas of the sensor chip of the EMCCD camera via an arrangement of mirrors inside the image splitter. The spatial separation of the emission light facilitated a clear distinction of differently colored fluorophore signals. Using such a microscope setup for studying spatially correlated processes, however, necessitated additional image processing to precisely register the images of both color channels. It had to be considered that axial

and lateral chromatic aberration occurs when different wavelengths are focused through an optical lens. Axial chromatic aberration describes the color aberration that is caused by the variation in depth of the focal point for different wavelengths. For simultaneous two-color imaging this implied that single-molecule spots of one color channel were imaged blurred when the other color channel was focused. To minimize the effect of the blurring on the identification of single molecules, the focal plane was set between the focal points of both color channels. For lateral chromatic aberration, different colors are in focus in the same plane, but distortions occur between lateral positions. The distorting effect of lateral chromatic aberration is larger towards the corners of an image. Even though such distortions might be small compared to the diffraction limit, the high localization precision of SMFM requires the correction of lateral chromatic aberrations when studying spatially correlated processes [110].

In this work fixed reference point-source beads visible in both color channels were imaged at the microscope to achieve an exact spatial correlation between the two detection channels. The bead localizations were used to generate a transformation mask in Matlab as e.g. described by Semrau et al. [53]. The transformation mask was applied to the images from two-color experiments to precisely register both image channels.

Multi-fluorescent TetraSpeck microshpheres immobilized on a glass support were chosen as reference objects (Section 4.2.10). The separation of the two color channels was achieved by manually rotating the mirrors of the beamsplitter along the horizontal axis until a clear image separation was achieved (Figure 2.10, A). For the applied camera orientation (facing downwards with attached cables pointing up) this resulted in a horizontal image separation on the EMCCD chip.

Typically, 10 movies with each 1000 consecutive frames were acquired at 28 Hz (10 ms illumination at λ_{515} and λ_{640}, 2 mW laser power, respectively). The microscope stage was slowly moved manually above the objective lens while recording the movies in order to image a multitude of beads homogeneously distributed within both ROIs. This was performed, because the quality of the image registration process was shown to benefit from large numbers of homogeneously distributed reference objects in the images [53]. Next, the beads were localized in both image channels as described in Section 4.2.9.

Exemplary results from the localization of the TetraSpeck beads and the subsequent image registration are presented in this work. For the example experiment, 56049 TetraSpeck beads were localized in the green color channel (ROI_{green}) with a precision of 5 ± 2 nm (Figure 2.10, B, green circles). In the red image channel ($\mathrm{ROI}_{magenta}$), 56903 molecules were localized with a precision of 5 ± 2 nm (Figure 2.10, B, red circles). The small difference in numbers of localizations resulted from erroneous single-molecule identification. The list of coordinates from bead localizations in both color channels served as the input to register both image channels. For that purpose, a program was written in Matlab that included the following steps:

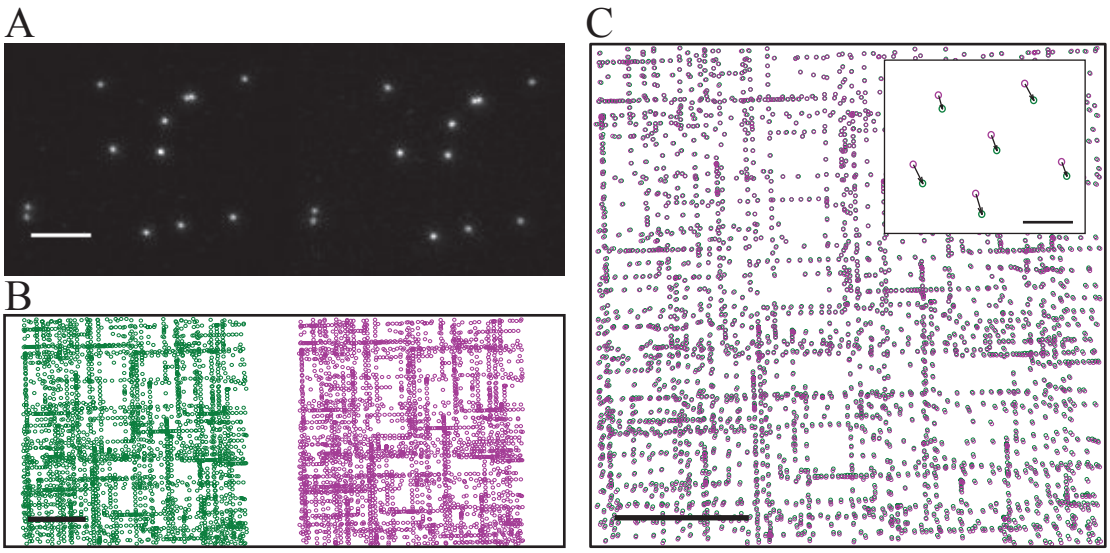

Figure 2.10: Correction for the horizontal offset in two-color single-molecule fluorscence microscopy. A) Fluorescence image of immobilized multi-fluorescent TetraSpeck beads in both color channels (λ_{515} left area, λ_{640} right area). The scale bar is 5 μm. B) Plot of a small fraction of single-molecule localizations from a movie of a two-color experiment in a ROI of 19.2 x 48 μm. Green circles represent single-molecule localizations in the green channel, magenta circles depict single-molecule localizations in the red channel. The scale bar is 5 μm. C) Plot of single-molecule localization from both image channels after correction for the horizontal offset. The localizations correspond to the same physical position, but are still distorted due to chromatic aberrations. The scale bar is 5 μm. The inset depicts an enlargement of exemplary bead localizations from the bottom right corner of the ROI. It displays single-molecule localizations from the green channel (green circles) and red channel (magenta circles); the arrows illustrate distortions arising from chromatic aberrations. The scale bar is 0.2 μm.

1) Correction for the horizontal offset (resulted from horizontal image separation via the Optosplit II) by large-scale repositioning of one image. Usually, the localizations in the red color channel were repositioned manually using a horizontal offset parameter. The parameter was calculated from the coordinates of an exemplary localization centrally detected in both channels. Care was taken to precisely overlay the images in the large-scale offset correction procedure (compare Figure 2.10 B and C).

2) Corrections for chromatic aberrations by the application of a transformation matrix. The transformation matrix was generated using a Matlab function that fits a local weighted mean transformation to a set of predefined fixed and moving reference data points that are related by a global second degree polynomial across the entire ROI (uses the Matlab built-in function images.geotrans.LocalWeightedMeanTransformation2D.m). The reference points had to be chosen correctly from the set of all localizations. Fixed reference points were defined as localizations from the green channel. Moving reference points were defined as localizations in the red channel that physically belong to the localizations in the green

channel. A nearest neighbor distance approach was applied to define reference points in every image. In order to avoid the assignment of false partners, a maximum distance between reference points was introduced. The distance was estimated from large-scale offset corrected images. The correct assignment of reference points required a precise overlay of both images in step 1).
3) Verification of the transformation process. The transformation matrix was applied to large-scale offset corrected images. The mean distance between registered reference points (large-scale offset and aberrations corrected) was calculated to verify the transformation process.
Figure 2.11 illustrates the increase of the image registration quality before (A) and after (B) correction for chromatic aberrations. Before the transformation mask was applied an increasing distance between reference points was observed towards the corners of an image, as expected for chromatic aberrations. The remaining spatial offset between the two differently colored signals of the same object was measured to be > 100 nm in extreme cases (Figure 2.11 A). After image registration, a mean offset of 25±10 nm was measured for all reference points. The offset was homogeneous throughout the area of the ROI (Figure 2.11 B). The results of the transformation were in good agreement with the precision Semrau et al. [53] achieved for image registration. The precise registration of both color channels generally facilitates simultaneous two-color single-molecule microscopy. However, it has to be considered that imaging multifluorescent Tetraspeck beads has to be performed prior to every two-color experiment. Further, image processing is a prerequisite in order to correlate the spatial information obtained in both color channels. The presented

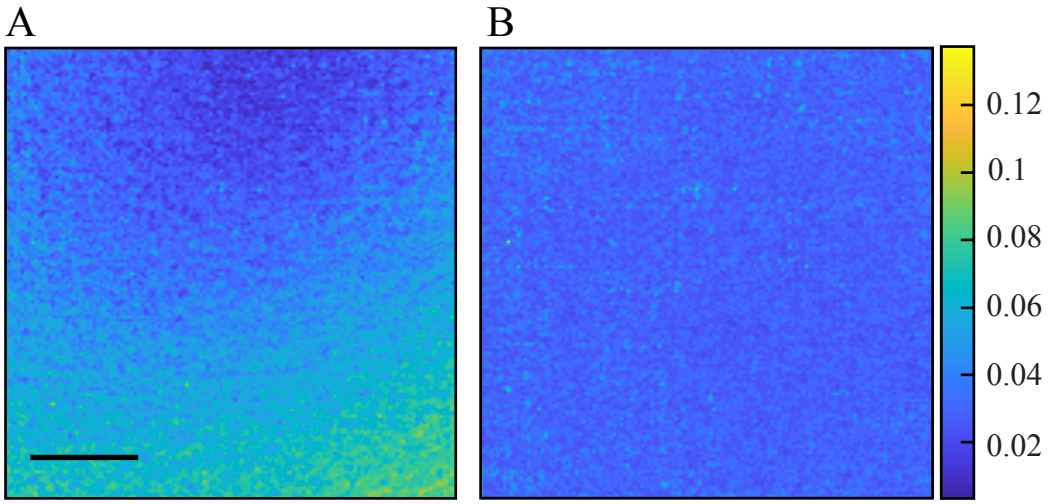

Figure 2.11: Correction for chromatic aberrations in two-color experiments. After correction for the horizontal offset (step 1), the image was further corrected for chromatic aberrations. The spatial offset of immobilized TetraSpeck beads is presented before (A) and after (B) application of the transformation matrix (step 2). The color code depicts the range of the spatial error in μm. The scale bar is 5 μm and valid for A and B.

data illustrate that the image splitter was successfully implemented into the microscope setup. The emission light of multi-fluorescent TetraSpeck beads was successfully separated and projected onto specific areas of the camera sensor chip. Image processing facilitated the precise registration of the images from both color channels, which included large-scale correction for the horizontal offset and consideration for chromatic aberrations. The high precision of the method allows prospective studies of spatially correlated processes.

2.2 Single-molecule microscopy in living trypanosomes

Single-particle tracking experiments facilitated detailed studies of VSG and lipid dynamics in a supported lipid bilayer system. For example, the diffusion of VSG M1.6 was studied as a function of the lateral protein density and the impact of VSG N-glycosylation on the mobility and diffusion coefficient was examined. Further, two distinct populations of freely diffusing VSG M1.1 were found in a SLB, consistent with recently discovered conformational states of the protein [91]. This represents a more detailed analysis of VSG dynamics than obtained by previous ensemble measurement studies using FRAP [100] but focused solely on artificial lipid bilayers. These systems are well established and commonly used to mimic the membrane environment of living cells. This facilitates studies under defined experimental conditions but also simplifies the actual complexity present in cell membranes. Hence, these methods cannot entirely replace studies in cellular systems. For that reason, single-molecule microscopy was established in living trypanosomes. The focus of the experiments was on resolving structures with high spatial resolution and studying dynamic processes like plasma membrane associated VSG mobility. In order to perform these studies, technological developments were necessary to ensure that the cells were properly immobilized on the timescale of a super-resolution experiment. The novel approach introduced here is based on hydrogel embedding.

2.2.1 Immobilization of living trypanosomes in hydrogels

Two hydrogels with different polymer compositions were tested for the immobilization of trypanosomes, autofluorescence properties, and cytocompatibility.
The first gel was based on allyl functionalized poly-glycidol (P(AGE-*co*-*G*) and thiol modified hyaluronic acid (HA-SH). The hydrogel was developed by Simone Stichler in the department of functional materials in medicine and dentistry at the university of Würzburg (AG Groll) as a part of her doctoral thesis (in preparation). The second hydrogel was based on a polyethylene scaffold, consisted of 8-arm poly (ethylene glycol, 20 kDa)-norbornene (PEG-NB) and linear PEG-dithiol (PEG-dT, 1 kDa), and was chosen as a commercially available alternative for the first gel.

Quantification of the hydrogel immobilization efficiency

The flagellar beat is the origin of trypanosome motility. In order to quantify the immobilization efficiency of the hydrogels, fluorescence imaging was performed on the trypanosome flagellum. Imaging this structure with high resolution over a period of time after immobilization should allow to draw conclusions about residual movements of the cell as a whole. A cell line was used for the experiments that expresses kinesin-MORN::eYFP. The cell line

was generated by Ines Subota and provided for the experiments. She found that the fusion protein is located at the flagellar region, elongating from the basal body next to the kinetoplast until the flagella tip (see Figure 2 in [111] for an exemplary fluorescence image of the flagellum). Similar results were found for trypanosomes immobilized in hydrogels, as illustrated in Figure 2.12, (a). The signal distribution of kinesin-MORN::eYFP is in accordance with the localization of the trypanosomal axoneme. Hence, kinesin-MORN::eYFP was regarded as a representative for the axoneme. In order to resolve this structure precisely, super-resolution imaging was performed by exploiting the intrinsic blinking behavior of eYFP molecules as described in the literature [112, 65].
In this section, the label density at the flagellar region was quantified and compared to the autofluorescence properties of the hydrogels in the spectral range of the fluorophore. The mean axoneme diameter of immobilized trypanosomes was then determined from super-resolution images and the results from chemically fixed and living trypanosomes were compared to quantify the immobilization efficiency of the hydrogels. As this section encompasses results from two different hydrogel systems with each varying polymer concentrations, the approach and its applicability are first demonstrated on the example of an embedded trypanosome. The final results are presented for both hydrogels.
As a proof of concept, a kinesin-MORN::eYFP expressing trypanosome was immobilized in a 15% (w/v) HA-SH/P(AGE-*co*-G) hydrogel. Figure 2.12 depicts exemplary single-molecule fluorescence snapshots of blinking eYFP molecules and a reconstituted super-resolution image of the axonemal structure from the trypanosome. As the label density of eYFP molecules at the flagellar region was initially high, prebleaching was performed before single-fluorophore spots became visible (Figure 2.12, a). For the trypanosome presented, eYFP molecules were localized inside the hydrogel with a precision of 24$\pm$5 nm. The fluorophore label density at the flagellar region was determined from single-molecule localizations. According to the Nyquist-Shannon theorem [40], this parameter defines the minimal extractable information of a structure. It had to be considered that next to specific fluorophore signals at the flagellar region, also additional global noise and false-positive signals occurred in the images. The spatial distribution of these signals suggested hydrogel contaminations and cellular autofluorescence or intracellular kinesin-MORN::eYFP (Figure 2.12, f). Thus, flagellar signals were sectioned from these unspecific background signals as described in Section 4.2.9. The process facilitated the identification of eYFP molecules that were localized at the flagellum. For the example trypanosome presented, 7309 eYFP molecules were localized at the flagellar region. Considering the longitudinal extension of the flagellum, a mean label density, p, of 988 eYFP molecules per μm^2 was achieved. Comparison with the average density of the background localizations revealed, that the contribution of unspecific signal, r, was $< 3\%$ for the specific case. In order to quantify the width of the eYFP signals in the super-resolution image, a contour line along the flagellar region was set. The average profile at lines perpendicular to the

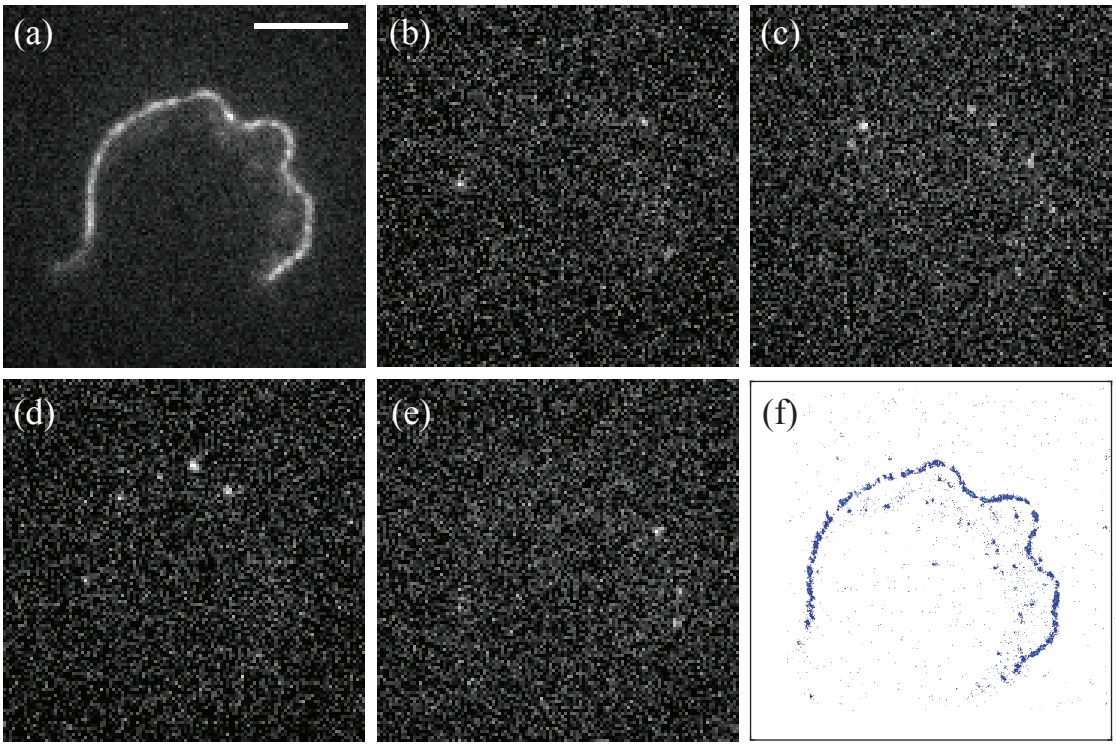

Figure 2.12: Super-resolution imaging of a kinesin-MORN::eYFP expressing trypanosome immobilized in a 15% (w/v) HA-SH/P(AGE-*co*-G) hydrogel. a) Diffraction limited fluorescence image of kinesin-MORN::eYFP, which is located to the axoneme. b-e) Consecutive background subtracted fluorescence snapshots of blinking eYFP molecules. f) Reconstructed super-resolution image of the axoneme located kinesin-MORN::eYFP. The scale bar is 5 μm and valid for a-f).

contour line was calculated to determine the average full-width half maximum (FWHM) of the signal. The FWHM was representative for the mean axonemal diameter of the embedded trypanosome and was found to be 200$\pm$35 nm.

The presented data from an immobilized trypanosome illustrate, that the applied hydrogel exhibits low autofluorescence properties in the spectral range of the fluorophore. eYFP molecules inside the hydrogel could be localized with high precision and the high label density at the flagellar region allowed the precise determination of the mean axonemal diameter from the super-resolution image. These features should generally meet the requirements of super-resolution imaging to quantify the immobilization efficiency of the hydrogels.

In a next step, the immobilization efficiencies of HA-SH/P(AGE-*co*-G) hydrogels were quantified. For that purpose, kinesin-MORN::eYFP expressing trypanosomes were embedded in HA-SH/P(AGE-*co*-G) hydrogels of varying polymer concentration and imaged as described before (Section 4.2.9). As a control for the immobilization efficiency, the average axonemal diameter of chemically fixed trypanosomes was determined. A comparison of the average axonemal diameter from living and chemically fixed trypanosomes allowed

to draw conclusion about the immobilization efficiency. Any residual flagellar beat of insufficiently immobilized cells should result in a spread out distribution of the eYFP signals and thereby increase the average axonemal diameter.
Figure 2.13 depicts exemplary super-resolution images of chemically fixed (a) or living (b-d) trypanosomes in 15%, 10%, 15% and 20% (w/v) HA-SH/P(AGE-*co*-G) hydrogels, respectively. Following the procedure previously described for the example trypanosome,

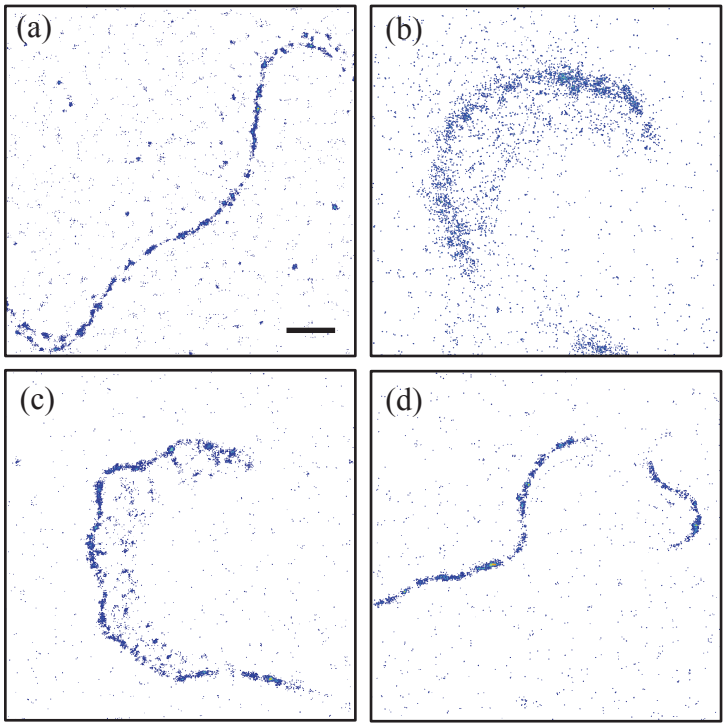

Figure 2.13: Exemplary super-resolution images of the axoneme structure of immobilized cells. The cells were chemically fixed prior to immobilization (a, 15% (w/v)) or immobilized alive in hydrogels of 10% (b), 15% (c) and 20% (d) (w/v) polymer concentrations. The spread-out signal distribution of the axoneme in b) is due to insufficient immobilization. The scale bar is 2 μm and valid for (a-d).

the autofluorescence properties of HA-SH/P(AGE-*co*-G) hydrogels and label densities at the flagellar regions of embedded trypanosomes were determined. In total, 127 trypanosomes were imaged in hydrogels of varying polymer concentration. eYFP molecules were localized with a precision of 24$\pm$6 nm. The determination of flagellar specific signals and background fluorescence revealed that even in the most unfavorable case the unspecific background contribution, r, did not exceed more than 3% of the total flagellar signal (Figure 2.14, a). The mode of the distribution of r was found to be 0.5%. The average label density inside the flagellum of the immobilized trypanosomes, p, was measured to range from 200 molecules μm^{-2} up to 1500 molecules μm^{-2}, with an average of 750 molecules μm^{-2}. To ensure high sampling frequencies, only images with an average density of > 500 molecules μm^{-2} were further analyzed.

First, the average axonemal diameter of 23 chemically fixed trypanosomes was determined.

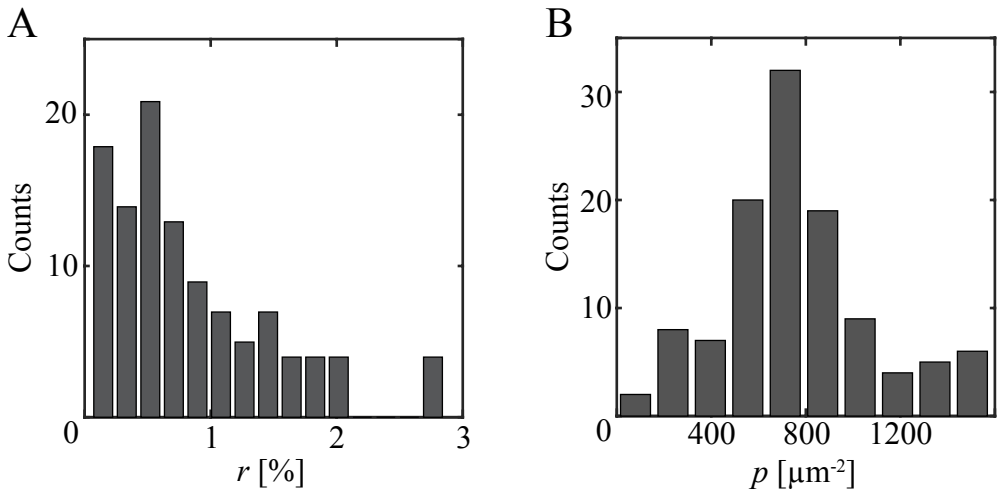

Figure 2.14: Optical properties of kinesin-MORN::eYFP expressing cells immobilized in HA-SH/P(AGE-*co*-G) hydrogels. (a) Histogram of the percentage of unspecific signals, *r*, that contributes to flagella kinesin-MORN::eYFP signals. (b) Histogram of the kinesin-MORN::eYFP density, *p*, in the flagella region.

Super-resolution images revealed that the average axonemal diameter was 214±39 nm (Figure 2.15, a). This value was in good agreement with axonemal diameters that were extracted from previously published electron microscopy images (210-230 nm, [113, 114]) and images acquired by Elisabeth Meyer-Natus in the institute (data not shown).
Next, the analysis was repeated for living trypanosomes embedded in HA-SH/P(AGE-*co*-G) hydrogels of different polymer concentrations. In total, 25 cells were immobilized in 10% (w/v) HA-SH/P(AGE-*co*-G) hydrogels followed by the reconstruction of super-resolution images. It has to be mentioned, that the behavior of the embedded cells at 10% (w/v) polymer concentration was quite diverse. A large fraction of the imaged flagella (13 from 25) were still moving substantially while the trypanosomes as a whole were stationary. As a consequence, a spread-out distribution of eYFP signals was seen from the super-resolution images of these cells (see Figure 2.13, b). The calculated label density at the flagellar region was low and impeded quantitative measurements. However, the average axonemal diameter in the 10% case was calculated to be 307±151 nm for the remaining cells (Figure 2.13, B, magenta line) and hence, substantially larger than the average cross section of chemically fixed trypanosomes. The average axonemal diameter can thus be regarded as a lower estimate for the lateral and axial space that is still accessible to the flagellum. The average diameters determined for trypanosomes immobilized in 15% (w/v) and 20% (w/v) hydrogels were measured to be 203±36 nm (N_{cells} = 42) and 191±32 nm (N_{cells} = 35), respectively (Figure 2.13, B, green and blue line). These values were in good agreement with the previously determined average axonemal diameter of chemically fixed trypanosomes and electron microscopy images. The analysis of an unpaired Student t-test

showed, that the distribution of these diameters were not significantly different at a 1% significance level. The presented data illustrate that HA-SH/P(AGE-*co*-G) hydrogels of

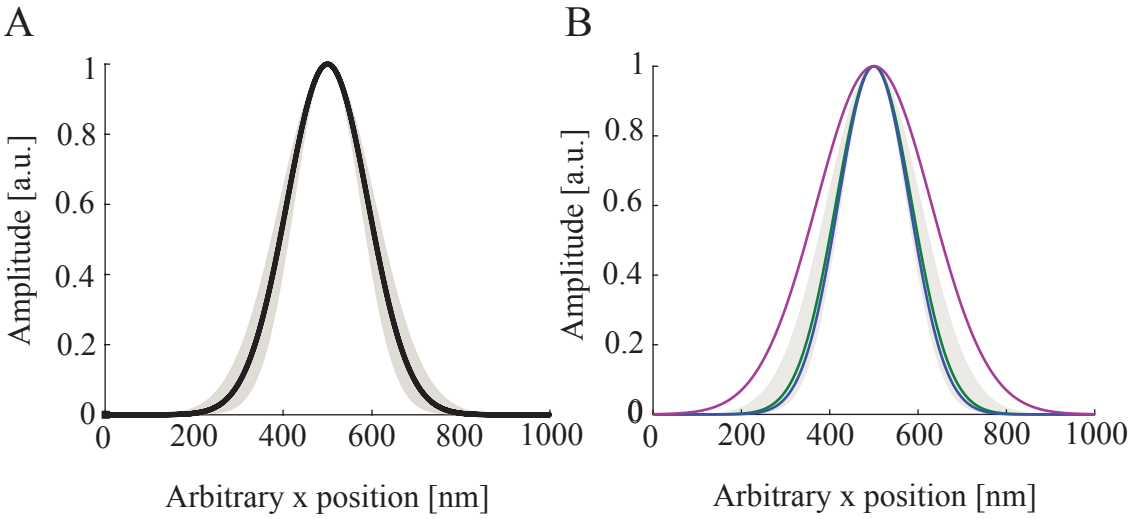

Figure 2.15: Quantification of the immobilization efficiency in HA-SH/P(AGE-*co*-G) hydrogels. The average axoneme cross sections were derived from fitting a Gaussian profile perpendicular to the kinesin-MORN::eYFP signal profiles of chemically fixed cells (A) or living cells, immobilized in 10% (magenta line), 15% (green line) and 20% (blue line) (w/v) hydrogels (B). The full lines depict the mean axonemal cross section. The shaded region represents the standard deviation from measurements of chemically fixed cells and was also plotted in (B) for better comparison.

15% (w/v) polymer concentration and above efficiently immobilized trypanosomes. Hence, hydrogel concentrations of 15% (w/v) were further used for single-molecule experiments in living trypanosomes. In order to correlate the employed polymer concentration to the resulting stiffness of the hydrogel, mechanical testing of 15% (w/v) hydrogels were performed by Simone Stichler. She measured a Young's modulus of 154±22 kPa for three replicates of the polymerized hydrogels. Thus, it was hypothesized that a gel stiffness of at least 150 kPa is a prerequisite for the efficient immobilization of living trypanosomes on the nanometer level.

Immobilization experiments were further performed for trypanosomes embedded in hydrogels based on a polyethylene scaffold. The gel consisted of 8-arm poly (ethylene glycol, 20 kDa)-norbornene (PEG-NB) and linear PEG-dithiol (PEG-dT, 1 kDa) and was chosen as a commercially available alternative for the first gel. The trypanosomes were immobilized in 10% (w/v) hydrogels containing equimolar ratios of functional groups. Figure 2.16 (A) depicts an exemplary super-resolution image of an embedded trypanosome. In total, super-resolution images of 34 immobilized cells were reconstructed (see Figure 6.2 for a comparison of a diffraction limited and a super-resolved image). A mean localization precision of 23±5 nm was achieved for eYFP molecules inside the hydrogel. Following the

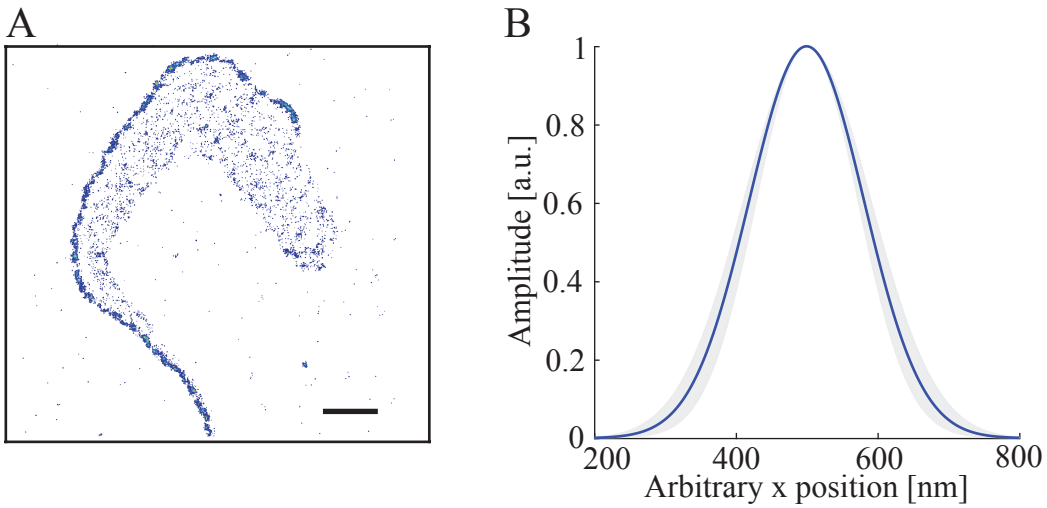

Figure 2.16: Super-resolution image of a trypanosomes in a PEG-NB/PEG-dT hydrogel and quantification of the immobilization efficiency. A) Representative super-resolution image of a kinesin-MORN::eYFP expressing trypanosomes in a 10% (w/v) hydrogel. The scale bar is 2 μm. B) Mean axoneme cross section of immobilized trypanosomes derived from fitting a Gaussian profile perpendicular to the kinesin-MORN::eYFP signal profiles. Presented are the mean values (blue line) and standard deviation (shaded region).

procedure previously described for HA-SH/P(AGE-*co*-G) hydrogels, the autofluorescence properties of the PEG-NB/PEG-dT hydrogel and label densities at the flagellar regions of embedded trypanosomes were determined. The contribution of false-positive signals was generally low and did not exceed $\sim$ 1% of the total flagellar signal. Further, a high label density at the flagellar region was measured, ranging from 450 molecules μm^{-2} up to 1300 molecules μm^{-2}, with an average of 800 molecules μm^{-2}. The average diameter of the axoneme was measured to be 191$\pm$23 nm (Figure 2.16, B). This value was in good agreement with the average diameters determined for chemically fixed cells, electron microscopy images, and trypanosomes immobilized in 15-20% HA-SH/P(AGE-*co*-G) hydrogels.

The presented data illustrate that HA-SH/P(AGE-*co*-G) hydrogels and PEG-NB/PEG-dT hydrogels are both suitable to perform super-resolution imaging in living trypanosomes. The hydrogels exhibit low autofluorescence properties in the spectral range of the fluorescence label. Further, the stiffness of the hydrogels facilitated an efficient cell immobilization on the nanometer level. This enabled super-resolution imaging of a structure inside a living trypanosome for the first time.

Cell viability in cross-linked hydrogels

The immobilization of *T. brucei* cells in HA-SH/P(AGE-*co*-G) or PEG-NB/PEG-dT hydrogels facilitated super-resolution imaging of the axonemal structure (Section 2.2.1). In order to ensure the cytocompatibility of these cross-linked hydrogels the viability of embedded trypanosomes was monitored.

In preliminary experiments, trypanosomes were immobilized in HA-SH/P(AGE-*co*-G) hydrogels of varying polymer concentration. The gels were swollen in a buffer solution (TDB) directly after cross-linking or 30 min after immobilization. Hydrogel swelling decreased the stiffness of the hydrogels significantly and residual flagellar bead became visible (data not shown). These experiments suggested a high cytocompatibility of HA-SH/P(AGE-*co*-G) hydrogels. In order to monitor the viability of immobilized trypanosomes quantitatively, propidium iodide (PI) was used as a fluorescent life/dead marker. PI is a membrane-impermeant green dye that is excluded from the interior of viable cells but can bind to DNA upon loss of cell membrane integrity. This leads to a large Stokes shift of the PI emission and the dye becomes highly fluorescent with an excitation and emission maximum of 535 nm and 617 nm, respectively.

The viability of immobilized trypanosomes was monitored up to 60 min at RT (PEG-NB/PEG-dT hydrogels) or 37 °C (HA-SH/P(AGE-*co*-G) hydrogels). The evaluation of

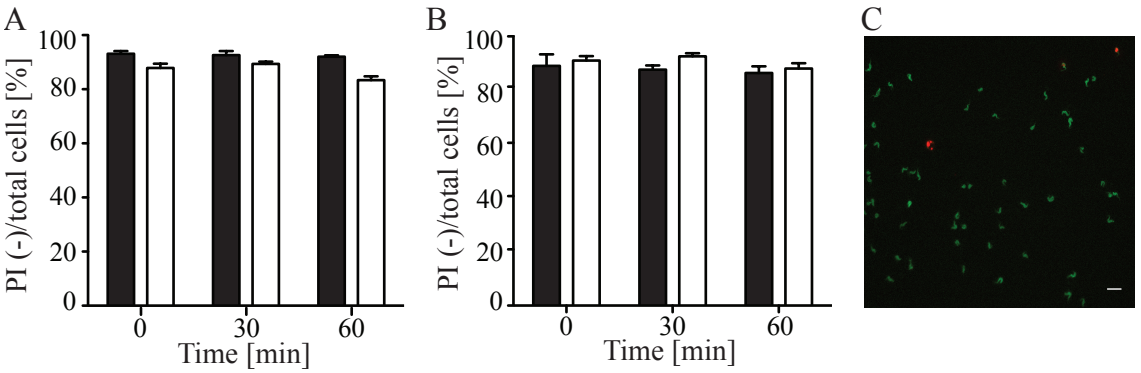

Figure 2.17: Viability of immobilized trypanosomes. The cells were embedded in 15% (w/v) HA-SH/P(AGE-*co*-G) hydrogels (A) or 10% (w/v) (PEG-NB/PEG-dT hydrogels (B)). Black bars show trypanosome survival rates (PI negative (-)) after cross-linking. As a control, the viability of the cells was monitored in buffer solution (TDB, white bars). The numbers represent the mean and standard deviation of 3 replicate experiments. C) Overlay fluorescence images of VSG surface stained trypanosomes (green) and intracellular PI fluorescence (red). The scale bar is 20 μm.

PI-negative and PI-positive cells (N_{cells} > 100 for each time point in both hydrogels) revealed high cell viabilities of >80% up to 60 min after embedding (Figure 2.17 A, B). These values were in good agreement with the fraction of living cells in TDB ($\sim$ 90%). TDB is a buffer solution that is commonly used in trypanosome research and contains 20 mM glucose, which facilitates a high viability of trypanosomes for several hours. VSG coat

staining of living trypanosomes previous to the immobilization facilitated the counting of immobilized cells in fluorescence images (Figure 2.17, C). It has to be mentioned that the cell viability strongly decreased after 60 min in both types of hydrogels. Further, cells that were immobilized in PEG-NB/PEG-dT hydrogels and incubated at 37 °C already exhibited a reduced viability at earlier time points (30-40 min). However, the large fraction of viable cells in HA-SH/P(AGE-*co*-G) hydrogels at 37 °C or PEG-NB/PEG-dT hydrogels at RT up to 60 min after immobilization provided sufficient time to perform single-molecule microscopy in living trypanosomes.

A third type of hydrogel (PEG-VS/HA-SH) was used for the immobilization of living trypanosome. The cytocompatibility of the PEG-VS/HA-SH hydrogel is presented in Section 2.2.3.

2.2.2 Plasma membrane organization in living trypanosomes

The eukaryotic plasma membrane consists of two distinct leaflets. Each exhibits specific lipid compositions and associated membrane proteins. There is limited knowledge of the specific lipid composition or the distribution of membrane associated proteins in *T. brucei*. Studies that addressed the membrane organization in trypanosomes so far focused on the dynamics of VSGs or fluorescent lipid tracer molecules [100, 105, 118]. On the time and length scales of the applied measurement method (FRAP), no indications of membrane or protein structuring was observed.

The establishment of SMFM in living trypanosomes in this work facilitates the investigation of membrane associated structures and dynamics with high temporal and spatial resolution. This section focuses on SMFM to study the organization of the inner plasma membrane leaflet. Super-resolution imaging was performed in living trypanosomes that expressed HASP::eYFP. HASP::eYFP is a fusion protein that is post-transcriptionally palmitoylated and myristoylated and localizes to the cytosolic side of the plasma membrane (see Figure 3 in [115] for exemplary immunofluorescence images of HASP::eYFP). The short HASP-sequence encompassed only 18 amino acids and thus, the fusion protein was regarded as a membrane anchored eYFP. The strong hydrophobicity of the dual fatty acyl anchor was found to stably attach proteins to a membrane [116]. The construct was used as a fluorescent marker to monitor the organization of the inner plasma membrane leaflet.

In a preliminary experiment, HASP::eYFP dynamics were studied in gelatin embedded trypanosomes via FRAP. The experiments revealed a diffusion coefficient of $\sim 0.1\ \mu m^2\ s^{-1}$ and a mobile fraction of 70-80% (Figure 6.3). The mobile fraction of HASP::eYFP was found to be in the same range as for surface VSGs, but the diffusion coefficient was $\sim$2-3 times higher. The strong expression of HASP::eYFP in the transgenic cell line impeded quantitative measurements via SMFM. Hence, the construct was cloned into the plasmid pLEW100v5, which allows a tetracycline ineducable level of protein expression [117] (Section 4.2.2). To this end, the plasmid containing the sequence of the construct was integrated into the genome of a parental *T. brucei* cell line (Section 4.2.1). Three clonal populations were obtained, of which one showed stable growth (see Figure 6.4) and membrane associated eYFP signals. Trypanosomes from this monoclonal population were used to perform microscopic studies. In a preliminary experiment, the dynamics of HASP::eYFP were studied via SPT. The fast movement of the fusion protein out of the focal plane and blinking behavior of eYFP at high illumination intensities resulted in trajectories of short length (< 10 localizations per trajectory), which impeded quantitative measurements of HASP::eYFP dynamics via SPT. However, the mobility of HASP::eYFP was exploited to cover large fractions of the plasma membrane and investigate a potential plasma membrane organization. To this end, 17 cells were immobilized in 10% (w/v)

PEG-NB/PEG-dT hydrogels and super-resolution imaging was performed as described before (Section 4.2.9). In total, 266363 eYFP molecules were localized with a precision of 23±5 nm. Reconstructed super-resolution images suggested, that areas of preferred eYFP occurrence exist in the plasma membrane (Figure 2.18, A; inset: red asterisk). An analysis

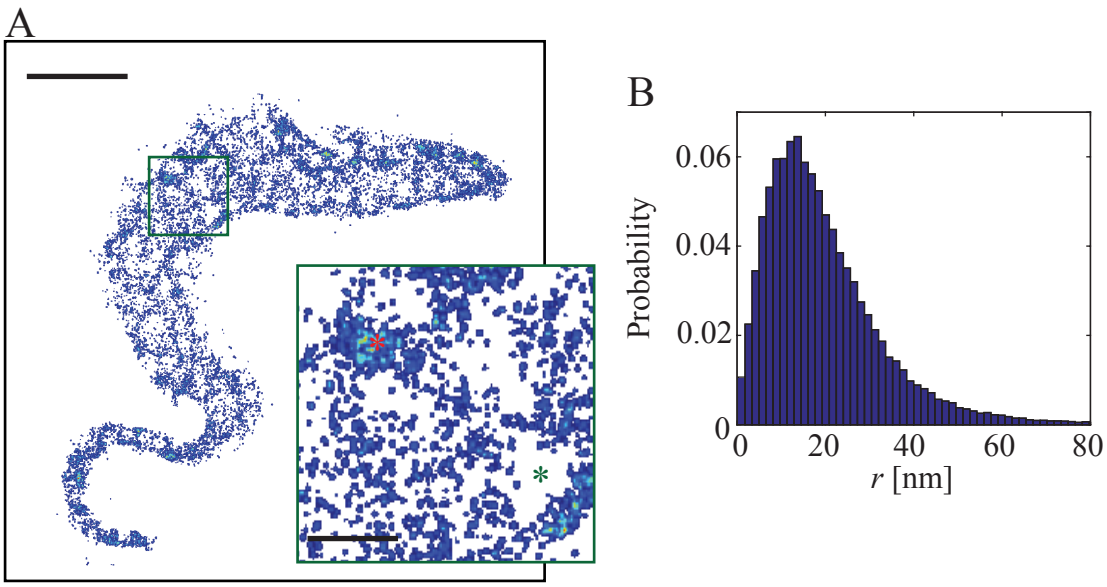

Figure 2.18: Distribution of HASP::eYFP in the plasma membrane. A) Reconstructed super-resolution image of HASP::eYFP in the inner leaflet of the plasma membrane of *T. brucei*. The scale bar is 2 μm. Inset: zoom into the area inside the green rectangle. The red asterisk illustrates a domains of preferred eYFP appearance, the green asterisk depicts a diluted membrane area. The scale bar is 0.5 μm. B) Probability distribution of the distances between HASP::eYFP molecules in the inner leaflet. The values were obtained from a nearest neighbor analysis. The figure is adapted from [115].

of the nearest neighbor distances (NND) was performed for HASP::eYFP localizations. The analysis confirmed this assumption (Figure 2.18, B). The most frequent distance between neighboring eYFP molecules was found to be 14 nm. A theoretical calculation, that assumes a homogeneous distribution of all localized eYFP molecules in the surface area of a trypanosome ($\sim$ 100 μm^2, [20]) would result in a mean distance of 65 nm. This discrepancy leads to the assumption that local clustering appeared for membrane associated HASP::eYFP molecules. In order to quantify these potential distribution patterns, a Ripley's analysis was performed for the data set. The $L(r) - r$ function yielded a maximum at domain radii of 170±5 nm, suggesting the existence of eYFP domains with a radius of this size in the membrane (Figure 2.19 A). The width of the 1σ confidence interval and the associated range of cluster radii (140-205 nm) was broad. This was not unexpected, as domains that deviate from a circular shape were commonly found for HASP::eYFP in the plasma membrane. A Ripley's analysis, however, inherently assumes circular shapes of potential domains.

A close inspection of the reconstructed super-resolution images revealed that next to

clustered areas, there were also specific regions where eYFP molecules appeared diluted (Figure 2.18, A; inset: green asterisk). In a next step, these regions were identified, ex-

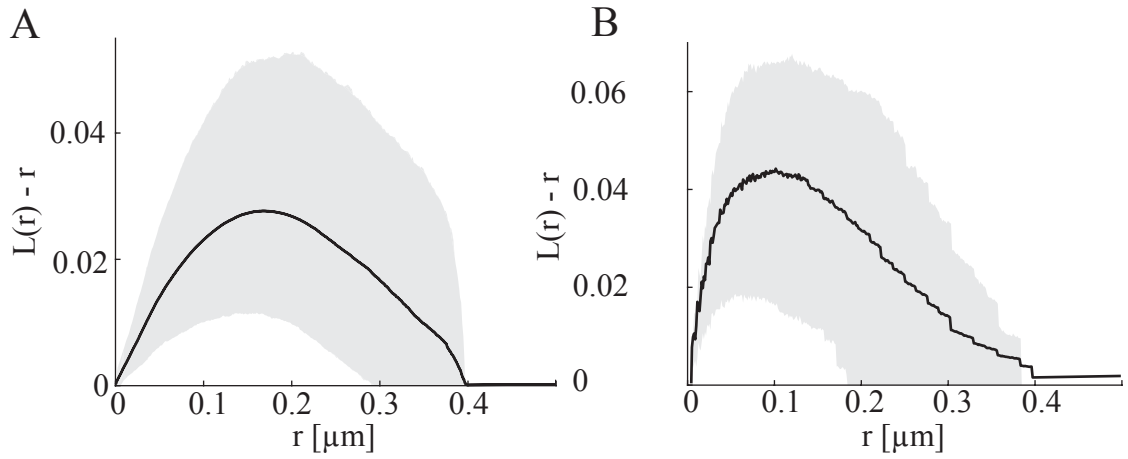

Figure 2.19: Cluster analysis of the HASP::eYFP distribution in the plasma membrane. A Ripley's $L(r) - r$ analysis for HASP::eYFP occupied (A) or void (B) membrane areas together with the 1 σ confidence interval (gray areas). The function was averaged over 17 imaged cells (black lines) and exhibited a maximum of 170±5 nm (A) and 115±15 nm (B). The figure is adapted from [115].

tracted from the original data set and artificially populated with eYFP localizations (see Section 4.2.9). A Ripley's analysis was performed for these areas to identify the mean radius of the diluted areas. The $L(r) - r$ function yielded a maximum at domain radii of 115±15 nm (Figure 2.19 B).

The presented data illustrate, that super-resolution imaging was successfully performed on trypanosomes expressing HASP::eYFP. In combination with a statistical analysis of nonrandom spatial distributions patterns it was found that HASP::eYFPs are not homogeneously distributed in the inner leaflet of the plasma membrane. Specific membrane domains were identified, in which the protein appeared accumulated or diluted.

2.2.3 Tracking of VSGs on the surface of living trypanosomes

Experimental investigations of VSG coat dynamics in living trypanosomes were previously performed on the ensemble level using the method of FRAP [105, 100]. These studies revealed diffusion coefficients of 0.010 - 0.020 $\mu m^2\ s^{-1}$ for different cell lines. Now, that single-molecule microscopy became accessible in living trypanosomes, SPT of surface VSG was performed in this work. To this end, a cell line that expressed VSG M1.6 was immobilized in a hydrogel and imaged.

Immobilization of *T. brucei* cells for single-particle tracking

Preliminary single-particle tracking experiments were performed in HA-SH/P(AGE-*co*-G) or PEG-NB/PEG-dT hydrogel immobilized trypanosomes. The immobilization method, however, often resulted in a cell orientation, that was unfavorable for imaging the whole plasma membrane. This was due to the fact that the cells moved during the UV-mediated cross-linking process. In order to immobilize trypanosomes in a more favorable position, a third type of hydrogel was tested for the immobilization of *T. brucei* cells. The gel consisted of HA-SH and 8-arm PEG-Vinylsulfone (10 kDa). Thiol and vinylsulfone groups readily reacted upon mixing and formed cross-linked hydrogels without the addition of a photoinitiator and UV-illumination. The reaction kinetics of the process depended critically on the pH-value of the buffer solution and gel formation was fast under slightly alkaline conditions. For SMFM, trypanosomes were embedded in 10% (w/v) PEG-VS/HA-SH hydrogels (pH 8.3). The cells were found to be efficiently immobilized within one minute. This provided sufficient time to centrifuge the trypanosomes during the polymerization process and thereby immobilize the cells in close proximity to the lower glass support. Centrifugation facilitated a flat cell orientation of immobilized trypanosomes and allowed imaging the whole plasma membrane.
The viability of trypanosomes embedded in PEG-VS/HA-SH hydrogels was monitored as described previously (Section 2.2.1) and was found to be high ($\sim$90%) for 1 h at 37 °C (Figure 2.20). This provided sufficient time to perform single-molecule microscopy in living trypanosomes. The contribution of signals that resulted from hydrogel autofluorescence or contaminations were found to be low in the spectral range of ATTO647N (usually < 0.1 false-positive signals per frame after image processing). Hence, PEG-VS/HA-SH hydrogels were considered to be suitable for single-molecule microscopy. The quantification of the immobilization efficiency will be performed by Marie Schwebs as a part of her doctoral thesis and is work in progress.

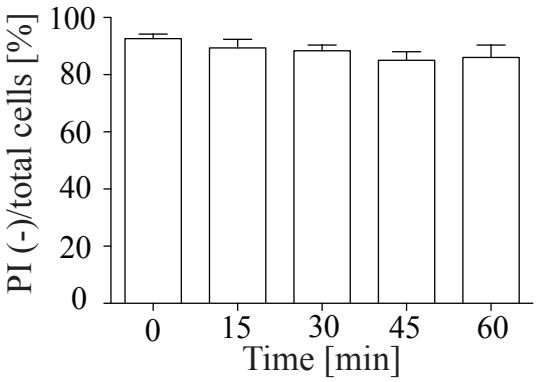

Figure 2.20: Viability of trypanosomes immobilized in PEG-VS/HA-SH hydrogels. The cells were embedded in 10% (w/v) hydrogels. White bars illustrate survival rates (PI negative (-)) of embedded trypanosomes up to 60 min after immobilization. For each time point > 100 trypanosomes were counted. The numbers represent the mean and standard deviation of 3 replicate experiments.

Single-particle tracking of *T. brucei* surface VSGs

Hydrogel embedding provided a beneficial orientation of immobilized trypanosomes for studying the whole plasma membrane. However, the cell architecture of the parasite was found to complicate SPT of surface VSGs. BSF trypanosomes are as large as 20 μm, but their cell body diameter is around 2-4 μm at the flagellar pocket and as small as < 1 μm at the anterior end (see Section 1.2.2). Due to the strong bending of the plasma membrane, surface VSGs moved quickly axial out of the detectable focal plane. Using imaging frequencies commonly applied in model membranes in this work (28 or 42 Hz) resulted in short VSG trajectories (< 10 localizations per trace). The limited length of the trajectories impeded quantitative studies of VSG dynamics via an MSD analysis to a great extend. Hence, tracking of VSGs required fast acquisition cycle times in order to generate VSG trajectories that included multiple single-molecule localizations. The built-in cropped mode and frame transfer settings of the EMCCD camera allowed image interval times of 4.9 ms between consecutive images within a ROI of 15.2 x 15.2 μm. Furthermore, it had to be considered that bleaching of ATTO647N during the imaging process strongly limited the number of VSG trajectories. In previous experiments, live cell staining was performed in buffer solution (TDB) and excess ATTO647N was removed from the background by multiple centrifugation and washing steps before the trypanosomes were immobilized and imaged. In this case, the number of localizations was found to be strongly limited due to photobleaching and resulted in small numbers of trajectories. In order to generate a multitude of VSG trajectories on the cell surface of immobilized trypanosomes, reactive ATTO647N dyes were allowed to diffuse through the hydrogel background during the imaging process. Adjusting the pH-value of the hydrogel to 8.3 facilitated the constant binding of dyes to surface VSGs. As a consequence, the

number of VSG M1.6-ATTO647N localizations was significantly improved in immobilized trypanosomes. The adaptations facilitated the generation of a large number of VSG trajectories. In total, 16 trypanosomes were immobilized in 10% (w/v) PEG-VS/HASH

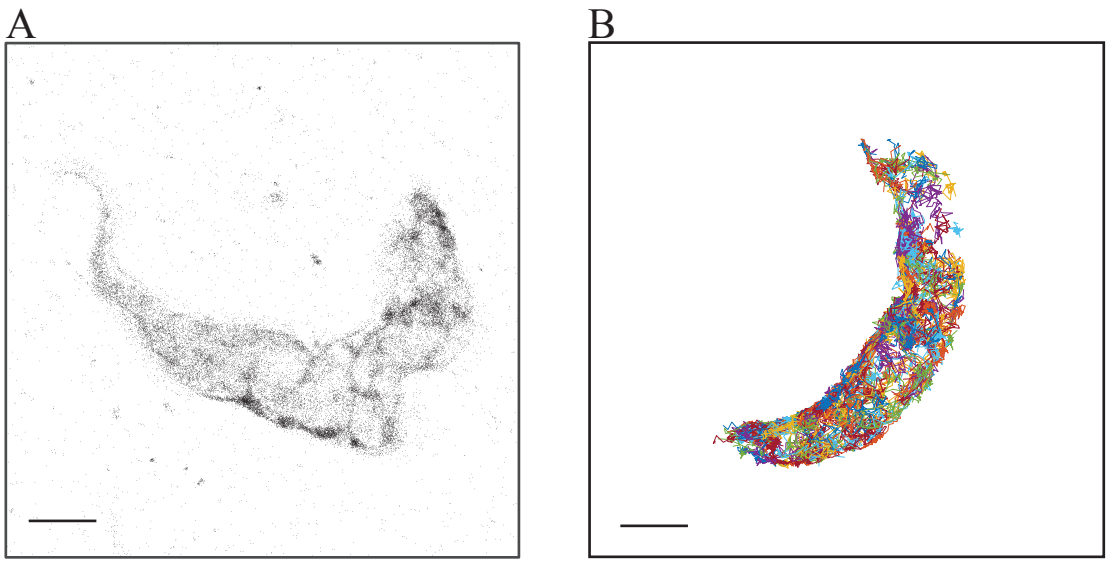

Figure 2.21: Single-particle tracking of surface VSG on living trypanosomes. A) Exemplary single-molecule localizations of a trypanosome immobilized in a 10% (w/v)) PEG-VS/HA-SH hydrogel. B) VSG trajectories in living trypanosomes. False-positive trajectories from the background were removed by masking the cell region. Individual trajectories are presented in different colors. The scale bar is 2 μm and valid for A) and B).

hydrogels and imaged as described in Section 4.2.8. Due to the continuous binding of reactive ATTO647N ester from the hydrogel background, $3.55*10^5$ molecules were localized in all samples. The localization precision was determined to be 32 ± 15 nm. Figure 2.21 (A) depicts an exemplary image of an immobilized trypanosome that contains all single-molecule localizations from an imaging procedure. Most signals were found to be located to the trypanosome. This was most likely because the diffusion of the reactive dye in the hydrogel was fast and ATTO647N rapidly accumulated at the trypanosome. Single-particle trajectories were generated from the localizations as described before (Section 2.1.1). In total, 2870 trajectories were generated. A weighted mean trace length of 28 localizations was calculated for these trajectories (Figure 2.21). Following the procedure previously described (Section 4.2.9), trajectories were categorized as mobile or immobile. A mobile fraction of 98% was determined and immobile trajectories were removed before further analysis. The mobile fraction determined in SPT was substantially higher than the one found in FRAP experiments ($\sim$ 80%, see Figure 6.3 or [118]). For the remaining mobile particles a preliminary MSD analysis was performed by averaging over all trajectories. The analysis revealed a diffusion coefficient of 0.11 ± 0.08 μm^2 s^{-1}. This represents a significantly higher diffusion coefficient than previously determined in FRAP measurements (see Figure 6.3 and [100, 105]). From the MSD analysis, no deviation from

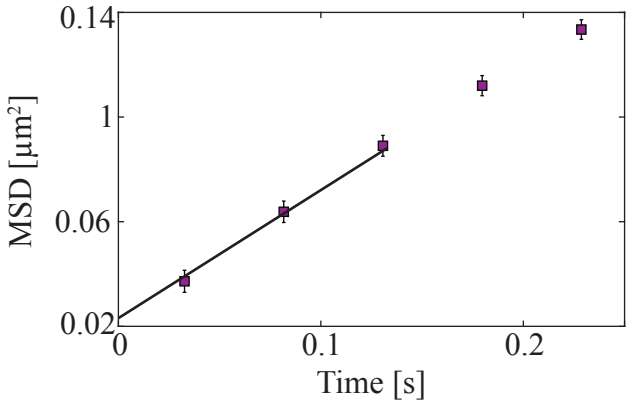

Figure 2.22: MSD analysis of surface VSG trajectories. The MSDs of all VSG trajectories from 23 surface labeled, immobilized trypanosomes were averaged. The diffusion coefficient was calculated from a linear to the first three data points. Five data points are presented to illustrate the absence of non-Brownian VSG motion in the data set.

Brownian motion was observed as the data points were found to increase linearly with time.

The results illustrate that SPT was successfully performed in living trypanosomes. The experiments represent the first measurements of VSG dynamics on the cell surface of living trypanosomes on the single-molecule level.

3. Discussion

Within the last years, trypanosomes became a well established model organisms in the field of biology. Modern molecular biology methods are nowadays routinely applied in trypanosome research. At the same time, sophisticated fluorescence microscopy methods were developed that facilitate studying properties of molecules in living cells with high spatial and temporal resolution. This includes single-molecule and super-resolution fluorescence microscopy. Applying these methods in living trypanosomes, however, is limited to a great extend by the intrinsic motility of the parasites.
In this work, state-of-the-art SMFM and SRM were introduced as a tool for live-cell imaging in trypanosomes. This included first the quantification of single fluorescent molecules. SLBs were then used as a model system to investigate the biophysical properties of VSGs on the single-molecule level. The studies were complemented by SMFM in living trypanosomes. For that purpose, hydrogel embedding was introduced as a tool for the immobilization of the parasite. The hydrogels were quantified with respect to autofluorescence properties, immobilization efficiency and cytocompatibility. As a proof of concept, static and dynamic processes were studied in living trypanosomes. This included investigations of the plasma membrane organization as well as VSG dynamics on the cell surface. In this section, the results of this work are discussed and critically reviewed.

3.1 Single-particle tracking in SLBs

3.1.1 Detection and quantification of single fluorescent molecules

Single-molecule fluorescence microscopy has become a well established method to study diverse phenomena in the field of biology. In order to make this tool accessible for trypanosome research, a fluorescence microscope setup was installed and tested for the detection and quantification of single fluorescent molecules. To this end, fluorescent lipids (DOPE488) and fluorescently labeled VSGs (VSG M1.6 ATTO647N) were integrated into preformed SOPC lipid bilayers at low lateral densities and individual molecules were monitored at the microscope (see Figure 2.1).
The lipids were headgroup labeled with an ATTO488 dye. ATTO488 exhibits high fluorescence quantum yields (80%) and was shown to be suitable for localization-based super-resolution imaging [119]. VSGs were fluorescently labeled using N-hydroxysuccinimide ester coupled ATTO647N dyes (ATTO-TEC). Characteristic features of ATTO647N are strong absorption, high fluorescence quantum yields (65%) and a high photo-chemical stability. Thus, it is recommended especially for single-molecule detection applications (e.g. [120]).
In order to facilitate a homogeneous illumination of the fluorophores, the laser spot size was adjusted to be significantly larger than the size of the ROI. This was achieved by adjusting the light-fiber cable output collimation lens. Typically, a Gaussian laser profile

with a FWHM of 32 μm was set at the focal plane before imaging a centered ROI of 19 μm, 15 μm or 10 μm. As a result, an inhomogeneous illumination of the ROI was minimized. The deviation of the laser power from the edges to the center of a ROI was calculated from the Gaussian-profile of the laser spot and found to be low ($\sim$ 20, 14 and 6%, respectively).

After the addition of DOPE488 or VSG M1.6 ATTO647N to preformed SLBs, diffraction limited signals were detected in the membrane (Figure 2.1). These signals were not detected in pure SOPC bilayers. Further, they were resistant to washing of the SLBs, suggesting a stable integration of the molecules. This is expected for a lipid in a membrane, but implies the existence of a GPI-anchor at VSG M1.6 after the extraction and purification of the protein (Section 4.2.6). Proteolytically cleaved VSGs did not show a stable integration into SLBs and could be removed during the washing procedure (data not shown). The fluorescence snapshots further show that VSG M1.6 ATTO647N and DOPE488 moved in the SLBs during the imaging process (Figure 2.1), illustrating the fluidity of the bilayer.

In a next step, image processing was performed in order to localize single molecules with high spatial precision (Section 4.2.9). The algorithms were developed by Thomas Schmidt and colleagues [35, 36] and kindly provided for this work. The applied two-dimensional Gaussian fitting method is routinely used in the field of SMFM and SRM as an approximation for the PSF of the microscope [121]. Gaussian fitting requires low computational costs and was shown to provide a robust way for the precise localization of single molecules [35]. Information of a single-fluorophore intensity, width and position can be obtained from such a fitting method [35].

From the distribution of all single-molecule intensities mean values of 517 counts and 253 counts were determined at an illumination intensity of 2 kW cm^{-2} for VSG M1.6 ATTO647N and DOPE488, respectively. The single-molecule footprints depicted in Figure 2.2 illustrate that fluorophore signals were significantly more intense than background signal that resulted from the camera noise (Figure 2.2, inset). Next to camera noise, unspecific signals were further detected after the incorporation of DOPE488 or VSG M1.6 ATTO647N. These signal were usually less intense than the fluorophore signals ($\sim$ 100 counts for VSG M1.6 ATTO647N samples and $\sim$ 60 counts for DOPE488 samples). They can most likely be assigned to contamination by fluorescent dirt within the samples. However, such signals were efficiently removed from further data analysis by comparing their intensities and widths to previously determined single-molecule footprints of the dyes.

From the distribution of all single-molecule widths mean values of 0.33 μm (s.d. = 0.06 μm) and 0.36 μm (s.d. = 0.02 μm) were determined for DOPE488 and VSG M1.6 ATTO647N, respectively. In theory, the width of an Airy disk is given by $d = 0.61\ \lambda/NA$, where λ denotes the wavelength of the emission light and NA the numerical aperture of the microscope. The determined mean width of DOPE488 and VSG M1.6 ATTO647N molecules were found to be substantially larger then the theoretical values for both fluo-

rophores ($\sim 0.22\ \mu$m for ATTO488 and $\sim 0.27\ \mu$m for ATTO647N). The theory assumes a perfect lens with no aberration. Aberration, however, can arise from e.g. lens imperfection or from mismatches between the refractive index of the lens immersion medium and cell material or structures in and around the focal plane and result in a PSF that deviates from the calculated, theoretical PSF [122]. Further, lateral movement of a fluorescent emitter was found to distort the shape of a Gaussian-like profile and thus increase the width of a single-molecule footprint [123]. For a more precise determination of single-molecule footprints, DOPE488 or VSG M1.6 ATTO647N could be monitored static, e.g. in a SLB below its gel to liquid phase transition temperature.
In single-molecule fluorescence microscopy the localization precision of a fluorophore is determined by the ratio of the signal intensity of the fluorophore to the total noise level. SNR values were calculated as:

$$SNR = \sqrt{(w^2/N + px^2/(12*N) + (8*\pi*w^4*BG_{noise}^2)/(px^2*N^2))}, \qquad (3.1)$$

where w denotes the width of the single-molecule signals, N the mean number of all intensities counts, px the pixel size of the EMCCD camera and BG_{noise} the variation in the background signal. In SLBs, SNR values were usually calculated to be high (> 55). VSG M1.6 ATTO647N and DOPE488 were localized with a spatial precision of 15-20 nm in SLBs, which is in good agreement with commonly achieved localization precisions using small organic dyes [119].
In conclusion, VSG M1.6 ATTO647N and DOPE488s were successfully integrated into SLBs. High quality fluorescence images were generated, which facilitated the localization of individual molecules with high spatial accuracy. Further, VSG M1.6 ATTO647N and DOPE488 were quantified with respect to their single-molecule footprints.

3.1.2 Generation and analysis of single-particle trajectories

For the determination of VSG and DOPE488 diffusion coefficients, trajectories were generated from single-molecule localizations. The algorithm was developed by Thomas Schmidt and colleagues and applied a probabilistic approach to connect localizations in neighboring frames. It required the estimation of the particle diffusion coefficient as an input parameter for the connection of localizations. In order to prevent false particle connections, a repetitive D_{in} versus D_{out} analysis was performed for every scenario. Two major points have to be considered in generation of single-particle trajectories using such an approach, the density and the dynamics of the particles. At high densities individual particles often cross paths, making it difficult to follow an individual particle [124]. This accounts especially for particles that diffuse quickly (e.g. small proteins and peptides). For such a scenario, alternative methods were developed (e.g. Particle Image Correlation

Spectroscopy [47] or Raster Image Correlation Spectroscopy [125]). However, as exemplified in Figure 2.1 the particle density was low and imaging at appropriate frequencies (28-200 Hz) resulted in minor particle displacements in consecutive images. Hence, the trajectories were believed to reliably represent the motion of the particles. They were then further analyzed to determine the diffusion coefficients of the particles.
The mean square displacement (MSD) analysis of trajectories reflects a simple and widely spread tool to extract the diffusion coefficient and type of diffusion regime undergone by a particle. However, it also faces limitations as it averages a set of observations. If two populations with different diffusion coefficients are present in a sample or a particle undergoes a motion change, the MSD analysis fails to reconstruct the individual diffusion coefficients correctly [126]. This accounts especially for particles in the complex environment of a cell [127]. Alternative approaches were developed for the statistical analysis of particle trajectories to account for such scenarios (reviewed by Gal et al. [128]). Nevertheless, a MSD analysis can provide a robust method for the determination of the diffusion coefficient, especially when free Brownian motion of only one population is present, e.g. in the case of lipid diffusion in an isotropic medium like a SLB.
Rules to follow for the extraction of the diffusion coefficient from a MSD plot are frequently debated in the field. The precision of a MSD analysis can be improved by the number of localizations within a trajectory and the overall number of individual trajectories that contribute to the average MSD. However, deviations from linearity occur at large time lags, even in the case of pure Brownian motion. This is due the fact that MSD points are less averaged, because the number of corresponding displacements decreases, which results in large statistical fluctuations [50]. Saxton and Daumas stated that data points equal to $1/4 - 1/10$ of the tracelength should be used for the calculation of the diffusion coefficient [51, 52]. For integrated DOPE488 and VSG M1.6 ATTO647N a weighted mean tracelength of 13 and 54 localizations was found, which would cover a range of 1-5 data points in extreme cases. At least three data points are required to detect departure from linearity and thus the first three points of the MSD plot were used to determine the diffusion coefficients of the molecules. It was found, that the resulting diffusion coefficient was robust with respect to the range of data points (3-5) considered in the linear plot. E.g. in the case of VSG M1.6 ATTO647N diffusion in SLBs, a variation of max 4% was found when using 3 or 5 data points for a linear fit. This variation is small and hence, usually a linear fit to the first three data points was applied to calculate the diffusion coefficient.
Single-particle tracking requires multiple illumination cycles with defined time intervals between consecutive images. Further, single molecules are only localized with a certain precision, σ. Both aspects were considered in the analysis by correcting the MSD plot for the limitations in the temporal and spatial resolution (Section 4.2.9) as described in the literature [53, 54, 55].
Considering the limitations of the applied MSD analysis, calculated diffusion coefficients

of e.g. lipids and proteins in SLBs or the plasma membranes of *T. brucei* cells can be regarded as a description of the average motion behavior with high temporal and spatial resolution (Section 2.1.1, 2.1.2 and 2.2.3). The difficulty in resolving subpopulations in the MSD analysis is reminiscent of the limitations of early ensemble FRAP based measurements. FRAP studies initially allowed the determination of an immobile and a mobile fraction ([24]). Within the last decades the evaluation approach in FRAP based studies has been extended by the incorporation of various phenomena into the evaluation procedure, e.g. binding kinetics or multiple diffusive populations within a sample [129]. The FRAP measurements performed by Andreas Hartel [118] were the basis of this work, but did not include evaluation procedures for such phenomena. In order to verify the results of his studies in this work, FRAP measurements were performed under equal conditions. Following this approach, single-particle trajectories were categorized as immobile or mobile by comparing their MSD to the achieved single-molecule localization precision, σ. This allowed the determination of the population mobile fraction and the average diffusion coefficient of the mobile particles. Nevertheless, additional profit on information was obtained in this work, as SPT gives access to particle dynamics in the spatial resolution beyond the diffraction limit and the temporal resolution of ms. Further, confined diffusion or active transport could potentially be identified from the MSD plot (Section 1.1.3). Additionally, a more detailed analysis of single-molecule trajectories was performed for VSG M1.6 ATTO647N and its N-glycosylation deficient mutant, which were reconstituted into SLBs at various protein densities as well as and VSG M1.1 ATTO647N sparsely integrated into SLBs (Section 2.1.3). The analysis method was developed and applied by collaboration partners (Mislav Cvitković and Ana-Sunčana Smith) and included among others non-Gaussian statistics to remove immobile objects as well as thresholding and the calculation of probability likelihoods for the determination of subpopulations within a sample (for a proper description of the analysis method see [91]). This offered novel insights into the dynamics of single VSGs and will be discussed later.

3.1.3 Diffusion of VSG M1.6 and DOPE488 in SLBs

Previous studies of VSG dynamics were performed in SLBs via FRAP [100, 20]. The authors measured diffusion coefficients of 0.7-1 $\mu m^2\ s^{-1}$ and high mobile fractions ($\sim$ 80%) for various types of VSGs. Here, the diffusion of VSG M1.6 ATTO647N was now studied at low lateral concentrations in SLBs via SPT (Section 2.1.1). In this section it is evaluated, which similarities and differences both measurement methods provide. For the case of VSG M1.6, a basic MSD analysis of mobile VSG trajectories was performed without any previous separation of potential subpopulations. This approach reflects the constraints of FRAP measurements and was applied to measure the average diffusion of

VSGs with high spatial and temporal resolution. The MSD analysis revealed diffusion coefficients of 1.75±0.03 $\mu m^2\ s^{-1}$ for VSG M1.6 ATTO647N and 2.22±0.03 $\mu m^2\ s^{-1}$ for DOPE488. The VSG diffusion coefficient reflects a $\sim$ twofold higher diffusion coefficient than previously determined by FRAP at low protein densities. This difference can in part be explained by the individual length- and time-scales probed by the techniques and was observed for other proteins before [131]. Further, in this work VSG M1.6 ATTO647N and DOPE488 were integrated into SLBs at protein concentrations substantially smaller then in previous FRAP measurements. In FRAP experiments, the sensitivity of the CCD camera impeded arbitrary large dilutions of the labeled proteins and limited average protein-protein distances to $\sim$ 20-30 nm. In such a scenario, protein interactions do still permanently occur and potentially slow down the diffusion of the proteins. Thus, the experiments performed in this work represent a more precise measurement of the behavior of single VSGs in SLBs. The mobile fraction determined via SPT was high in both samples (> 98%), suggesting a homogeneous, defect free lipid bilayer with no protein or lipid clustering. Similar diffusion coefficients and mobile fractions were calculated for VSG M1.1 ATTO647N and VSG M1.3 ATTO647N at low lateral protein densities (1.6 - 1.8 $\mu m^2\ s^{-1}$), which suggests an overall similarity of VSGs at low concentrations. The determined VSG M1.6 ATTO647N diffusion coefficients are in good agreement with previously determined values for other GPI-anchored proteins in a SLB via SPT (e.g. prion proteins, 1.6 $\mu m^2\ s^{-1}$ [70]). The DOPE488 diffusion coefficient was found to be in the same range as determined for DOPE488 integrated into SLBs together with VSG M1.1 ATTO647N (2.688±0.005 $\mu m^2\ s^{-1}$, Section 2.1.3). The small difference might results from the individual trajectory analysis methods applied in each scenario.
Overall, the results illustrate that SPT was successfully applied for VSG M1.6 ATTO647N and DOPE488 reconstituted into SLBs at low concentrations. In the the following sections, systematic SPT and FRAP studies of VSG and lipid diffusion will be discussed.

3.1.4 Impact of protein density and N-glycosylation on VSG diffusion

In this work, a systematic study of the influence of VSG lateral density and N-glycosylation on the diffusion coefficient and mobile fraction of VSG was performed in model membranes. Previous attempts on these topics were performed by Andreas Hartel as a part of his doctoral thesis [118]. He measured VSG dynamics in SLBs and living trypanosomes via FRAP and found that removing N-glycans in trypanosomes that expressed VSG M1.6 or VSG M1.4 did not alter the diffusion coefficient of surface VSG but reduced the mobile fractions [105, 118]. Further, his studies in SLBs suggested a density depended decrease of the VSG diffusion coefficient. Comparison with the N-glycan deficient form of VSG M1.6 also suggested that N-glycosylation facilitates VSG mobility at high protein densities. In

order to verify these results, diffusion measurements of VSG M1.6 and VSG M1.6$_{mut}$ were performed systematically for a broad range of reconstituted protein densities in SLBs via FRAP. Further, complementary SPT of fluorescently labeled VSG was performed to study the dynamics of VSG in time and length scales beyond the resolution limit of the FRAP technique.

Generally, a high controllable degree of protein reconstitution was achieved with respect to lateral protein densities. VSGs were integrated into SLBs at average free protein distances (d_{free}) of 0-20 nm, which reflects 0.7-2 SE of live cells. This allowed quantitative investigations of the impact of VSG lateral density and N-glycosylation on the diffusion coefficient and mobile fraction. FRAP measurements confirmed the existence of a MCT above which the measured diffusion coefficient decreased. The MCT of VSG reconstituted in SLBs and measured by FRAP corresponded to an average free distance between individual VSGs of d_{free} = 5-7 nm (Section 2.1.2), which represents ∼1.3-1.5 SE. The quantification as surface equivalents illustrated, that the VSG coat operates very close to its MCT. The surface coat of living trypanosomes is indeed a very dense structure. This finding is in good agreement with the general accepted view of the VSG coat as a dense barrier that shields underlying invariant proteins [90]. FRAP measurements also revealed a high mobile fraction of VSG M1.6 ATTO488 at and above the MCT. A high mobility is a prerequisite for a complete surface coat turnover [99], the efficient accumulation of VSG antibody complexes at the flagellar pocket [97], and the exchange of surface VSGs during antigenic variation [130]. Immobile surface VSGs would be permanently exposed to the host immune system, and it can be assumed that such a case would lead to a rapid clearance of an infection. Thus, the VSG surface coat must be designed by nature to maintain a sufficiently high mobility, even at high protein densities. The quantification of surface VSGs also illustrates that trypanosomes could actually harbor more VSG on their cell surface. It appears to be beneficial for trypanosomes to be able to transiently adjust the VSG density on their cell surface, e.g. in the case of antigenic variation, when two types of VSGs populate the cell surface at the same time. Indeed, ectopic VSG overexpression raised the level of surface VSG to roughly 140% [105]. In this regime the diffusion coefficient and mobile fraction of VSG M1.6 ATTO488 was measured to be still unaffected, but any further increase of the protein density decreased the VSG diffusion coefficient and mobile fraction rapidly (Figure 2.5). These data illustrate, that the VSG coat density of trypanosomes is adjusted very close to its MCT, but naturally occurring density variations do not affect the dynamics of the overall VSG coat.

Next to the impact of lateral protein density, the influence of VSG N-glycosylation on the diffusion coefficient and mobile fraction was studied. FRAP measurements revealed, that the MCT of the N-glycosylation deficient form of VSG M1.6 ATTO488 was already reached at protein concentrations corresponding to d_{free} of ∼15 nm, which reflects ∼0.8-1 SE of live cells. Further, the mobile fraction was generally lower for the mutant form.

Extrapolated to the *in vivo* situation, an overexpression of VSG M1.6$_{mut}$ *in vivo* would reduce the surface VSG diffusion coefficient $\sim$ twofold. This could mean less efficient surface coat turnover rates and immobile VSG antibody complexes. Such a scenario could result in a rapid clearance of a trypanosomes infection inside a host.
In oder to study VSG diffusion *in vitro* beyond the resolution limits of FRAP, state-of-the-art SPT experiments were performed on the same samples. The diffusion coefficients measured via SPT were generally in good agreement with the diffusion coefficients determined in FRAP experiments. Again, the diffusion coefficients of VSG M1.6 and its mutant were most different at the MCT of VSG M1.6. In this regime, the N-glycosylation deficient mutant possessed a $\sim$ twofold reduced diffusion coefficient. The conformity of the results illustrates (i) that FRAP measurements can be used to reliably describe the diffusion behavior of VSGs in SLBs and (ii) the diffusion coefficients of VSGs are equal at the time and length scales of SPT. It has to mentioned that the applied MSD analysis averaged the motion behavior of a multitude of VSGs and individual populations might be overlooked. Small differences in VSG diffusion coefficients were measured via SPT at protein concentrations below the MCT. This was made evident by a comparison of the diffusion coefficients of VSG M1.6 ATTO647N determined via SPT at d_{free} » 20 nm (Figure 2.7). In this case, the diffusion coefficient was measured to be $\sim$twofold higher than the diffusion coefficient of VSG M1.6 ATTO647N at the MCT. As explained in Section 3.1.3, FRAP measurements cannot be performed in arbitrary large diluted samples and protein-protein interactions still occur at a d_{free} of 20 nm. Thus, at low protein concentrations, SPT must be performed to study the diffusion of VSGs.
FRAP measurements suggest that the measured decrease in the diffusion coefficient beyond the MCT might simply result from aggregation. However, a close inspection of individual VSG M1.6 ATTO647N trajectories revealed that the mobile fraction was > 90% independent of the protein density. This discrepancy can be explained by the temporal and spatial resolution limits of FRAP. Diffusion confined to domains below the lateral dimensions of the bleaching spot in FRAP will be assigned to the immobile fraction. The advantage of SPT is that individual trajectories can be analyzed for such properties. Applying this technique for VSG trajectories, different characteristics were observed for VSG M1.6 ATTO647N. The identification and detailed examination of such properties is work in progress and performed by collaboration partners (Mislav Cvitković and Ana-Sunčana Smith). Preliminary results of such an analysis revealed two regimes of free diffusion within the samples, a slow and fast moving population. Next to free diffusion (Figure 3.1, a), an increasing fraction of VSGs was identified in samples with increasing protein density, that was transiently trapped in domains well below the resolution limit of the FRAP technique (Figure 3.1, b and c).

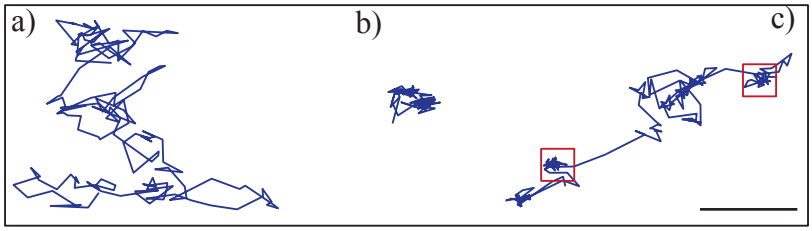

Figure 3.1: Anomalous behavior of VSG M1.6$_{mut}$ ATTO647N in model membranes. Domains were observed in reconstituted protein samples (d_{free} = 4 nm), in which VSGM1.6$_{mut}$ ATTO647N was transiently trapped. Exemplary trajectories illustrate free fast diffusion (a) or anomalous behavior in a whole trajectory (b) or parts of a trajectory (c). Red squares illustrate domains of potential trapping within a trajectory. The scale bar is 1 μm.

These domains were found in VSG M1.6 ATTO647N and VSG M1.6$_{mut}$ ATTO647N samples. The analysis of the trajectories further allowed the calculation of dissociation rates from such domains (Figure 3.2). While VSG M1.6 ATTO647N exhibited constant rates of unbinding form these domains, the N-glycosylation deficient mutant remained longer in these domains as the protein concentration increased. Thus, it was asked what

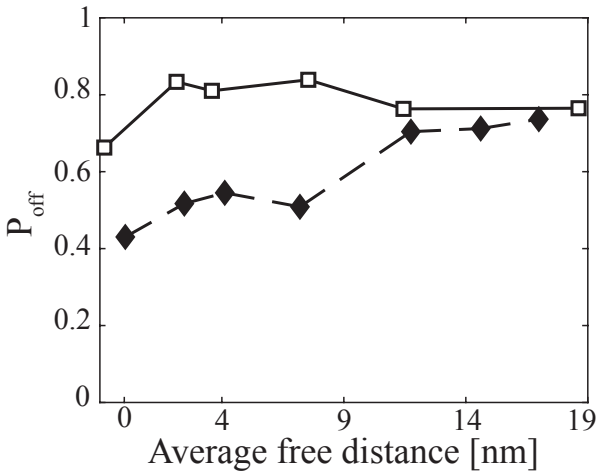

Figure 3.2: Transient trapping of reconstituted VSG at different protein concentrations. The probability of unbinding (P_{off}) from the traps as a function of the lateral VSG density is shown for VSG M1.6 (white boxes) and its N-glycosylation deficient mutant (black diamonds). The analysis was performed by Mislav Cvitković.

possibly caused the decreased unbinding probability of VSG M1.6$_{mut}$ ATTO647N. As protein-protein interactions permanently occur at high protein densities, it can be assumed that N-glycosylation might be relevant to e.g. prevent transient or permanent protein clustering. This is supported by the finding, that glycans induce repulsive forces and render proteins more soluble at high concentrations [132, 133]. One argument for transient protein clustering is the fact that VSGs were able to escape from the traps (Figure 3.1, c). However, also whole trajectories were found to be associated to these domains (Figure

3.1, b). This might be attributed to the fact that bleaching occurred before the proteins dissociated from the traps. So far it remains unknown whether the domains transiently or permanently existed in reconstituted protein samples.
Another explanation for this phenomena is that N-glycosylation might be relevant for the stability of the protein's tertiary structure. In a recent study that applied molecular dynamics simulations, it was found that N-glycosylation leads to an increased protein tertiary structure stability with less intramolecular fluctuations [134]. Such an increased stability might be beneficial to maintain an either relaxed or compact conformation and avoid permanent transition between both states. The recently discovered two main conformational states of VSG M1.1 [91] in combination with single-particle tracking performed in this work suggest that the N-glycosylation might indeed be connected to protein conformation (Section 3.1.5). Local protein clustering could therefore be the result of the inability to adjust to high protein densities and maintain this conformational state. This seems especially relevant for the N-glycosylation deficient form of VSGs. The further analysis of VSG trajectories might provide more detailed insights into the nature of the phenomena. Nevertheless, the example data illustrate the capability of SPT in detecting anomalous behavior of proteins in compartments well below the resolution limit of the FRAP technique.

3.1.5 VSG M1.1 conformation and lateral diffusion

Bartossek and Jones recently discovered, that VSG M1.1 and VSG I1.24 can adopt two main protein conformations [91]. They described a flexible linker region between the N-terminal region and the small C-terminal domain, which allows great protein flexibility. It was hypothesized, that this flexibility might be important for VSGs to respond to surface obstacles or variations in the VSG coat density.
The single-molecule experiments performed in this work support this assumption. Two distinct, freely diffusing populations were determined for VSG M1.1 integrated into a SOPC lipid bilayer (Section 2.1.3). A sophisticated analysis of single-particle trajectories (performed by Mislav Cvitković) revealed diffusion coefficients of 2.87 ± 0.03 μm^2 s^{-1} and 0.81 ± 0.05 μm^2 s^{-1} for the individual populations. The fast population dominated and was found to account for 96% of all mobile trajectories.
The applied analysis method facilitated a clear assignment of individual trajectories to the fast or slow population, even though a significant overlap was found from the distribution of population diffusion coefficients (Figure 2.1.3). The determination of population diffusion coefficients illustrates the capability of the analysis method to detect subpopulations in a set of trajectories. Averaging the information of all trajectories without a previous separation of populations would inevitably lead to a loss of information on the dynamics

of such subpopulations. Such a limited analysis was performed in Section and 2.1.1 2.1.2 and repeated for VSG M1.1 trajectories. The analysis resulted in a diffusion coefficient of 1.65 ± 0.02 μm^2 s^{-1} and a mobile fraction of 99% whereby no subpopulations were detected. Hence, the analysis method developed and applied by Mislav Cvitković represents a more accurate description of the diffusion properties of VSG M1.1.

Interestingly, the diffusion coefficient of the fast population of VSG M1.1 was found to be in the range of DOPE488 in SLBs (2.688 ± 0.005 μm^2 s^{-1}). This is surprising, as Hartel et al. have shown, that the proteinaceous part of GPI-anchored proteins influences the diffusion coefficient of the protein, even at low lateral protein concentrations [20]. In order to investigate this phenomena, it is suggested to repeat the experiments performed by Hartel et al. using SPT.

It has to be discussed, what causes slow and fast diffusion of VSG M1.1, intrinsic parameters like the protein conformation or external parameters like protein-protein interactions or membrane impurities. In order to exclude potential membrane defects, DOPE488 lipids were integrated into the same SLBs and their diffusion was monitored. The mobility of the lipid was very high and free diffusion was observed from the trajectories. Further, slow diffusing VSGs appeared randomly within a bilayer an no indication of any spatial correlations was found. Thus, no local interaction with e.g. the underlying support was assumed and potential membrane defects were excluded as a causal factor for reduced diffusion of VSG M1.1. Protein-protein interactions within the bilayer are also unlikely, since VSGs were integrated into the membrane at low protein densities (< 0.1 VSG per μm^2). Impurities resulting from the protein extraction are also unlikely, since only one fraction of proteins was obtained from the HPLC purification (see SI Figure 7 in [91] for an exemplary western blot of purified VSG M1.1). Thus, an intrinsic property of VSG M1.1 was most likely the reason for fast and slow diffusion. Hence, it can be assumed, that the distinct populations determined by SPT reflect the two main VSG M1.1 conformations. It remains unknown, which conformation can be assigned to the fast or slow population. A relaxed protein conformation covers larger membrane areas, thus the diffusion could be slowed down due to an increased friction with the membrane. On the other hand, the molecular size of the extracellular domain was found to influence the diffusion of GPI-anchored VSGs on the cell surface of trypanosomes and in model membranes [20]. The compact conformation extends further from the membrane, which would decrease the diffusion coefficient of the protein according to this finding. The assumption of the compact form as the slow diffusion population is supported by the hypothesis of the authors, that VSGs adopt to a diluted VSG coat density by converting to a relaxed state that covers larger areas. In such a situation the barrier function of the surface coat maintains and underlying invariant proteins are shielded from the host immune system. In the experiments of this work, the VSG density in SLBs was low and thus, a relaxed conformation could be assumed. A more detailed analysis of the single-particle trajectories from samples of different protein

concentrations (Section 2.1.2) could shed light on the relationship between lateral density and protein conformation. Further, the experiment should be repeated for other types of VSGs (e.g VSG M1.3 or VSG M1.5) to confirm a general structure-mobility relationship of VSGs.
It has to be mentioned, that the VSG models were obtained from proteins in solution and not, as naturally occurring, integrated into a lipid bilayer. This could affect the overall protein flexibility and conformation. High resolution techniques could be used in prospective experiments to investigate the conformational states of a VSG in its natural environment. This encompasses X-ray based analysis of protein crystals using microfocused beamlines (e.g. XFEL [135]) or state-of-the-art cyroelectron microscopy [136].
This is not the first time, that protein conformation was linked to its lateral diffusion. Schubert et al. [70] reported similar observations for GPI-anchored bovine prion proteins (PrP) in SLBs. PrP is susceptible to misfolding at acidic pH and SPT experiments revealed 40% difference in the diffusion coefficient under basic and acidic conditions (1.8 and 1.1 $\mu m^2\ s^{-1}$, respectively).
The single-molecule experiments performed in this work support the hypothesis that VSG M1.1 can adopt two main protein conformations. The flexibility of VSG might be of relevance to avoid local trapping caused by obstacles on the surface of living trypanosomes or facilitate a high mobility of VSGs at high lateral protein densities. Further, the continuous variation between the main VSG conformations could compensate density fluctuations within a VSG coat and facilitate a homogeneous coverage of the plasma membrane.

3.2 Single-molecule microscopy in living trypanosomes

3.2.1 Cell viability in cross-linked hydrogels

In this work, hydrogel embedding was introduced as a tool to immobilize living trypanosomes for single-molecule microscopy. Three different hydrogels were tested, all with individual polymer compositions and concentrations. Generally, all hydrogels were found to be highly cytocompatible and facilitated imaging living trypanosomes for at least 30 to 60 minutes.
The first two hydrogels (HA-SH/P(AGE-*co*-G) and PEG-NB/PEG-dT) were polymerized based on thiol-ene chemistry. Thiol-ene reactions are organic reactions between a thiol and an alkene to form alkyl sulfide. The reaction proceeds through a Michael-addition pathway, catalyzed by either a base or a nucleophile. The conditions of this chemistry have been shown to be mild and facilitate a high cellular viability, e.g. in 3D human cell culture experiments, which includes peptide-functionalized PEG hydrogels [137] or norbornene functionalized hyaluronic acid [138]. The entire cross-linking process of HA-

SH/P(AGE-*co*-G) and PEG-NB/PEG-dT hydrogels required continuous UV-illumination for several minutes. UV-light is commonly associated with the production of reactive oxygen species, which can cause severe cell damage [139]. However, thiol-ene based cross-linking required only low UV-illumination intensity (1 mW cm^{-1}). The cytocompatibility of the UV-illumination process was shown in Section 2.2.1, where no negative effects on the viability were measured in control cells after UV-illumination (Figure 2.17). Care was taken when using the photoinitiator I2959 for hydrogel cross-linking. Reactive products of the photoinitiator originate upon UV-illumination. They readily react with the hydrogel components or eventually, molecules on the cell surface. Hence, only low concentrations ($< 10\ \mu g\ ml^{-1}$) were used for cross-linking process. In this range, the viability of trypanosomes was shown to be unaffected up to 34 h in cell culture experiments when the photoinitiator was present [140]. Further, hyaluronic acid or chemically inert PEG are commonly used as hydrogel scaffolds for the embedding of e.g. human cells and their cytocompatibility was proven in several cell culture experiments for various types of cells [138, 141].

The third hydrogel tested was cross-linked based on Michael-addition chemistry and consisted of PEG-VS and HA-SH. Cross-linking of the polymers was possible without UV-illumination and fast ($\sim$ one minute) under alkaline conditions (pH 8.3), which allowed the centrifugation of trypanosomes during the gel formation process. Centrifugation immobilized trypanosomes in close proximity to the glass support and facilitated a beneficial orientation of the cells for SMFM. The cytocompatibility of the hydrogel was found be in the same range as for HA-SH/P(AGE-*co*-G) and PEG-NB/PEG-dT hydrogels. The high viability of embedded trypanosomes in all hydrogel suggests a generally good cytocompatibility, independent of individual polymer compositions or cross-linking chemistry. Hydrogels are water-swollen networks, originally designed to mimic the 3D-structure of the extracellular matrices in cell culture experiments [142]. Hence, hydrogels were specifically designed to facilitate a high viability of embedded cells.

Propidium iodide (PI) was used as a fluorescent life/dead marker to monitor the viability of immobilized trypansosomes. PI is commonly used in hydrogel or flow cytometry experiments to determine the fraction of living and dead cells [143]. The results shown in Section 2.2.1 illustrate that PI is also suitable to determine the fraction of dead trypanosomes in hydrogels. A strong intracellular fluorescence signal was measured for chemically fixed control cells as well as dead cells inside the hydrogel.

The viability of embedded trypanosomes was significantly reduced after 1 h of immobilization in all hydrogels. This was most likely caused by an insufficient supply of the cells with glucose within the hydrogels or side effects of an incomplete cell division process that is impeded by the immobilization. The first argument is supported by the finding, that diffusion of soluble material in hydrogels strongly depends on the hydrogel composition [106]. This suggests, that pure PEG-based hydrogels (PEG-NB/PEG-dT) are

less permeable for glucose or other soluble molecules that are important for the viability of trypanosomes. Such properties could explain the reduced cytocompatibility after 30 min or at 37°C in PEG-NB/PEG-dT hydrogels. However, the high fraction of viable cells over 30-60 min after immobilization provided sufficient time to perform single-molecule microscopy in living trypanosomes.
In prospective cell viability experiments, membrane potential sensitive fluorescent dyes could be used to detect any impairment of membrane integrity in immobilized trypanosomes. This will become important when studying plasma membrane associated processes like surface VSG diffusion or membrane leaflet specific motion of tracer molecules. Energy depended intracellular transport (e.g. vesicles in the endocytosis route) could be monitored to guarantee the viability of immobilized trypanosomes. Small quantum dots (20 nm diameter) could serve as tracer molecules. Preliminary data showed that they are rapidly endocytosed by a trypanosome at the flagellar pocket and could potentially facilitate imaging intracellular transport within the endocytosis route (data not shown).
In conclusion, hydrogel embedding was successfully introduced as a tool for the immobilization of living trypanosomes. The hydrogels were found to be highly cytocompatible for $\sim$ 60 min, which is sufficient for microscopic studies in live trypanosomes.

3.2.2 Quantification of the hydrogel immobilization efficiency

In Section 2.2.1 the hydrogels were quantified with respect to their autofluorescence properties in the spectral range of the fluorophore as well as their immobilization efficiency.
The immobilization efficiency was verified by imaging a flagellar structure of immobilized trypanosomes with high resolution. To this end, a transgenic cell line that expresses kinesin-MORN::eYFP was used for the experiments. The cell line was generated by Ines Subota and provided for the experiments. She found that the fusion protein is located at the flagellar region, elongating from the basal body next to the kinetoplast until the flagella tip (see Figure 2 in [111] for an exemplary fluorescence image of the flagellum). Similar results were found for trypanosomes immobilized in hydrogels, as illustrated in Figure 2.12, (a). Hence, kinesin-MORN::eYFP was regarded as a representative to study the structure of the axoneme.
In a preliminary experiment it was studied, whether the fusion protein is actively transported along the flagellum, as it was measured for other kinesin proteins in living cells before [144]. From the single-molecule fluorescence movies, no diffusion or directed motion of kinesin-MORN::eYFP could be detected (data not shown). This might be due to a strong binding of the kinesin domain to the axoneme or the MORN-domain to the flagellar membrane. Studies in other organisms revealed that MORN-motives are associated with membrane binding or the formation of protein scaffolds involved in tight membrane adhesion or organelle fission [145]. The MORN-motive might have a similar function *T.*

brucei where it was found to be present in e.g. the bilope structure [146].
In order to quantify the immobilization efficiency of the hydrogels, fluorescence microscopy was performed on living and chemically fixed trypanosomes. While it might be possible to recover the correct axonemal diameter from diffraction-limited fluorescence images of embedded trypanosomes after image deconvolution, the error bars associated with the diffraction-limited images are substantially larger than in SRM. As a consequence, residual flagellar beating might be overlooked using diffraction-limited fluorescence imaging. Thus, SRM was performed to resolve the axonemal diameter precisely and detect remaining flagellar movements. If structural details need to be resolved in SRM, a sample requires a high label density to satisfy the Nyquist-Shannon sampling criterion [40]. The theorem basically states, that the sampling frequency must be greater than twice the frequency of the smallest structure in the image. It was asked, whether sufficient eYFP molecules could be localized at the flagella region to fulfill the Nyquist-Shannon sampling criterion. Indeed, even without tetracycline induction the basal level of kinesin-MORN::eYFP expression resulted in a high label density at the flagellar region of transgenic cells. By exploiting the intrinsic blinking behavior of eYFP molecules at high illumination intensities as demonstrated in the literature [65] [112], single diffraction limited kinesin-MORN::eYFP spots became visible at the axonemal region of trypanosomes (Figure 2.12, B). The autofluorescence properties of HA-SH/P(AGE-*co*-G) and PEG-NB/PEG-dT hydrogels and embedded trypanosomes were quantified in the spectral range of the fluorophore. Hydrogel and cellular autofluorescence accounted always for < 3% of total signals (Figure 2.14, A). This can in part be attributed to the absence of aromatic compounds in the chosen hydrogel components. Further, the cleaning procedure of the glass support (Section 4.2.7) efficiently removed any fluorescent contaminants and the hydrogel was most likely not permeable for large kinesin-MORN::eYFP molecules from dead cells. As a consequence, the hydrogels were found to be free of substantial background signal. The low autofluorescence properties of the hydrogels in the spectral range of eYFP in combination with a strong fluorescence of the fluorophore facilitated the localization of single-eYFP molecules with high spatial precision (24$\pm$5 nm).
Both aspects, the high label density at the flagellar region and the achieved localization precision facilitated the reconstruction of super-resolution images and allowed the precise determination of the axoneme diameter (203$\pm$36 nm in HA-SH/P(AGE-*co*-G) hydrogels and 191$\pm$23 nm in PEG-NB/PEG-dT hydrogels, Figure 2.15). It has to be mentioned, that the signal distribution of kinesin-MORN::eYFP was not homogeneous throughout the flagellum. Flagellar segments with more frequent kinesin-MORN::eYFP signals were found next to diluted parts. Such inhomogeneities were not considered in the analysis, as only the mean diameter and mean label density were determined along the flagellar region. As a consequence, the presented results might underestimate the real diameter of the axoneme. However, kinesin::MORN itself is substantially large ($\sim$ 80 kDa). Even

though, no structural details of kinesin::MORN are published, the generally accepted view of kinesin as a protein with a extended tertiary structure [147] leads to the assumption that the same accounts for kinesin::MORN. C-terminal labeling of eYFP at the MORN domain of the fusion protein most likely positioned the fluorophore to a certain distance from the the axoneme. As a result, the determined mean diameter would overestimate the axoneme structure. Further, spatial inhomogeneity of biological structures is common and the Nyquist-Shannon can often be achieved at lower total label densities, as long as the local density of the structure in sufficiently high. This was given for kinesin-MORN::eYFP at the flagellar region.
Comparison of the full-width half-maximum of the averaged flagellar signals from living and chemically fixed cells revealed that 15% (w/v) HA-SH/P(AGE-*co*-G) and 10% (w/v) PEG-NB/PEG-dT hydrogels provided sufficient stiffness for a complete cell immobilization. Similar axoneme diameters were further measured in electron micrographs [113, 114], which leads to the assumption that the applied hydrogels efficiently immobilized living trypanosomes. The stiffness of 15% (w/v) HA-SH/P(AGE-*co*-G) hydrogels was analyzed by Simone Stichler. She measured a Young's modulus of 150 kPa. This value is high compared to the stiffness of hydrogels that are usually used in cell culture experiments (< 40 kPa [107]). These gels are designed to mimic the extracellular matrix and they are commonly used to study static of slow moving cells. Trypanosomes, however, are intrinsically fast moving. Even though swimming trypanosomes only generate forces < 10 pN [103], a high stiffness is obviously required to impede any residual flagellar beat. This hypothesis is supported by the finding that low hydrogel concentrations (10% (w/v) HA-SH/P(AGE-*co*-G), Section 2.2.1) could not suppress flagellar motion sufficiently and thus resulted in a spread out intensity distribution of the kinesin-MORN::eYFP signal (Figure 2.15).
The presented kinesin-MORN::eYFP expressing trypanosomes are the first images of a super-resolved structure in a living trypanosome. The applicability of the method for other flagellates is straightforward, given that these cells are viable inside the gel and exhibit low autofluorescence properties in the spectral range of the used fluorescent label. In such a case, the methodology can facilitate prospective studies of e.g. static or dynamic processes with high spatial and temporal resolution. As a first application of the method in *T. brucei*, SMFM was performed for a tracer molecule that located to the inner leaflet of the plasma membrane.

3.2.3 Plasma membrane organization in living trypanosomes

The plasma membrane of *T. brucei* is of major importance for the survival of the parasite in the bloodstream of a mammalian host or inside the tse tse fly. It is not only the foundation of the GPI-anchored VSG coat but also contains a multitude of associated proteins, e.g.

ion pumps, channels and cytoskeleton associated proteins [148]. Attempts to study the localization of every protein encoded in the genome of *T. brucei* have been made recently [149], including parts of the plasma membrane proteome. The approach uses fluorescent protein tagging in a high-throughput assay and the project provides fluorescence images of transgenic cell lines. However, no detailed information of the distribution of the fusion proteins within the plasma membrane are available in living cells and the provided fluorescence images are and not analyzed for potential distribution patterns or domains. The same accounts for the distribution of lipids in *T. brucei*. While the lipid composition of trypanosomes as a whole was found to be comparable to eukaryotic cells [150], the plasma membrane composition was not studied in isolation. Discussions about the existence of membrane structuring elements, especially lipid and VSG domains within the plasma membrane did not reach any certain conclusion [111] and it remains largely unclear how the plasma membrane is organized in *T. brucei*. The only studies addressing membrane organization in living trypanosomes measured the dynamics of surface VSG or fluorescent lipid tracer molecules [20, 105, 100] using FRAP and no indications of membrane structuring were found on the time and length scales of the method.

As a part of this work, SMFM was performed in living trypanosomes to study the organization of the inner leaflet of the plasma membrane on the nanometer scale (Section 2.2.2). To this end, the fusion protein HASP::eYFP was constitutively expressed in *T. brucei* cells and used as a tracer to probe for the inner leaflet of the plasma membrane. Originating from *Leishmania major*, the dual acylated HASP protein targets to the plasma membrane of the cells, where it locates to the outer leaflet [151]. This mechanism is believed to be absent in *T. brucei* and HASP::eYFP most likely attaches to the inner leaflet of the plasma membrane. This assumption is supported by immunofluorescence detection experiments (see Figure 3 in [115]). The strong hydrophobicity of the dual fatty acyl anchor was further found to stably attach proteins to a membrane [116]. HASP::eYFP contained only the first 18 amino acids of the original HASPB protein from *Leishmania major* N-terminally tagged to the eYFP. This short sequence was found to be sufficient for dual acylation of the protein [151]. Hence, the fusion protein can be regarded as a membrane-anchored eYFP and thus, a fluorescent analogue to a lipid of the inner plasma membrane leaflet. Previous ensemble FRAP measurement of embedded trypanosomes that expressed HASP::eYFP revealed a diffusion coefficient of $\sim 0.1\ \mu m^2\ s^{-1}$ and a high mobility of the fusion protein in the inner leaflet of the plasma membrane (mobile fraction > 70%). The diffusion coefficient was found to be ∼twofold higher than the diffusion coefficient of surface VSG determined via FRAP (Figure 6.3). Subsequently, single-particle tracking of HASP::eYFP immobilized cells were performed. The fast movement of the fusion protein out of the focal plane and strong blinking behavior of eYFP at high illumination intensities resulted in trajectories of short length (< 10 localizations per trajectory), which impeded quantitative measurements of HASP::eYFP dynamics via SMFM. The mobility of HASP::eYFP was exploited to

sample the plasma membrane and the blinking ensured the detection of isolated diffraction limited HASP::eYFP spots. In this way, a multitude of HASP::eYFP molecules were localized during the imaging procedure, which allowed the reconstruction of super-resolution images. Generally, this approach is reminiscent of the concept of PALM, but without the activation of the fluorophore prior to imaging. From all localizations, the inner leaflet of the plasma membrane was scanned for a potential organization or distribution pattern. The combination of super-resolution imaging and quantitative statistical analysis was shown to be suitable to study the protein distribution in cells before [152].

From the super-resolution images, a potential membrane structuring was observed (Figure 2.18). This was confirmed by a Ripley's analysis of HASP::eYFP localizations. Specific domains within the membrane were found where HASP::eYFP appeared rather diluted or accumulated (Figure 2.19).

It can be asked, what possibly causes such a distribution. Dual acylation of proteins was shown to result in a marker for ordered lipid domains [153, 154]. However, the spatial expansion of the domains of several hundred nanometers and the stability over a prolonged period of time are arguments against the current view of rafts as small and dynamic objects. In order to study the dynamics of HASP::eYFP more precisely, the temporal resolution of the imaging procedure would need to be substantially improved. This could be achieved by using a fluorescent tracer with photophysical properties that allows fast acquisition cycles and thereby resolve fast dynamic states in the inner leaflet (e.g. SNAP-tag in combination with a SNAP-Cell 647-SiR dye). Similar experiments were performed before, illustrating the temporal occurrence of small size local trapping [155], which could be resolved in living cells by increasing the temporal resolution.

A possible explanation that could potentially explain the distribution of HASP::eYFP in the inner leaflet of the plasma membrane is an interaction with the cellular cytoskeleton analogous to the picket and fences model by Kusumi et al. [56]. In trypanosomes, the cytoskeleton consists of subpellicular microtubules that are highly organized. The distance of the microtubules to the membrane was measured from electron micrographs and found to be 14 ± 4 nm (see SI Figure 3 in [115],). This is substantially larger than the dimension of the eYFP molecules (< 5 nm). Under the assumption, that no substantial membrane denting occurs in immobilized cells, no direct interaction with the microtubules can be expected. However, the microtubules were found to be connected to each other and the plasma membrane via a class of microtubule associated proteins (MAP) [156]. The most promising MAP to explain the distribution of eYFP, is the whole cell body protein (WCB), which possesses a membrane binding domain and can interact with microtubules [157, 158]. The anchoring of WCB in the plasma membrane could explain the diluted domains found in the experiments.

More precise explanations of the distribution within the plasma membrane could be given after a two-color single-molecule experiment. Fluorescence labeling of MAP proteins

could facilitate studying their spatial distribution within the membrane and simultaneous monitoring of a fluorescent tracer could reveal interactions with the MAP proteins. Further, the extension to a microscope setup capable of three-dimensional single-molecule identification (e.g. astigmatism based approach) could erase any distortions that arise from a possibly undulated plasma membrane of immobilized cells. Prospective experiments could also use a multi-color approach to label specific regions of the cell membrane (e.g. the flagellar pocket, the flagellum or both leaflets) and look for evidence of inter-leaflet coupling and elucidate the interaction of surface VSGs with potential membrane domains in the outer or inner leaflet of the plasma membrane.

3.2.4 VSG dynamics in live trypanosomes

Previous investigations of VSG dynamics in live trypanosomes were limited to FRAP measurements. They applied fringe pattern or line-bleaching in agarose or gelatin embedded cells [100, 20]. It is questionable, whether the small cell size and architecture allow a precise determination of the diffusion coefficient and mobile fraction using a method like FRAP that is limited to the range of seconds and micrometers. Further, it was demonstrated that FRAP has a limited capability of detecting and considering membrane bending and the calculated diffusion coefficients and mobile fractions might be underestimating the real molecule dynamics [159]. Thus, the results from previous FRAP measurements of VSG dynamics can be regarded as an approximation for the surface VSG diffusion coefficient in living trypanosomes.

The situation of VSGs diffusing on the plasma membrane of a trypanosome with endocytosis being restricted to the flagella pocket is reminiscent of the narrow escape problem (NEP) in two dimensions [160]. It is a common problem in biology and physics, in which a Brownian particle is restricted to a given domain with reflecting borders. The escape from such a domain is limited to a small window. An example of a NEP is e.g. the activation of genes by transcription factors or the diffusion of a molecule in a dendritic spine with a narrow cylindrical neck. The mean time a particle needs to escape at the window is exponentially distributed. The mean first passage time ($\bar{m}$) that characterizes this decay can be calculated, and for a VSG on the cell surface it is approximated by:

$$\bar{m} = \frac{A}{(2\pi D)} ln \frac{1}{\varepsilon}, \tag{3.2}$$

where D denotes the diffusion coefficient, A the surface area with a centrally positioned circular opening of radius a and ε the dimensionless radius a/C with C being the circumference of the surface (equation from David Holcman, personal communication). For a BSF trypanosome with a surface area of 100 μm^2 [20] and a radius of the flagella pocket of $\sim$ 500-800 nm, the diffusion coefficients determined in the FRAP measurements would

lead to a mean first passage time, $\bar{m}_{VSG}$, of 40-130 minutes in the extreme cases. This is in strong discrepancy with experimentally measured VSG coat turnover rates ($\sim$ 10 min, [99]).

In this work, the surface VSG dynamics in live trypanosomes was studied in hydrogel immobilized cells via SPT. Can the results from single-particle experiments explain the fast VSG coat dynamics *in vivo*? Indeed, a basic MSD analysis that averages the motion of all mobile trajectories revealed a VSG diffusion coefficient of 0.11 ± 0.08 μm^2 s^{-1}. This is substantially higher than diffusion coefficients determined in FRAP experiments. Using Equation 3.2, $\bar{m}_{VSG}$ = 7-40 min for the extreme cases. Further, a high mobile fraction was measured (98%), suggesting that no aggregates or immobile VSGs are present on the cell surface. This is in good agreement with the results from studies of VSG dynamics in SLBs in this work, in which the VSG coat was found to be very dense but still maintains a high mobility. It is also in good agreement with the finding that VSG-antibody complexes accumulate at the flagellar pocket side, mediated by hydrodynamic drag forces [97]. This process requires a high mobility of surface VSGs. Further, in a recent study, the dynamics of VSG coat replacement after antigenic variation and the impact of this process on successful immune evasion was investigated [130]. The authors found, that full coat replacement requires several days to complete (4.5 days) but the cells are only vulnerable to clearance by early IgM-antibodies for the first 29 h due to a fast dilution of the formerly expressed VSG. Again, a high protein mobility is a prerequisite for the efficiency of the process. Immobile VSGs would be presented prolonged to the host immune system and mediate a fast clearing of the trypanosome population.

It has to be mentioned that the cell architecture of a trypanosome deviates from the simplified assumptions from Equation 3.2 and it remains questionable whether the higher diffusion coefficients determined in SPT can solely explain the fast VSG coat dynamics. Trypanosomes are as long as $\sim$ 20 μm, but the cell width is only 2-4 μm at the flagella pocket and as small as < 1 μm at the the anterior end. Thus, substantial membrane curvature is present, which limits the observable space on the cell membrane to a great degree in 2D-fluorescence microscopy. For single-particle tracking experiments, this causes two major problems. First, the obtained single-particle trajectories are short for highly dynamic particles, since rapid diffusion out of the focal plane occurs. Second, VSG trajectories are projections of three-dimensional diffusion over the curved plasma membrane on the two-dimensional image plane. This means, that for a particle, which diffuses perpendicular to the image plane, the projected displacement will be less than the actual displacement. This applies especially to VSGs diffusing at the edges of the cell membrane but might also be relevant for all VSG trajectories, since the plasma membrane of immobilized cells seems to be rather vaulted than smooth (Figure 2.21, A) and the orientation of a cell after embedding might not be planar to the image plane.

The length of VSG trajectories on the cell surface was substantially improved in the ex-

periments by using the camera built-in cropped mode and frame-transfer readout modus. This allowed fast acquisition cycles up to 200 Hz and resulted in trajectories with weighted mean trace length of 28 localizations. However, membrane curvature is still present and difficult to consider in 2D-experiments, since a detailed knowledge of the surface architecture would be required to recalculate the correct displacements. Attempts to generally consider such a situation were made on the example of bacteria [161, 162] and the authors concluded, that the measured diffusion coefficients are significantly underestimated. This is most likely also true for VSG diffusion on the trypanosome plasma membrane and hence, a VSG diffusion coefficient $> 0.11\ \mu m^2\ s^{-1}$ can be estimated. This would lead to even smaller values of $\bar{m}_{VSG}$. Thus, the results from SPT in this work approach the experimentally determined values for VSG coat turnover rates.

From the applied MSD analysis, no deviations from pure Brownian motion were observed, since a linear increase in the MSD was found for the first three data points. Even by including more MSD data points (5), no indications for active processes or confined diffusion could be found. However, the analysis averages the information of all mobile VSG trajectories and such individual characteristics might be overlooked. A more detailed analysis of the VSG trajectories could reveal distinct VSG motions on the cell surface, e.g. directed transport or local trapping. Directed transport could be detected e.g. by analysis of the individual MSD plots or by including the information of angles between consecutive steps as demonstrated by Arcizet et al. [163]. However, such an analysis would also require the information of the 3D-particle localization and improved statistics to avoid misinterpretation of molecules diffusing axially.

As the obtained VSG trajectories remained still relatively short, even at an increased acquisition speed, a method recently published by Holcman et al. [164] might be suitable to calculate local velocity fields and diffusion coefficients on the cell surface. The method divides the cell surface in subdomains and averages the limited information of a multitude of short trajectories within each subdomain. This way location-specific dynamics can be detected. This might be of relevance for specific areas on the surface of a living trypanosome, e.g. in close proximity to the flagella pocket or at the flagellum. This approach is currently tested in collaboration with Torsten Paul and Philip Kollmannsberger, experts in the field of computational image analysis. The validity of this approach increases with the trajectory density and the experimental design of surface VSG labeling and data acquisition was adapted to this.

A major challenge was the generation of a multitude of VSG trajectories on the cell surface, since photobleaching during the imaging limited the number of VSG trajectories substantially and the number of fluorophores that are recorded at the same time has to be low to ensure proper tracking. Common genetic labeling of VSGs in *T. brucei* is difficult and regularly fails. The cells seem to possess a tight control mechanism that detects substantial changes in the structure of VSGs, and VSG-fusion proteins are often not presented on the

cell surface of the parasite. Hence, small organic fluorescence dyes were used to covalently label surface VSGs via their primary amines. The ATTO647N dye used is commonly used in SMFM and was proven to allow multiple illumination cycles before bleaching occurs [165]. This labeling approach is rather unspecific, but the dense arrangement and abundance of VSGs in the surface coat ensures that the vast majority of labels attaches to VSGs. About 95% of all surface proteins are VSGs [87] and the small invariant proteins are hidden below the VSG coat. Thus, it can be estimated that < 5% of the labeled proteins are not VSGs.

In order to perform single-molecule microscopy, the label density on the cell surface must not be too high. At high densities individual particles often cross paths, making it difficult to follow an individual particle [124]. In order to increase the number of recorded traces without increasing the label density, reactive ATTO647N molecules were allowed to diffuse through the hydrogel background, in which living trypanosomes were embedded. This way, bleached fluorophores could be readily replaced by fresh dyes binding from the solution. The pH value of the buffer (8.3) was chosen to optimize the reactivity of surface VSGs to the ATTO647N dyes. This continuous labeling strategy allowed to generate a multitude of surface VSG trajectories, but on the downside increased the background signal substantially. It was found, that the background fluorescence was reliably removed in the image processing procedure, but VSG surface trajectories remained. The labeling concept in combination with the data analysis procedures explained, might allow to study the VSG dynamics more precisely in prospective experiments.

Another possibility to improve the quality of the measurement is the extension of the microscope setup to facilitate 3D fluorescence detection. Established methods include e.g. astigmatism based imaging or the manipulation of the phase of the emitted light [166, 167]. It was demonstrated that particle trajectories can be generated in three dimensions, which improved the investigation of molecule dynamics in a cellular environment [168]. The axial depth of imaging using astigmatism can comprise several micrometers, when highly fluorescent labels (e.g. quantum dots) are used [167]. Such a range covers the width of the plasma membrane of a planar, immobilized *T. brucei* cell. In astigmatism based imaging, single VSGs could be monitored and followed on the cell surface on during their route through the endosomal apparatus. Further, the VSG dynamics could be studied in the flagella pocket, a three dimensional invagination of the plasma membrane ($\sim 1\ \mu$m). In combination with simultaneous two-color SMFM, static cellular structures or specific regions could be counter labeled and the interplay between VSG dynamics and their distribution could be studied.

It has to be evaluated, how the immobilization procedure might have affected the mobility of surface VSGs. The high mobile fraction of VSGs on living trypanosomes determined by SPT indicates no aggregates or trapping caused by the hydrogel immobilization procedure. In order to investigate the impact of the embedding method systematically, VSGs were

incorporated into preformed SLBs at different protein densities and the buffer reservoir above the bilayer was exchanged for a hydrogel solution. Subsequently, the hydrogel was cross-linked. This mimics the situation of embedded trypanosomes. SPT of integrated VSGs was performed before and after the addition and cross-linking of the hydrogel. From single-particle trajectory measurements at lateral protein densities that equal those on the living cells and above (SE $\geq$ 1), no affect on the diffusion coefficient was measured. At low lateral protein densities, however, a significant drop in the diffusion coefficient was observed (from $\sim 1.26\ \mu m^2\ s^{-1}$ to $0.85\ \mu m^2\ s^{-1}$). This might be explained by void membrane areas in diluted VSG samples, that are covered by hydrogel polymers prior to cross-linking and locally trap single VSGs once the gel has formed. It was shown, that small molecules like single domain antibodies ($\sim$ 15 kDa) can partially penetrate the VSG coat on living cells, but larger molecules are excluded from any membrane proximity [169]. The hydrogel polymers used for the formation of gels cover a range of 10-24 kDa but quickly form macroscopic structures that are too large to intercalate between VSG proteins. It can thus be hypothesized, that no negative effect on the protein motion in dense VSG coats occurs upon hydrogel cross-linking. One hypothesis that can explain this observation is that a thin layer of solvent remains between the VSG coat and the hydrogel, where it forms a lubricating layer. It is suggested that the single-particle trajectories from the control experiments need to be analyzed in detail to back up this interpretation.
In summary, single-particle tracking of surface VSGs was successfully performed for the first time in living trypanosomes. The analysis revealed, that VSGs exhibit a diffusion coefficient, which is substantial larger than previously determined in FRAP measurements. No deviations from Brownian characteristics were observed from VSG trajectories, however, substantial improvements in the imaging procedure (e.g. 3D single particle localization) and trajectory analysis need to be made to verify the results. Further, the extension to simultaneous two-color SMFM could improve the quality of the images and facilitate studies of VSG dynamics in specific areas of the plasma membrane.

3.2.5 Two-color single-molecule fluorescence microscopy

In order to facilitate simultaneous two-color single-molecule fluorescence microscopy without the extra costs of a second EMCCD camera, an emission light image splitter was implemented into the single-molecule fluorescence microscope setup as a part of this work (Section 2.1.4). The spatial separation of the emission light facilitated the simultaneous sample illumination with both laser lines. However, the separation of the emission signal required additional image processing in order to study any spatial correlation of two types of molecules. The concept of using immobilized multi-fluorescent TetraSpeck beads was adopted from Semrau et al. [53]. The authors achieved an image registration of both

color channels with a mean precision of $\sim$10 nm, which was beyond the precision of single-molecule localization in their experiments (40-50 nm). With a mean precision of 25 ± 10 nm after image registration in this work (Section 2.1.4), comparable results were achieved. The mean precision was only slightly larger than the achieved localization precision for DOPE488 or ATTO647N labeled VSGs in SLBs (15-20 nm) and in the range of VSG ATTO647N in immobilized trypanosomes ($\sim$ 30 nm). Thus, the image processing generally facilitates simultaneous two-color single-molecule experiments without adding substantial imprecisions to the experiments.

It has to be mentioned that the adjustment of the image splitter can affect the precision of the transformation process in different ways. First, the size of the images determines the level of lateral chromatic aberrations. The distorting effect is larger towards the edges of an image and increases with image size. The precision of the transformation was only shown for an image size of $\sim$20 μm and has to repeated when significantly larger areas are imaged. Second, the applied Matlab function fits a local weighted mean transformation to a set of defined fixed and moving reference points that are related by a global second degree polynomial across the entire ROI. Fitting data sets subject to chromatic aberrations using second degree polynomial were shown to provide good results for the registration of two color channels [110]. However, the algorithm does not consider image distortions arising form e.g. rotation of one channel versus the other. The image splitter device generally facilitates rotational image adjustment by tilting mirrors. Care must be taken to precisely align both color channels on the EMCCD camera prior to imaging. Alternatively, rotational distortions could be erased in the imaging process by including suitable algorithms (e.g. Matlab built-in function fitgeotrans.m). As stated in the description of the algorithm for for image registration, the transformation precision increases with the number and spatial homogeneity of the reference points. Thus it is recommended to image a multitude of immobilized beads spatially distributed in the color channels. In the experiments, $\sim$ 2800 beads per μm^2 were localized, which resulted in a good image registration precision.

The spatial image separation comes at the expense of an increased image interval time as the camera readout speed depends on the size of the imaged area. For highly dynamic processes, it has to be evaluated individually whether the lag time between consecutive images allows studying spatially correlated processes. Surface VSG diffusion, for example, was shown to be highly dynamic and needs to be imaged in a small ROI to generate long VSG trajectories Section 2.2.3.

Implementation of simultaneous two-color fluorescence microscopy can facilitate versatile prospective experiments in a SLB or in living, embedded trypanosomes. An exemplary experiment could focus on hydrodynamic driven sorting of VSG-antibody complexes in a supported lipid bilayer within a microfluidic channel. Using e.g. green and red dyes to stain VSGs and antibodies, respectively, allows the individual tracking of both molecules simultaneously. Individual trajectories could verify that large VSG-antibody complexes

are more susceptible to the hydrodynamic forces and are transported towards the direction of the flow. Also, different types of VSGs with individual labels could be reconstituted into a SLB at the same time to mimic and study a mixed VSG surface coat that is present when antigenic variation occurs. For microscopic studies *in vivo*, static structures like the microtubule cytoskeleton or its associated proteins could be resolved in one color and linked to the dynamic information of surface VSGs or components of the outer and inner membrane leaflet (second color). Further, specific staining of structures like the flagella pocket or the flagellum enables to investigate VSG dynamics in relation to its surface localization. Two-color SMFM ca be a powerful tool to study versatile processes in living trypanosomes, especially when combining the technique with sophisticated 3D single-molecule microscopy.

4. Materials and Methods

4.1 Materials

4.1.1 Chemicals, buffers and working solutions

DNA analyses

TAE-buffer: 40 mM Tris-HCl, 40 mM acetic acid, 1 mM EDTA, pH 8.0
DNA loading buffer (10 x): 0.1 M EDTA (pH 8.0), 0.05% bromphenol blue (w/v), 0.05% xylene cyanol (w/v), 40% sucrose (w/v)
DNA-ladder: GeneRuler DNA ladder mix (100-10.000, Thermo Fisher Scientific, Waltham)

Protein analysis

2x-Laemmli sample buffer: 120 mM Tris-HCl, pH 6.8, 4% SDS (w/v), 20% glycerol (v/v), 0.004% bromphenol blue (w/v), 2% β-mercaptoethanol (v/v)
Laemmli running buffer: 25 mM Tris, 192 mM glycerol, 0.1% SDS (w/v)
Stacking gel buffer: 0.5 M TRIS-HCl (pH 6.8), 0.4% SDS (w/v)
Stacking gel: 1 mL acrylamid/bis-acrylamide 30:0.8, 1.8 ml stacking gel buffer, 4.5 mL mpH_2O, 40 μl 10% APS (w/v), 10 μl TEMED
Resolving gel buffer: 1.5 M TRIS-HCl (pH 6.8), 0.4% SDS (w/v)
Resolving gel, 12.5%: 1 mL acrylamid/bis-acrylamide 30:0.8, 1.5 ml resolving gel buffer, 2.5 mL mpH_2O, 30 μl 10% APS (w/v), 10 μl TEMED
Coomassie solution: 10% 2-propanol (w/v), 5% acetic acid (v/v), 0.05% Coomassie R-250 (w/v)
Destaining solution: 10% 2-propanol (w/v), 5% acetic acid (v/v)
Phosphate buffered saline, PBS: 10 mM Na_2HPO_4, 1.7 mM KH_2PO_4, 137 mM NaCl, 2.7 mM KCl, pH 7.4

T. brucei cultivation media

HMI-9 medium for *T. brucei* standard cultivation[170]: For 1 l medium: 17.66 g Iscove's modified Dulbecco's Medium (IMDM), 3.024 g $NaHCO_3$, 136 mg hypoxanthin, 82.2 mg bathocuproinsulfonat, 14 μl β-mercaptoethanol, 39 mg thymidine, 100.000 U penicillin, 100 mg streptomycin, 182 mg cysteine, 10% fetal calf serum (v/v, Sigma Aldrich)
HMI-9 medium for *T. brucei* high density cultivation: Standard HMI-9 medium with 10% fetal calf serum (v/v, Gibco)
Trypanosoma dilution buffer, TDB: 20 mM Na_2HPO_4, 2 mM NaH_2PO_4 (pH 7.7), 20 mM glucose, 5 mM KCl, 80 mM NaCl, 1 mM $MgSO_4$, pH 7.6 (sterile filtered, 0.2 μm pore size)
2 x freezing mix: 80% (v/v) HMI-9 medium, 20% (v/v) glycerol, sterile filtered (0.2 μm

pore size)

E. coli cultivation

LB-medium, 1 l: 10 g Bacto-Tryptone, 5 g yeast extract, 10 g NaCl, pH 7.4, ampicillin (100 μg/ml)
LB-agar plates: 1.5% agar in LB-medium (w/v), ampicillin (100 μg/ml)

Chemicals

All chemicals were purchased from Carl Roth, Applichem or Sigma-Aldrich if not other stated in the text.

Hydrogel components

Name	Providers
Poly(allyl glycidyl ether-*co*-glycidyl (P(AGE-*co*-G))), 11% substituted, 3.7 kDa	Simone Stichler (AG Groll), Würzburg
Hyaluronic acid, thiol modified (HA-SH), 54% substituted, 24 kDa	Simone Stichler
8-arm PEG-Norbornene (20 kDa, tripentaerythritol core)	Sigma-Aldrich (St. Louis)
linear PEG-dithiol (1 kDa)	Sigma-Aldrich
8-arm PEG-Vinylsulfone (10 kDa,tripentaerythritol core)	Sigma-Aldrich
Photoinitiator Irgacure-2959	Sigma-Aldrich
UVL hand lamp (VL-4LC)	Hartenstein, (Würzburg)

HPLC solutions

Solvent A, equilibration solvent : mpH_2O, 0.1% TFA (v/v)
Solvent B, eluent: 90 % Isopropanol, 10% mpH_2O, 0.1% TFA (v/v/v)
Solvent C, column storage solvent: 50% Acetonitril, 50% mpH_2O (v/v)

Fluorescent dyes

Reactive fluorescent dyes: ATTO-488 NHS-ester (ATTO-TEC),
ATTO-647N NHS-ester (ATTO-TEC)

staining solution: PBS, sodium-bicarbonate, 0.5% sodium-deoxycholate (w/v) pH 8.3

4.1.2 Kits and enzymes

Name	Providers
Amaxa Basic Parasite Nucleofector Kit1	Lonza (Basel)
CloneJET PCR Cloning Kit	Thermo Fisher Scientific
NucleoBond PC 100	Macherey-Nagel (Düren)
NucleoSpin Gel and PCR clean-up Kit	Macherey-Nagel
Sephadex G-25 PD-10 desalting column	GE Healthcare

Enzymes: Phusion High-Fidelity DNA Polymerase (Thermo Fisher Scientific), T4-DNA Ligase (Thermo Fisher Scientific)

4.1.3 Organisms

Bacterial strains

Escherichia coli (Top 10) genotype: F-mcrA Δ(mrr-hsdRMS-mcrBC) θ80lacZΔM15 ΔlacX74 recA1 araD139 Δ(araleu)7697galU galK rpsL(StrR) endA1 nupG

T. brucei strains

Wildtype strains:
Strain Lister 427: Molteno Insitut Trypanozoon Antigen Typ 1.1 and 1.6 (expressing VSGs referred to as VSG M1.1 and M1.6, respectively), blood stream form (BSF).
Parental strains for the generation of transgenic cell lines:
The parental MITat 1.2 13-90 cell line is based on monomorphic wildtype MITat1.2 BSF trypanosomes. The cells were genetically modified to constitutively express a T7 RNA polymerase and a tetracycline repressor ([117]) which facilitates an inducible control of T7 promotor-regulated gene expression. The cells were cultivated in standard HMI-9 medium containing 5 μg ml^{-1} hygromycin and 2.5 μg ml^{-1} neomycin (G-418).
Transgenic strains:
MITat 1.6 N-glycosylation deficient mutant: The cell line is based on parental MITat 1.2 13-90 trypanosomes. Expressed VSG M1.6 was genetically modified to be N-glycoylation deficient. Antibiotics used for selection: 30 μg ml^{-1} neomycin, 5 μg ml^{-1} hygromycin and 20 μg ml^{-1} blasticidin.
T. brucei Kinesin-MORN: The cell line is based on parental MITat 1.2 13-90 trypanosomes. Expresses a fusion protein located to the axonemal structure inside the

flagellum. Standard antibiotics for the parental cell line and additionally 0.1 μg ml^{-1} puromycin used for selection.
T. brucei HASP-eYFP: The cell line is based on parental MITat 1.2 13-90 trypanosomes. Expresses a dual-acylated eYFP that integrates into the cytosolic side of the plasma membrane. antibiotics for the parental cell line and additionally 2.5 μg ml^{-1} phleomycin used for selection.

4.1.4 Equipment

Cell culture

Name	Providers
Airstream Class II BSC	Esco global (Hoyland)
Amaxa NucleofectorTM 2b Device	Lonza
CO_2 Incubator	Binder (Tuttlingen)
Neubauer chamber	Marienfeld (Lauda-Königshofen)

Centrifuges and shaker

Name	Providers
Centrifuge 6-16 K, rotors: 12169/12170	SIGMA Laborzentrifugen (Osterode)
Centrifuge Z 216 MK, rotor: 220.87	HERMLE Labortechnik (Wehingen)
Centrifuge 1-14K	SIGMA Laborzentrifugen
Ultracentrifuge L8-70M, rotor: SW 55 TI	Beckman (Indianapolis)
Shaker TS-100C	BioSan (Riga)
Shaker celltron	INFORS HT (Bottmingen)

Sonicator

Elmasonic P30H (320 W, Elma, Singen), Bandelin Sonorex RK (80/320 W, Bandelin, Berlin)

DNA and protein analysis

Name	Providers
Odyssey Infrared Imaging System	LI-COR Bioscience (Lincoln)
Tecan Infinite M200 NanoQuant	Tecan Group (Männerdorf)
T-100 Thermal cycler	Bio-Rad Laboratories (Munich)

HPLC Ultimate 3000 and Freeze dryer

Equipment (DIONEX Softron, Germering): Pump HPG-3400SD, Photometer VWD-3400 RS, Column compartment TCC-3000SD, Solvent Rack SRD-3400, Manual sample injector (1 mL), Colomn PerfectSil 300 C4 (5 μm particle size, 250 x 10 mm)
lyophilization device (CHRIST, Osterode): freezer dryer: ALPHA 2-4 LD, rotary evaporator: AVC 2-25 CD, ILMVAC pump P4Z (Fisher Scientific)

4.1.5 Lipid work

Name	Providers
MicroThrough X-LB (Langmuir-blodgett through)	Kibron Inc. (Helsinki)
Hamilton Syringe	Sigma-Aldrich
1-stearoyl-2-oleoyl-sn-glycero-3-phosphocholine (SOPC)	Avanti Polar Lipids (Alabaster)
1,2-dioleoyl-sn-glycero-3-phosphoethanolamine (DOPE),	
ATTO 488 labeled	ATTO-TEC (Siegen)
Trichlormethan (Chloroform)	Sigma-Aldrich
Phosphate standard solution 0-65 nM	Sigma-Aldrich
color solution:	
Ammonium molybdate	Merck (Darmstadt)
L-ascorbic acid	Sigma-Aldrich

vesicle buffer: 20 mM Tris-HCl, pH 7,6, 50 mM NaCl, 0.5mM $CaCl_2$

Software

Name	Providers
Adobe Illustrator Creative Suite 6	Adobe Systems Incorporated (San Jose)
CLC Main Workbench 6	CLC bio (Venlo)
ImageJ 64	National Institute of Health
Microsoft Office	Microsoft (Redmon)
Prism 5.0	GraphPad Software (La Jolla)
Matlab R2013-17	The MathWorks Inc (Natick)
Cobolt Monitor^{TM}	Cobolt (Solna)
μManager 1.4	Micro-Manager
Live Acquisition	Till Photonics (Gräfeling)
Offline Analysis	Till Photonics

4.1.6 Microscopes

Fluorescence microscope

Name	Provider
Leica DMI 6000B	Leica (Wetzlar)
Leica Control Unit super z, Leica	
Leica CTR 6500 HS, Leica	
Incubator, Heating Unit 2000,	
TempController, CO_2 Controller	Pecon (Erbach)

FRAP Microscope Setup

Name	Provider
iMIC (inverted wide-field microscope)	Till photonics
Yanus digital scan head	Till photonics
Cobolt Blues, 473 nm	Cobolt Inc.
Polychrome V monochromator	Till Photonics
CCD camera (Sensicam)	PCO (Kelheim)
Nikon 60 x objective lens (NA 1.45)	Nikon (Tokio)

Single-molecule microscope set-up

Name	Provider
Leica DMI 6000B [1]	Leica
HCX PL APO 100x objective lens (NA 1.47 OIL) [2]	Leica
Cobolt Fandango 515 nm, 50 mW [3]	Cobolt Inc.
Cobolt MLD 640 nm, 100 mW [4]	Cobolt Inc.
AOTFnc-400.650-TN & Multi-Digal Synthesizer [5]	AAOpto Electronics (Wallenhorst)
AOTF control unit	custom made
VCM-D1 (shutter) [6]	UniBiltz (Rochester)
OptoSplit II [7]	Cairin (Faversham)
iXon3 DU-897 Em-CCD camera [8]	Andor (Belfast)
HM81-50 (function generator)	Rohde & Schwarz (Munich)
HM010-22 (oscilloscope)	HAMEG (Frankfurt)
PM100D (photometer)	Thorlaps (Newton)
emission & excitation filter:	
F37-551, F76-635	Semrock (Rochester)
F48-635, z514-633	Chroma (Rockingham)

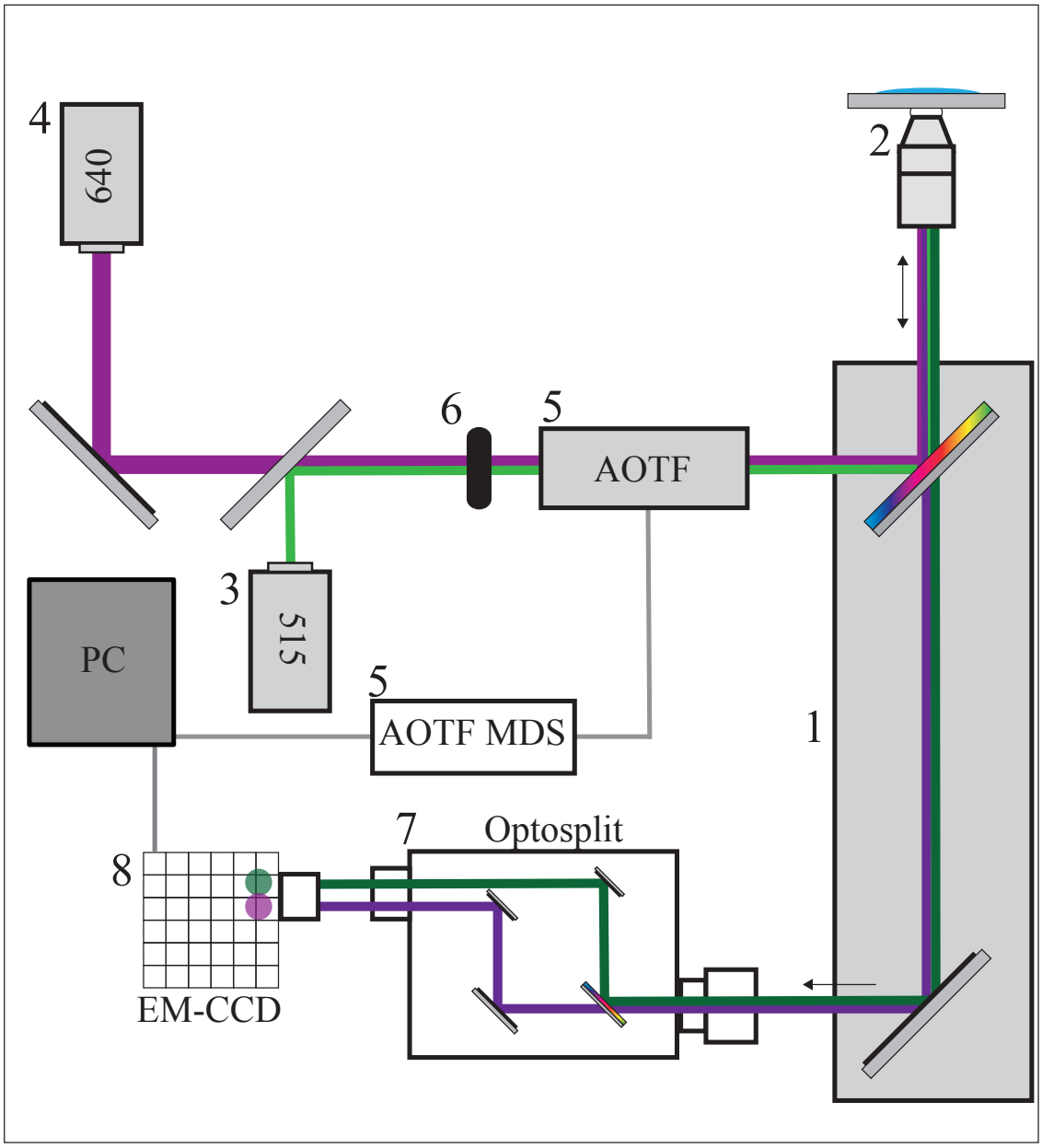

Figure 4.1: Scheme of the single-molecule fluorescence microscope setup. 1) Leica DMI 6000B, 2) CX PL APO 100x objective lens (NA 1.47 OIL), 3) Cobolt Fandango 515 nm, 50 mW, 4) Cobolt MLD 640 nm, 100 mW, 5) AOTFnc-400.650-TN & Multi-Digal Synthesizer, 6) VCM-D1 (shutter), 7) OptoSplit II, 8) iXon3 DU-897 Em-CCD camera.

4.2 Methods

4.2.1 Working with *T. brucei*

Standard cultivation

Bloodstream form *T. brucei* cells were cultivated in HMI-9 medium ([170]), supplemented with 10% (v/v) fetal bovine serum at 37°C and 5% CO_2. Maintenance of a stable population was achieved by regular determination of the cell concentration and dilution with fresh, pre-warmed HMI-9. The Cell concentration was limited to 8 x 10^5 cells ml^{-1} at all times to ensure exponential growth of the population. Transgenic cell lines were cultivated with HMI-9 medium containing specific antibiotics.

Generation of cryo-stabilates

Cryo-preservation was applied for long-time storage of *T. brucei* populations. For each stabilate, 4 x 10^6 cells were harvested from a liquid culture via centrifugation at 1400 x g for 10 min at 4 °C, resuspended in 500 μl ice-cold HMI-9 and transferred to cryo tubes. The cells were then chilled on ice for 5 min to minimize their endocytosis activity. 500 μl of ice-cold glycerol containing 2x freezing mix was then added to each stabilate and they were stored immediately at -80°C. For long-time storage, the cryo-stabilates were transferred to -180°C.
For the recultivation of cryo preserved cells, stabilates were thawed in a 37°C warm water bath and quickly diluted in 10 ml ice-cold HMI-9 medium. After centrifugation (1400 x g, 10 min, 4 °C), the supernatant was discarded and the cell pellet was resuspended in 10 ml pre-warmed HMI-9 medium. After one hour of incubation, the cells were counted, diluted appropriately and antibiotics were added to the culture.

High-density cultivation

Large amounts of cells are required for the extraction and subsequent purification of the membrane form of VSG (mfVSG). For that purpose, *T. brucei* cells were cultivated in HMI-9 medium that contained 10% (v/v) fetal calf serum purchased from Gibco (Thermo Fisher Scientific) that facilities high cell densities in liquid cultures. The cells were grown under standard conditions until a density of 8 x 10^5 cells ml^{-1} was reached. The cells were then diluted in 10 x the volume of the initial culture and transferred to 2 l conical flasks, whereby the culture volume did not exceed 20% of flasks total volume. Cell proliferation continued on a rotary shaker (60-80 rpm) up to a density of 1.5-3 x 10^6 cells ml^{-1}, before the cells were prepared for the extraction of mfVSG. The total number of harvested trypanosomes did not exceed 5 x10^9 cells as this represents the maximal loading capacity of

the HPLC-column (4.2.6).

Generation of transgenic cell lines

Bloodstream form *T. brucei* Lister 427 13-90 cells were used as the parental cell line for the generation of new transgenic cultures. 3 x 10^7 cells were harvested by centrifugation at 1400 x g for 10 min at RT and carefully resuspended in 100 μl transfection solution of the Amaxa Basic Parasite Nucleofector Kit1. 10 μg linearized plasmid DNA was added and the mixture was transferred to transfection cuvettes. Cell electroporation was performed using a commercial electroporation device (Amaxa Basic Parasite Nucleofector, program X-001). Transfected cells were then immediately transferred to 30 ml pre-warmed HMI-9 followed by a serial dilution (1:10, 1:100 and 1:1000 (v/v), contained parental antibiotics) for the establishment of monoclonal cell populations. Each dilution was plated on a 24-well plate, incubated for 8 h and then supplemented with antibiotics for the selection of transgenic cells. The well plates were examined regularly for upcoming monoclonal populations. Transgenic cells were then transferred to cell culture flasks for the establishment of stable cultures (usually after 4-6 days post-transfection).

Generation of *T. brucei* kinesin-MORN

Super-resolution imaging was conducted in living trypanosomes in order to determine the immobilization efficiency of different hydrogels (see section 4.2.5). Since the flagellar beat is at the origin of trypanosome motion, cells were imaged that expressed a fluorescent fusion-protein located to the axoneme inside the flagellum. A transgenic cell line was used, that was generated by Ines Subota and expressed an eYFP tagged kinesin-MORN. In brief, the parental cell line was genetically modified to constitutively express kinesin-MORN (membrane occupation and recognition nexus, gene accession number: Tb927.10.14570) C-terminally labeled with eYFP [111]. The expression system was based on the eYFP containing plasmid 3329 [171, 172] and linearized prior to stable integration into the endogenous locus via transfection. Selection for transgenic cells was conducted using standard antibiotics for the parental cell line and additionally 0.1 μg ml^{-1} puromycin.

Generation of *T. brucei* HASP-eYFP

The organization of the inner plasma membrane leaflet was studied using an eYFP fusion protein. In brief, the parental cell line was genetically modified to express eYFP N-terminally tagged with the dual acylation sequence from the Leishmania HASPB protein (Accession number: LmjF.23.1060). The amino acid sequence of the dual acylation side

(MGSSCTKDSAKEPQKSAD) gets post-transcriptionally myristoylated and palmitoylated at positions two and four, respectively [151]. The HASP::eYFP trans-gene sequence was amplified via PCR and then cloned into the tetracycline inducible vector pLEW100v5 [117] using the restriction enzymes HindIII and XhoI (4.2.2). Stable integration of the construct into the genome was performed via transfection (section 4.2.1) and monoclonal cells were selected for successful integration using antibiotics for the parental cell line and additionally 2.5 μg ml^{-1} phleomycin. Super-resolution imaging was performed for the transgenic cells without the addition of tetracycline, which ensured low levels of HASP::eYFP expression and facilitated the detection of single-molecules.

4.2.2 Working with DNA

Standard molecular biology methods were used for generation of the HASP::eYFP sequence. This included the amplification from circular plasmid DNA and the ligation into the target vector pLEW100v5 (pLEW100v5 was a gift from George Cross (Addgene plasmid (24011)).

Generation of pLEW100v5HASP::eYFP

The HASP::eYFP DNA sequence was generated via 2-step PCR and then integrated into the plasmid vector pLEW82ΔOP ([173]) as an interim stage. The eYFP sequence was amplified from the plasmid P2675-eYFP (Nicola Jones). The oligonucleotide eYFP$_{forward}$ contained a 5' overhang that encodes for parts of the HASP sequence (see table 4.1, bold letters). A short sequence of the target plasmid (pLEW82deltaOp-PDEB1, Jaming Jung) was also amplified using an oligonuleotide (pLEW82$_{reverse}$) that contained a 3' overhang partially identical to the HASP-sequence of the eYFP PCR product. The sequence identity of the amplified products was used in a second PCR for the amplification of the complete HASP::eYFP sequence (2-step PCR). The product was then digested (XhoI and HindIII) and ligated into the Vector pLEW82. For single-molecule experiments, the HASP::eYFP DNA sequence was further ligated into the tetracycline ineducable vector pLEW100v5 using the XhoI and HindIII restriction sites.

In general, DNA-fragments were amplified from plasmid DNA in a 25 μl standard assay using 1 unit of the polymerase (Phusion High-Fidelity DNA Polymerase) in 1x GC or HF-buffer containing 100 μM oligonucleotides, 10 ng plasmid DNA and 0.2 μM forward and reverse primers, respectively. The annealing temperature of the reaction depended on the composition of the primers.

Table 4.1: Oligonucleotides used for the generation and amplification of the HASP::eYFP trans gene product. Bold letters indicat added overhangs of the oligonucleotides.

Name	Sequence (5'-3')
$eYFP_{forward}$	**AAGACTCTGCCAAGGAACCTCAGAAAAGCGCTGAC**-ATGGTGAGCAAGGGCGAGGAGCTGTTCAC
$eYFP_{reverse}$	ATGGATCCTTACTTGTACAGCTCGTCCAT
$pLEW82_{forward}$	AGGAATTCGAGCTCATATAGT
$pLEW82_{reverse}$	**CCTTGGCAGAGTCTTTAGTGCAGCTGGAGCCCAT**-AAGCTTGTGAATTTTACTTTTTGGTGTAAT

Agarose gel electrophoresis

DNA-fragments of variable length were analyzed using 0.8% - 1.5% (w/v) agarose gels in TAE-buffer. The DNA was mixed with 6 x DNA loading buffer and analyzed in appropriate gel-electrophoresis chambers together with a DNA-ladder at 100 V. The DNA was then stained for 10 min in a 3 μg ml^{-1} ethidium bromide solution and visualized using UVA light. DNA-fragments were extracted from agarose gels using commercial kits (NucleoSpin Gel and PCR clean-up kit) following the manufacturers' instructions.

Isolation of plasmid DNA

Expression of ectopic plasmid DNA in *E. coli* was verified by analytical digestion. Commercial plasmid extraction kits were used following the manufacturers' instructions for the purification of plasmid DNA (NucleoBond PC 100, NucleoSpin Gel and PCR clean-up Kit). DNA concentration and purity were determined photometrically at A_{260} and A_{280} and DNA was stored at - 20 °C.

Restriction enzyme digestion and ligation of DNA

PCR-fragments and plasmid DNA were digested prior to ligation or for analytical purposes following the manufacturers' instructions. The T4-DNA ligase was used for the ligation of DNA-fragments into target vectors using a commercial kit (CloneJET PCR Cloning Kit).

4.2.3 Working with *E. coli*

Transformation of competent *E. coli*

Chemically competent *E. coli* cells were used for the amplification of circular plasmid-DNA containing the HASP::eYFP sequence. The cells were thawed on ice and incubated with 20-50 ng of a ligation product for 30 min. A heat shock was then performed at 42 °C

for 45 s. Transformed cells rested for another 20 min on ice before they were plated on LB agar plates and incubated over night at 37°C. The expression and purification of ectopic plasmid DNA was performed as described in section 4.2.2.

4.2.4 Biochemical techniques

Discontinous SDS-polyacrylamid gel electrophoresis

SDS-polyacrylamid gel electrophoresis was conducted to verify the successful extraction and purification of membrane form VSG from living trypanosomes (section 4.2.6). Collected HPLC-fractions were dissolved in 1 x Laemmli buffer and heated to 95 °C for 5 min to denaturize the proteins. The samples were then analyzed in appropriate chambers using 12.5% acrylamid/bisacylamid gels at 100-130 mV. The gels were subsequently stained in Coomassie solution for 30 min followed by destaining (Destaining solution) over night to visualize protein bands.

Isolation of *T. brucei* whole cell protein extracts

The amount of reconstituted VSG in lipid bilayer (section **??**) was compared to a dilution series of trypanosome whole-cell extracts using an immuno-histochemical approach. This was conducted to quantify the lateral protein density relative to cell surface equivalents. Whole cell *T. brucei* protein extracts were isolated from living trypanosomes. $3*10^7$ cells were harvested via centrifugation (1400 x g for 10 min at RT) and washed 2 x with 1 ml TDB (800 x g, 90s,RT). The cells were carefully resuspended in 600 μl TDB and aliquots were prepared from the cell solution. The exact amount of cells was then determined using a Neubauer-chamber (4.2 x 10^5 cells in 50 μl TDB). 50 μl 2 x Laemmli buffer were then each added and the samples were heated to 95 °C for 5 min and finally stored at - 20 °C until used.

Western dot-blot

Reconstituted VSG samples and whole cell protein extracts were analyzed immuno-histochemically on a western dot-blot. For that purpose, a nitrocellulose membrane was incubated in PBS for 5 min and subsequently dried between two layers of whatman paper. The membrane was then deposited in a custom made device. Triplicates of whole cell protein extracts (4.2.4) were then dotted in a six step linear dilution series onto the membrane (equals 1.3 x 10^3-8.4 x 10^4 cells). The pure or diluted VSG proteoliposome samples (before and after incubation) were pipetted next to the dilution series and the membrane was dried for 15 min at RT. VSG was then detected on the nictrocellulose membrane using specific primary and secondary antibodies. In brief, the membrane was

incubated for 1 h in 50 ml PBS containing 5% (w/v) milk powder to block unspecific binding sites. The primary antibody (anti VSG M1.6, second bleed, polyclonal, rabbit, Mark Carrington) was diluted 1:1000 in PBS (1% milk powder, 0.1% Tween-20). 5 ml were then added to the membrane and incubated for 1 h at RT. The membrane was washed 3 x for 5 min with each 10 ml PBS (0.2% Tween-20). Next, the secondary antibody (IR-Dye 800 anti-rabbit (LI-COR), polyclonal, goat) was diluted 1:10000 ((1% milk powder, 0.1% Tween-20) and 5 ml were added to the membrane, followed by 1 h incubation at RT in the dark. The membrane was then washed 3 x with each 10 ml PBS (0.2% Tween-20) and 2 x with 10 ml PBS. The membrane was then finally dried between two whatman paper for 20 min. The antibody complexes were detected using infrared fluorescence (LI-COR ODYSSEY IR Scanner (LI-COR, Lincoln)). The comparison of the dilution series and pre- and postincubation samples from reconstituted samples allowed then the quantification of VSG in the artificial lipid bilayers.

4.2.5 Preparation of trypanosomes for microscopy

Labeling of surface VSG in living cells

NHS-ester coupled fluorescent dyes were used to label the VSG coat of living trypanosomes. These dyes react with primary amines of VSGs under mild alkaline conditions and form covalent bonds. For single-molecule studies of VSG dynamics, irreversible bleaching of VSG bound dyes had to be considered when imaging the VSG coat. To increase the number of VSG localizations in the imaging process, the cells were immobilized in hydrogels that contained reactive ATTO647N-NHS ester. These dyes diffused through the hydrogel and reacted with surface VSG throughout the imaging procedure. In brief, 1 x 10^7 cells were centrifuged at 800 x g for 12 min at 4 °C and washed 3 x in 1 ml TDB (800 x g for 90 s at 4 °C). The cells were then resuspended in 10μl TDB and kept on ice for 5 min. 1 μl of the cell solution was then mixed with the hydrogel precursor solutions (4.2.5) and ATTO647N-NHS ester was added to a concentration of 0.5 nM. After immobilization, single-molecule imaging of VSG dynamics was conducted. Adding free, reactive dye to the hydrogel facilitated the permanent formation of covalent VSG-dye bonds on the cell surface while imaging. This allowed the repetitive illumination of an immobilized cell and the generation of a multitude of VSG trajectories on the cell surface. For applications that required the labeling of the majority of the VSG surface coat, 1 x 10^7 cells were centrifuged at 800 x g for 12 min at 4 °C and washed 3 x in 1 ml TDB (800 x g for 90 s at 4 °C). The cells were then resuspended in 100 μl TDB pH 8.3. The cell solution was kept on ice for 10 min in the dark and 1 μM ATTO-488 was added. After 10 min of incubation, the cells were washed 3-4 times with 1 ml ice cold TDB, which efficiently removed unbound dyes from the solution. The cells were kept on ice for a maximum of 1 h before they were used for microscopy.

Hydrogel formation

Three different types of hydrogels were used for the immobilization of living trypanosomes. The formation of two gel systems was based on the nucleophilic addition of reactive thiol-groups to unsaturated carbonyl containing components. The third gel reacted via Michael-addition chemistry.

The first hydrogel consisted of the precursor solutions poly(allyl glycidyl ether-*co*-glycidyl, P(AGE-*co*-G)) substituted with allyl groups to a degree of 11% and thiol-functionalized hyaluronic acid (HA-SH) with 53% thiol substituted side groups and was synthesized by Simone Stichler ([109, 174]). For the formation of the hydrogels both polymers were separately dissolved in TDB for 1 h at RT in the dark while gently agitating the solutions. P(AGE-*co*-G)) and HA-SH were then mixed at equimolar ratios of functional groups (allyl:SH) to total polymer concentrations larger than the final desired concentrations (10% (w/v), 15% (w/v) and 20% (w/v)) in order to consider further dilution steps (e.g., the addition of the photointiator, trypanosomes and fluorescent dyes). The mixtures were then agitated for 30 min in the dark at 37 °C and the pH was adjusted to 7-7.5 using 1 M NaOH. 0.05% (w/v) photoinitiator (Irgacure-2959, I2959) was then added and solution was kept on ice in the dark for a maximum of 2 h. Longer storage times can lead to polymerization of the hydrogel precursor solution without UV-illumination. For the immobilization of cells, pre-washed living or chemically fixed trypanosomes (4.2.5) were carefully resuspended in appropriate volumes of the hydrogel (usually 10 μl) and 3-5% of the cell/hydrogel mixture was pipetted between two cleaned glass cover slips. The cover slips were then mounted in a sample chamber and centrifuged at 100 x g for 1 min at 4 °C. The chambers were then illuminated with a UV lamp (λ = 365) at a distance of 5 cm for 5 min at 4 °C with a mean intensity of 1 mW cm$^{(-2)}$ for cross-linking of polymer precursors.

For the formation of the second hydrogel, the precursor solutions 8-arm poly(ethylene glycol)-norbornene (20 kDa, PEG-NB, Sigma-Aldrich) and linear PEG-dithiol (1 kDa, PEG-dT, Sigma-Aldrich) were separately dissolved in TDB and gently agitated in the dark for 30 min at RT. Next, the solutions were mixed at equimolar ratios of functional groups (norbornene:thiol) to total polymer concentrations larger than the final desired concentrations (10% (w/v)) to consider further dilution steps. The mixture was then gently agitated for 30 min at 37 °C to ensure proper mixing and 0.025% I2959 was added. Immobilization of cells was then performed as described for P(AGE-*co*-G))/HA-SH hydrogels with an UV-exposure time of 2 min.

The third hydrogel tested was cross-linked based on Michael-addition chemistry and consisted of 8-arm PEG-Vinylsulfone (PEG-VS) and thiol-functionalized hyaluronic acid (HA-SH) with 53% thiol substituted side groups. Thiol and vinylsulfone groups readily reacted upon mixing and formed cross-linked hydrogels without the addition of a photoinitiator and UV-illumination. The reaction kinetics of the process depended critically on the

pH-value of the buffer solution and gel formation was fast under slightly alkaline conditions ($\sim$ 1 min). For the immobilization of trypanosomes, 10% (w/v) PEG-VS/HA-SH hydrogels (4 °C, pH > 8.3) were mixed with appropriate numbers of ice-cold, prewashed trypanosomes. The mixture was pipetted between two cleaned glass cover slips. The cover slips were then mounted in a sample chamber and centrifuged at 400 x g for 1 min at 4 °C.

Cell viability assay

Propidium iodide (PI) was used as a live/dead fluorescence marker to monitor the viability of trypanosomes immobilized in hydrogels over time. PI is a membrane-impermeant green dye that is excluded from the interior of viable cells but can bind to intracellular DNA upon loss of cell membrane integrity. This leads to large stokes-shift of the PI emission and the dye becomes highly fluorescent with an excitation maximum of 535 nm. 5 μg ml^{-1} PI were added to the unpolymerized hydrogel solutions that already contained I2959 and pre-washed living or fixed trypanosomes (VSG surface labeled (4.2.5)). The gels were then cross-linked as described before (4.2.5). Intracellular PI-fluorescence was monitored using an inverted wide-field microscope with appropriate excitation wavelengths and emission filters of 530-560 nm and 572-648 nm, respectively. The cell viability was recorded over 60 min at RT (PEG-NB/PEG-dT hydrogels) or 37 °C ((HA-SH/P(AGE-*co*-G) hydrogels). As a control, trypanosomes were prepared equally but in buffer solution (TDB) instead of hydrogel solution. In order to categorize immobilized trypanosomes as living or dead, a threshold of intracellular PI-fluorescence was set upon which cell viability was excluded. This threshold was derived from the intracellular fluorescence of chemically fixed cells. Trypanosomes were then counted in the images by eye and evaluated to determine the cell viability.

Chemical cell fixation

As a negative control for the cell viability, trypanosomes were chemically fixed and further immobilized in hydrogels (4.2.5). The procedure partially disrupts the membrane integrity and hence, facilitates the binding of PI to intracellular DNA. In brief, 1 x 10^7 cells were centrifuged and washed with TDB as described previously. The cells were then chemically fixed in TDB containing 2% paraformaldehyde (w/v) for 15 min at RT and washed three times with TDB. Subsequently, 0.1% Triton-X 100 were added to the solution to partially disrupt the cell membrane. The solution was incubated for 5 min at RT, followed by three washing steps with TDB. Finally, the chemically fixed cells were immobilized in P(AGE-*co*-G))/HA-SH hydrogels.

4.2.6 Extraction and purification of *T. brucei* membrane form VSG

Acidic extraction of membrane form VSG

The membrane form VSGs were extracted from living trypanosomes using the trifluoroacetic acid (TFA) assay published by Clarke et al. [175]. The procedure required strict cooling of the cells during centrifugation and protein extraction to inhibit cellular protease activities and cleavage of the VSG GPI-anchor. A maximum of 5 x 10^9 cells were prepared for the purification, since this represents the loading capacity of the HPLC-column (PerfectSil300 C4, 5μm particle size, 250 x 10mm). The cells were harvested by centrifugation either in 50 ml falcon tubes at 800 x g for 10 min at 4 °C or in 800 ml tubes at 1000 x g for 30 min at 4 °C. The supernatant was then discarded and the cell pellet was carefully resuspended in a total volume of 50 ml ice-cold TDB, followed by three washing steps with 50 ml ice-cold TDB at 800 x g for 10 min at 4 °C. For the extraction of all membrane proteins, the cell pellet was resuspended in 2 ml ice-cold PBS containing 0.1% TFA (pH 2-3) and incubated for 5 min on ice. The TFA solution solubilizes membrane proteins and its low pH-value impedes protease activities that would readily cleave of the GPI-anchor of the VSGs. Solubilized, VSG containing fractions were then separated from cell fragments by centrifugation at 6000 x g for 5 min at 4 °C and kept on ice. The pelleted fragments were again resuspended in 750 μl ice-cold PBS 0.1% TFA and centrifuged at 9000 x g for 5 min at 4 °C. The VSG containing supernatant was pooled (kept on ice) and the pellet was resuspended in 500 μl ice-cold PBS 0.1% TFA, followed by centrifugation at 9000 x g for 5 min at 4 °C. The collected supernatants were then pooled ($\sim$ 4 ml total volume) and centrifuged again to remove remaining cell fragments (9000 x g for 15 min at 4 °C). The membrane protein containing solution was then immediately injected in a pre-equilibrated HPLC column to purify the membrane form of VSGs.

High-performance liquid chromatography

The purification of membrane form VSGs from *T. brucei* protein extracts (4.2.6) were conducted via high-performance liquid chromatography (HPLC). 1 ml of the protein solutions were injected to a pre-equilibrated column (mpH_2O, 0.1% TFA), followed by purging of the injection loop of the HPLC device using 4 ml solvent A. The procedure was repeated until the entire extracted protein solutions were applied to the column. The membrane form VSGs were then eluted from the column using the solvent gradient shown in table (4.2). The elution times depended on VSG type applied but were typically found around 40-50 min, representing 40-50% (v/v) solvent B (90% Isopropanol, 10% mpH_2O, 0.1% TFA). The HPLC-device contained a photometer for the detection of eluted proteins using a wavelength of 280 nm. Positive, protein containing fractions were then collected in glass vials and stored on ice until the elution program was finished (50 μl of each fraction were

Table 4.2: HPLC solvent gradient. Solvent A (equilibration solvent, mpH_2O, 0.1 % TFA), Solvent B (eluent, 90 % Isopropanol, 10 % mpH_2O, 0.1 % TFA), Solvent C (column storage solvent, 50 % Acetonitril, 50 % mpH_2O)

Time [min]	Flow [ml/min]	Solvent A [vol%]	Solvent B [vol%]	Solvent C [vol%]
0-5	4	100	0	0
5-15	4	67	33	0
15-25	4	67	33	0
25-65	4	42	58	0
65-70	2.5	10	90	0
70-80	2.5	10	90	0
08-100	4	100	0	0
100-120	4	0	0	100

kept for a SDS-polyacrylamid gel electrophoresis). The solutions were then evaporated for 30 min in a rotary evaporator at 30 °C to quickly remove the majority of isopropanol in the solvent. Subsequently, they were frozen in liquid nitrogen and evaporated in a lyophilization device for 24 h at 0.001 bar to remove trace amounts of solvents. The lyophilization product was then stored at -20 °C until used. The collected fractions were analyzed using 12.5% SDS-polyacrylamid gels in order to identify the purified VSGs. Care must be taken since membrane form VSGs and their GPI-anchor deficient degradation products are almost similar with respect to their retention times on the HPLC-column and appearance on SDS-polyacrylamid gels. To verify the existence of the anchor, purified VSG fractions were further fluorescently labeled and their integration into preformed supported lipid bilayer was monitored.

Fluorescence labeling of purified VSGs

Purified VSGs were labeled either with ATTO-488 (VSG ATTO488) or ATTO-647N (VSG ATTO647N) using primary amine reactive N-hydroxysuccinimide ester (NHS-ester). Lyophilized protein powder was redissolved in 0.5-1 ml staining solution (PBS, 0.01 M sodium-bicarbonate, 0.5% sodium-deoxycholate (w/v), pH 8.3) and the protein concentration was determined photometrically. The molar extinction coefficients of the VSGs were derived by ProtParam algorithms based on mature protein sequences [176]. ATTO-488 and ATTO-647N were added to the protein solutions at a 3 x and 0.1 x molar excess, respectively. Covalent attachment of the dyes to the primary amines of the proteins was achieved by incubation at RT for 45 min in the dark. Protein-dye conjugates were then separated from unbound dye via size-exclusion chromatography following the manufacturers' instructions (PD-10, Sephadex G-25 gel filtration column). Separation of free dye was concomitant with buffer exchange to vesicle buffer (20 mM Tris-HCl, pH 7,6,

50 mM NaCl, 0.5mM $CaCl_2$) solution, that was required for the formation of supported lipid bilayers (4.2.7). The degree of labeling (DOL) was then calculated following the manufacturers' instructions and the solutions were aliquoted and stored at -20 °C until used.

4.2.7 Formation of supported lipid bilayers

Preparation of hydrophilic glass cover slips

Thickness corrected glass cover slips were cleaned and surface treated before they were used in microscopic studies. When used as solid supports for the formation of lipid bilayer they were cleaned by sequential sonication in acetone, ethanol and methanol for 15 min each, followed by excessive rinsing with fresh mpH_2O. Cover slips were then soaked in 1:1:5 (v/v/v) 30% ammonia : 30% hydrogen peroxide : mpH_2O for 30 min at 80 °C, washed again with fresh mpH_2O and stored under mpH_2O for maximum three days. For *In vivo* studies, cover slips were cleaned by sonication in 2% Hellmanex II solution for 15 min followed by multiple washing steps with fresh mpH_2O. The procedure was repeated once and the glass cover slips were then sonicated in fresh mpH_2O for 15 min and rinsed excessively with fresh mpH_2O. Cleaned glass cover slips were then stored for maximum three days in a water bath.

Formation of small unilamellar vesicles

Liquid SOPC lipid stock solutions (chloroform, stored at -20 °C) were prepared for a long time storage. For that purpose, they were equilibrated to RT and then aliquoted to glass vials using Hamilton syringes. The solutions were then dried under a stream of nitrogen gas to evaporate the solvent and finally stored at -80 °C until used.
Large multilamellar vesicles (LUV) were formed by rehydrating dried SOPC aliquots in vesicle buffer to a concentration of 1-2 mg ml^{-1}. The solutions were vortexed for 1 min and then gently agitated for another 30 min at RT. Disruption of LUV's to small unilamellar vesicles (SUV's) was achieved by sonication. The efficiency of SUV formation depended on the sonication power and time. Usually, 3-5 sonication steps of 15 min with a minimum power of 200 W were conducted. As a control, the turbidity of the solution was examined by eye - SUV solutions were formed from turbid LUV's when the solution appeared transparent. SUV solutions were then stored at 4 °C for a maximum of 7 days and sonicated for another 10 min before they were used.

Formation of supported lipid bilayer by vesicle fusion

Supported lipid bilayers were formed on hydrophilic glass cover slips via vesicle fusion. For that purpose, pre-cleaned glass cover slips were mounted in custom made microscopy chambers of different size (radius 0.5- 2 cm), washed thoroughly with sterile filtered vesicle buffer and finally covered with vesicle buffer. Depending on the size of the chamber, 20-100 μl SUV solution (1-2 mg ml^{-1}) were added to the buffer. The chambers were then incubated for 30-120 min in a 37 °C room in order to facilitate the fusion of SUV's to the hydrophilic glass. The samples were then washed thoroughly with vesicle buffer to remove non-adsorbed vesicles. Lipid bilayers were then used for the incorporation of fluorescently labeled VSGs or DOPE-488 lipids.

Incorporation of fluorescent VSGs and lipids into SLBs at low densities

1-5 μl of ATTO647N labeled VSGs (1-10 nM) were added to the supernatant of preformed SOPC SLBs and incubated for 1-10 min. Incorporation of single VSG ATTO647 molecules was monitored at the microscope until the desired density was reached. The membrane was then washed thoroughly with > 10 x supernatant volume with vesicle buffer. For the incorporation of fluorescent lipids, 10 μl of DOPE488 solution (0.1 μg ml^{-1} in chloroform) were dried under a stream of N2-gas and rehydrated in 150 μl vesicle buffer. 10 μl of the solution were then added to preformed SOPC SLBs and the integration of single DOPE488 molecules was monitored. The membranes were finally washed as described to remove non-integrated molecules from the supernatant.

Reconstitution of VSGs into proteoliposomes

Extracted and purified VSGs ATTO647 were reconstituted into proteoliposomes in order to measure the density depended VSG diffusion. VSG ATTO488 was used for ensemble FRAP measurements. For single-molecule studies unlabeled VSGs were reconstituted and single VSGs ATTO647N were finally integrated into preformed SLB/VSG layer from the supernatant at low densities in order to detect single flurescent spots. The method of reconstitution was based on the approach described by Hu *et al.* [74] and Erb *et al.* ([75]). In brief, SOPC-lipids and VSGs were mixed at a molar lipid-to-protein ratio of 40 in vesicle buffer containing 1% sodium deoxycholate (w/v). The mixture was then agitated in the dark for 30 min at 30 °C and subsequently at 37 °C for 90 min. The detergent was then removed from the solution by incubating two times with 100 mg SM-2 Biobeads for 60 min at 37 °C. The Biobeads were previously washed as described by Holloway [177]. Non-incorporated VSGs and trace amounts of sodium-deoxycholate were then separated from proteoliposomes in a four-step sucrose gradient (2 M, 1.2 M, 0.8 M and 0.4 M in

vesicle buffer) via ultracentrifugation at 120.000 x g for 18 h at 4 °C. The proteoliposome containing fractions (usually settled at the boundary layer between 2 M and 1.2 M surcrose) were determined photometrically at A_{280} or A_{488} and collected. The sucrose was then removed from the solutions via dialysis. The samples were dialysed three times for at least 8 h against 400 x volume vesicle buffer using a high molecular weight cut-off tube (1000 kDa). The proteoliposomes were then sonicated for 15 min and stored at 4 °C for a maximum of 7 days.

Determination of the lipid-to-protein ratio in proteoliposomes

The concentration of SOPC-lipids in proteoliposome samples was determined calorimetrically at A_{797} after the reaction of the organic phosphate with ammoniummolybdat. The procedure followed the protocol published by Bartlett [178] with modifications described by Anderson [179]. In brief, three aliquots (40-60 μl) of a proteoliposome solutions and defined amounts of a phosphate standard dilution (0-65 nmol phosphate were each pipetted into glass vials and dried at 100 °C in a laboratory oven. The glass vials were subsequently cooled to RT and 100 μl concentrated sulfuric acid were added. The mixtures were now incubated at 155 °C for 15 min in a laboratory oven, cooled to RT and supplemented with 50 μl 6% hydrogen peroxide. The solutions were again heated to 155 °C for 40 min in a laboratory oven and subsequently cooled to RT. 2 ml mpH_2O were then added. Finally, 800 μl of a coloring solution (6.25 mg ml^{-1}, 4.5 mg ml^{-1} L-ascorbic acid) were added and the samples were incubated for 15 min at 100 °C in a laboratory oven. Finally, the absorptions were determined at A_{797} in a photometer (Tecan Infinite M200) and the lipid concentration was then determined with the help of the phosphate standard curve. The amount of VSG in the proetoliposome solutions was determined photometrically at A_{280} and the lipid-to-protein ratio (lpr) was calculated as $lpr = M_{SOPC}/M_{VSG}$.

Langmuir-Blodgett transfer

Langmuir-Blodgett transfer was used to deposit SOPC monolayers on hydrophilic glass cover slips. 5 μl of a SOPC solution (2 mg ml^{-1}, in chloroform) were spread on the water sub-phase of a Langmuir film balance (Kibron). The lipid film was then compressed using Polytetrafluoroethylene (PTFE) barriers while recording the surface pressure as a function of the area (compression isothereme). Lipid monolayeres were then transferred to the solid support at a constant surface pressure of 32 mN m^{-1} and a vertical deposition rate of 1 mm min^{-1}. The covered glass covers slips were then mounted to PTFE enclosed microscopy chambers and immediately used for the formation of protein decorated lipid bilayers via proteoliposome vesicle fusion. The Fusion of proteoliposomes was analogous

to the fusion of SUV's (4.2.7).

Incorporation of VSGs in supported lipid bilayers at different concentrations

VSGs were reconstituted in supported lipid bilayers at different lateral protein densities. The technique is based on the formation of proteliposomes and their fusion to solid supported SOPC-monolayers (4.2.7). The lateral spacing of VSGs in the bilayer was adjusted by dilution of proteoliposomes with maximum protein density with defined amounts of protein-free SOPC vesicles before applying the solution to SOPC-monolayers. The samples were then incubated for 2 h at 37 °C and subsequently washed thoroughly with vesicle buffer. For single-molecule experiments the samples were further incubated with ∼0.1 pmol ATTO-647N labeled VSGs for 5-15 min at 37°C, followed by another washing step.

Relative quantification of VSGs in supported lipid bilayers

Reconstituted VSG samples were compared to a dilution series of defined trypanosome whole-cell extracts to quantify their lateral protein density relative to cell surface equivalents. The procedure involved an immuno-histochemical detection of VSGs (4.2.4). Triplicates of pure or diluted proteoliposome samples (50 μl) were collected before they were applied to SOPC-monolayers and 2 h after incubation at 37 °C. The samples were then spotted onto nitrocellulose membranes and dried for 15 min. Triplicates of whole cell protein extracts (4.2.4) were then dotted in a six step linear dilution series onto the membrane (equals 1.3 x 10^3-8.4 x 10^4 cells). Primary and secondary antibodies were applied as described before (4.2.4) and detected using a fluorescence imaging system (LI-COR ODYSSEY IR Scanner). The mean intensities of reconstituted and linearly diluted VSG-antibody complexes were determined from the membrane compared to determine the relative concentration reconstituted in lipid bilayers. A mean surface are of 144 μm^2 of bloodstream form trypanosomes [89] was assumed for the comparison.

Calculation of free VSG distances in supported lipid bilayers

The average distance (d) between VSG dimers reconstituted in supported lipid bilayers was calculated based on the lipid-to-protein ratio and protein geometry. The depth (d_{VSG}) and width (w_{VSG}) of the N-terminal domains of VSG M1.2 and ILTat1.24, both resolved by X-ray crystallography, were measured as a reference for VSG dimensions. As a mean, a depth of 6.5 nm and a width of 4.5 nm were assumed for VSG dimensions. The lateral protein-protein distances were then calculated for different scenarios considering protein density and rotational freedom of the dimers. At low protein densities (lpr > 300) free

lateral rotation on a honeycomb lattice was assumed (equation 4.1) with r_{rot} = (d^2_{VSG} + w^2_{VSG})$^{1/2}$ and A_L being the area per SOPC head group (0.6 nm^2):

$$d = \left\{ \begin{array}{ll} 2(\frac{\sqrt{lpr*A_L}}{\pi}) - r_{rot}) & \text{for } lpr \geq 300 \\ (1-f)d_{lpr\leq 80} + f d_{lpr\geq 300} & \text{for } 80 \leq lpr \geq 300 \\ \frac{1}{2}(-(w_{VSG} - d_{VSG}) + \sqrt{(w_{VSG}) - d_{VSG})^2 + 4A_L}) - l & \text{for } lpr \leq 80 \end{array} \right\}. \quad (4.1)$$

The area of a rotating VSG dimer cover $\sim$ 80 x A_L. thus, at high protein densities (lpr < 80) free lateral rotation was assumed to be sterically hindered and VSGs orientate on a rectangular grid. At intermediate protein densities (80 < lpr < 300), a conversion from free rotation to stationary alignment was considered. In this case, the protein distance was calculated from a weighted mean of distances at high and low densities. A weighting factor was introduced ($f = \frac{(lpr-80)}{219}$) and the upper threshold was chosen to facilitate a smooth transition between the regimes.

4.2.8 Fluorescence microscopy

FRAP

The method of fluorescence recovery after photobleaching (FRAP) was used to determine ensemble diffusion coefficients of VSGs reconstituted into SLBs.

An inverted widefield microscope (Till photonics) equipped with a digital scan-head for the control of a 473 nm laser line, appropriate excitation and emission filters and a CCD camera were used to perform the experiments (see section 4.1.6). Usually, 10 consecutive pre-bleaching images were acquired every 2 s using 100 ms sample illumination within a field-of-view of > 20 x 20 μm. A uniform circular irradiation with a 100 ms laser pulse (20-30% intensity) was then used to irreversibly bleach the region of interest (ROI, r = 5 μm). 100-150 consecutive images were then subsequently acquired at intervals of 2 s with an illumination time of 100 ms to monitor the fluorescence recovery in the ROI. The fluorescence images were then analyzed as described by Soumpasis [25], which involved corrections for continuous background bleaching and data normalization. The half-recovery time of fluorescence (τ) was determined by fitting data points to equation 4.2, with I_0 and I_1 being modified Bessel functions of second kind and zeroth or first order:

$$f(t) = exp^{\frac{-2\tau}{t}}[I_0(\frac{2\,\tau}{t}) + I_1(\frac{2\tau}{t})], \quad \text{with} \quad f(t) = \frac{F(t) - F(0)}{F(\infty) - F(0)} \quad (4.2)$$

where $F(t)$ is the actual fluorescence intensity, $F(0)$ the intensity directly after irreversible bleaching and $F(\infty)$ the fully recovered fluorescence signal. The lateral diffusion coefficient D was then calculated from equation 4.3.

$$D = \frac{r^2}{\tau}. \tag{4.3}$$

Single-molecule imaging

Single-molecule fluorescence microscopy was performed at RT on an inverted wide-field microscope (Leica DMI6000B) equipped with a high numerical aperture lens (HCX PL APO 100x objective lens (NA 1.47 OIL)) and an EMCCD camera (iXon3 DU-897, 512 x 512 pixel sensor format, pixel size = 16 μm). Two solid state diode lasers (Cobolt Fandango 515 nm, Cobolt MLD 640 nm) were used for sample illumination in the ROI with a mean laser intensity of 1 or 2 kW cm^{-2}. Fluorescence signals were detected by the camera using appropriate filter combinations (4.1.6). Illumination times depended on the experimental setup and readout mode of the camera sensor chip (normal readout mode in the ROI or frame transfer + cropped mode) and were either 10 ms or 4.9ms. Synchronization of illumination and camera readout was achieved using an acousto-optical tunable filter (AOTFnc-400.650-TN). The camera signal triggered a function generator (HM81-50, Rohde), which transmitted rectangular signals to the AOTF, and thereby specified the illumination starting point and duration. Final acquisition cycle times depended on image size and camera readout mode (64x64 pixel or 120x120 in ROI mode; 95x95 pixel in frame transfer + cropped mode) leading to imaging frequencies of 28, 42 and 200 Hz, respectively. Up to 10.000 successive background subtracted images were recorded. An image splitter (OptoSplit II) was mounted in front of the EMCCD camera for real-time two-color imaging. An open source microscopy software (μmanager) was used to control the settings of the camera and AOTF.

4.2.9 Analysis of single-molecule microscopy data

Single-molecule localization

Image analysis was performed using programs written in MATLAB (The MathWorks, R2014a-R2017a) as described before [35, 36] in order to localize single fluorophores with high a positional accuracy. To this end, the large-scale image background was subtracted via low-spatial-frequency filtering. Resulting images were then filtered by cross-correlation with a Gaussian as an approximation for the point-spread function (PSF) of the microscope. A threshold was then set to distinguish noise from fluorophore signals and typically only signals larger then 5-fold the noise were categorized as single-molecules. Finally, remaining single-molecules peaks were fitted to the PSF to retrieve information about their

x/y-positions, signal intensities and spatial widths of the signals and background signals. These parameters were then compared to previously determined single-fluorophore footprints and detection error thresholds. This allowed the identification of single molecules and the removal of signals originating from aggregates or large structures. The single-molecule parameters were then stored in a data matrix and used for further data analysis.

Single-molecule tracking

Trajectories of particles were generated by correlation of molecule localizations in an image to localizations in subsequent images. The algorithm used for single-particle identification and tracking was developed by Thomas Schmidt and colleagues and was further extended. The method applies a probabilistic algorithm to connect positions of molecules in two frames, i and j, of a movie. The probability (p) that a molecule k in image I_i is identical to a particle l in I_j depends on the diffusion coefficient (D) of the molecule and is given by:

$$p(k,l) = exp(-\frac{(\vec{s}_{\mathrm{k,i}} - \vec{s}_{\mathrm{l,j}})^2}{4D\Delta t}) \tag{4.4}$$

with Δt being the time-lag between consecutive frames. A transitional matrix is created that contains the probabilities of all possible connections between all M molecules in I_i and N molecules in I_j. These connections are further evaluated with respect to the total probabilities within a time step and from these a combination of connections is chosen in such a way that the total probability is maximized. The algorithm required an estimation of the particle diffusion coefficient as an input parameter (D_{in}) to calculate the probabilities of connections and the resulting diffusion coefficient of a particle (D_{out}). In order to minimize incorrect particle connections, a repetitive analysis over a range of D_{in} values was performed and the resulting D_{out} was calculated. The final algorithm input values were then chosen where D_{out} values became independent of D_{in}. Further, corrections for photobleaching of single molecules and diffusion in-and-out of the field of view were considered. A minimum number of consecutive steps within a trace was set as a criteria for further data analysis (20 for VSG ATTO647N and 10 for DOPE 488 lipids).

Analysis of single-particle trajectories

Single-particle tracking can provide insights into molecule dynamics with high temporal an spatial resolution. The analysis methods of such measurement results are versatile, but commonly multiple steps encompassing particle trajectories are the basis of data analysis. In the experiments performed in this work, the generation of trajectories was the starting point for the determination of the diffusion coefficients of VSGs and lipid integrated into

supported lipid bilayers and VSGs on the plasma membrane of trypanosomes. A detailed analysis of these trajectories was performed using two different approaches.
The first method applied a mean-square displacement (MSD) analysis of single trajectories to derive the diffusion coefficients of the molecules. Starting from the trajectories generated from single-molecule localizations, the MSD for a trajectory of N consecutive steps at a time lag $\tau = n\Delta t$ was calculated as:

$$MSD(n\Delta t) = \frac{1}{N-1-n} \sum_{i=1}^{N-1-n} \{[x(i\Delta t + n\Delta t) - x(i\Delta t)]^2 + [y(i\Delta t + n\Delta t) - y(i\Delta t)]^2\}, \quad (4.5)$$

where x and y denote the position of a particle within a trajectory at time t, and Δt is the smallest time interval resolved. The particles were then categorized as immobile or mobile by comparing their MSD to the achieved single-molecule localization precision, σ. Immobile particles were categorized by $\text{MSD}_{immob} \leq 4\sigma^2$ and excluded from further analysis as they represent aggregates or strong interaction of a particle with e.g. the underlying solid support. This categorization allowed the determined of a samples mobile fraction. The remaining, mobile particles were further analyzed by averaging their MSDs. The averaged MSD and the time between consecutive frames were then corrected for limitations in temporal and spatial resolution (equation 4.6) [54, 55, 53].

$$MSD_{corr} = MSD - 4\sigma^2 \quad and \quad t_{corr} = t - \frac{t_{\Delta ill}}{3}, \quad (4.6)$$

where t_{ill} denotes the sample illumination time. The diffusion coefficient of the mobile fraction was then finally calculated as one-fourth of the slope of the $MSDcorr(t_{corr})$ curve using a linear fit to the first 3 data points. This method provided a robust way to determine the mobile fraction within a sample and the determination of the diffusion coefficient of the mobile particles represented a fundamental property of the particle motion. However, it was derived from the averaged MSDs and thereby the mean of all mobile particles. This prevented a precise determination of individual mobile fractions that could occur within a sample of mobile particles.
A second analysis method was therefore performed in order identify individual populations within all freely diffusing particles of a sample. The analysis method was developed by Mislav Cvitković and Ana-Sunčana Smith from the Friedrich-Alexander-Universität Erlangen-Nürnberg and applied for membrane integrated VSG M1.1 and DOPE488 (see Section 2.1.3). A detailed description of the experimental setup and data analysis method was published by Bartossek and Jones [91]. In brief, ATTO647N labeled VSGs and DOPE488 were integrated into preformed SLBs at low protein densities followed by single-molecule imaging as described previously (4.2.8). The identified single-molecule positions were then used for the generation of individual particle trajectories. These trajectories were then further analyzed by the cooperation partners. In a first step, immobile particles were

removed by filtering the trajectories for stretches of non-Gaussian behavior using the strong separation in the characteristic step length of mobile and immobile molecules. For that purpose, the mean step length ($\langle L^2 \rangle$) of all trajectories was calculated and $T = 0.15 < L^2 >$ set as a threshold. Sequences of at least ten successive steps with a square step length smaller then this threshold were identified as immobile and removed from further analysis. This procedure was reiterated with the remaining data until the determined threshold saturated at 0.06 μm^2. The remaining trajectories showed characteristics of two different freely diffusion populations with significant overlaps. These populations were denoted as slow and fast and were further separated. For that purpose, besides thresholding, an addition statistical criterion was introduced into the analysis. This criterion was based on the calculation of probability likelihoods and the analysis method was performed on the entire set of mobile trajectories. This procedure allowed the classification of each trajectory as slow or fast. Furthermore, the diffusion coefficients of both populations were then calculated (i) from the ensemble average as the mean of the distributions of diffusion coefficients calculated from the MSD analysis per trace and (ii) from the MSD analysis of one concatenated trace containing all traces of one subpopulation (time average).

Super-resolution imaging in living *T. brucei* cells

Trypanosomes were immobilized in novel cross-linkable hydrogels as a preparation for *in vivo* single-molecule fluorescence microscopy. In order to quantify the immobilization efficiency of the hydrogels, super-resolution imaging of the flagellar axoneme was performed. To this end, a transgenic cell line was used, that constitutively expresses kinesin-MORN::eYFP. The cell line was generated by Ines Subota and kindly provided for the experiments. The mean axoneme diameter of immobilized trypanosomes was then calculated from reconstructed from super-resolution images of chemically fixed cells and compared to mean axoneme diameter immobilized living cells. Residual flagellar bead of incompletely immobilized cells should result in a spread out intensity distribution of eYFP molecules. For single-molecule imaging, the same microscopic setup as described in section 4.2.8 was used. The region of interest was set to 120x120 pixels with a pixel size of 160 nm. The cells were illuminated with a 515 nm laser beam for 10 ms at a mean intensity of 1 kW cm^{-1}. Due to a high label density inside the flagellar structure, cells were bleached until single-fluophore spots became visible before image acquisition started. 8000-10000 consecutive images were then recorded at 28 Hz. The intrinsic blinking behavior of eYFP molecules at high illumination intensities [112, 65] allowed multiple illumination cycles and a clear distinction of single-molecule localizations before fluorophores were irreversibly bleached. Image processing for single-molecule localization was then performed as describe before (4.2.9) including data filtering with respect to known eYFP footprints and detection error thresholds. Super-resolution images were then calculated

as the sum of all single-eYFP localizations. Each localized molecule was plotted as a 2D Gaussian spot with its respective localization precision, σ, being the width of its profile. Next, a countour line along the axonemal signal was mapped to quantify the width of the eYFP signal and thereby the width of the axoneme. Perpendicular lines to the contour lines were set and the average profile widths were calculated as a full-width half-maximum from a Gaussian fit to the data points. The immobilization efficiency of embedded trypansomes was then quantified by comparing their mean average axonemal diameter to the mean axonemal diameter of chemically fixed and immobilized trypanosomes.

Determination of the label density and autofluorescent background in super-resolution images

The label density in the axoneme was determined from super-resolution images of immobilized, kinesin-MORN::eYFP expressing trypanosomes. To this end, fluorescent background signals resulting from hydrogel contaminations or intracellular autofluorescence were separated from specific axoneme eYFP signals in a two-step procedure. First, a nearest neighbor analysis was applied to molecule localizations in the super-resolution images in order to remove sparsely distributed signals from hydrogel contaminants and intracellular fluorescence. Setting a threshold of 10 localized objects within a square of side length 240 nm effectively removed unspecific noise pixels and small clusters. Remaining clustered objects were removed in a second step by first manually masking everything but the axoneme. The area of the flagellum was then redefined by multiplying the resulting coarse-grained mask with a mask generated from the remaining localizations after the nearest neighbor analysis. The resulting, fine grained mask was then finally applied to all images to identify and count eYFP molecules ($N_{eYFP,Fl}$) localized to the flagellar area (A_F). This allowed the calculation of the label density, p, as $p = \frac{N_{eYFP,Fl}}{A_F}$ and the average density of the background signal $p_{BG} = \frac{N_{eYFP} - N_{eYFP,Fl}}{A - A_F}$, where N_{eYFP} denotes the number of all found localizations and A the are of the ROI. False-positive single-molecule localizations in the flagellar region were estimated from the ratio $r = \frac{p_{BG}}{p}$.

Studying the plasma membrane organization in living trypanosomes

Single-molecule fluorescence microscopy was applied to study the plasma membrane organization of living trypanosomes, with a focus on the inner leaflet of the plasma membrane. To this end, a transgenic cell line was used, that expresses a dual acylated eYFP fusion protein (section 4.2.1). The short sequence, that encodes for the acylation sides was adapted from the Hydrophilic Acylated Surface Protein B (HASPB) in *Leishmania major* and localizes the eYFP to the inner leaflet of the plasma membrane.
The lateral diffusion of the eYFP molecules in the membrane was monitored using single-molecule microscopy as described before (4.2.9). In brief, the image size was set to

120 x 120 pixels with a pixel size of 160 nm. The cells were then illuminated for 10 ms with a 515 nm laser beam (Cobolt) at a mean intensity of 2 kW cm^{-1}. Pre-bleaching was performed to monitor single-molecules and then 8000-10000 consecutive images were recorded at 28 Hz. eYFP signals were singled-out by exploiting the intrinsic blinking behavior of eYFP at high illumination intensities and single-eYFP molecules were then localized with high precision (4.2.9). The expression of the fusion protein ensured a high label density and its mobility allowed to probe the full plasma membrane area for putative nanometric domains. Immobile hydrogel contaminations were excluded from the process of scanning for areas of preferred occupancy. For that purpose, manually defined masks were generated to separate plasma membrane signals from background fluorescence. Further, eYFP signals were excluded that were localized in the same area of their first appearance (defined by the localization precision) within 50 consecutive frames. The remaining localized eYFP molecules were then used for the further analysis.

Identification of nonrandom distributions in the plasma membrane

Nonrandom distributions of HASP::eYFP in the plasma membrane were identified using Ripley's $L(r) - r$ function ([180],

$$L(r) - r = \sqrt{\frac{K(r)}{\pi - r}} \tag{4.7}$$

with Ripley's K-function that counts the mean number of neighboring eYFP molecules in a distance of radius, r, for N points in an area A:

$$K(r) - r = \frac{A}{N^2} \sum_{i \neq 1}^{N} w_{ij}^{-1} I_r(d_{ij}). \tag{4.8}$$

Here, d_{ij} denotes the distance between two eYFP molecules and the counting measure is $I_r(d_{ij}) = 1$ for distance $d_{ij} \leq r$ and else $I_r(d_{ij}) = 0$. Edge effects are accounted by a weighting factor for $w_{ij} \geq 1$, that corresponds to the inverse of the proportion of a circles circumference with its center i passing through a point j that is found within the area A.
The analysis was performed by Susanne Fenz, based on matlab codes for single-molecule localization and Ripley's Analysis developed by Thomas Schmidt. The analysis followed the method described by Pezzarossa et al. [152].
In brief, occupancy maps were calculated from HASP::eYFP positions. These maps were initialized at an increased resolution by dividing each original pixel into nine subpixels. This range was chosen, based on results from cumulative distributions of nearest neighbor distances calculated between all single-molecule positions ([111]). The occupancy was then calculated as the number of all eYFP localizations per subpixel. Next, the maps were then scanned for regions of dilute HASP::eYFP appearances. To this end, subpixels with

a maximum of one localizations were labeled and extracted from the original data set by masking. The identified diluted subpixels were then artificially populated with 100 evenly spaced localizations. This resulted in separate data sets that included either the original dense HASP::eYFP positions or the artificially occupied positions that represent diluted areas.
Ripley's L(r)-r function was then applied to both scenarios to identify potential nonrandom distributions on the plasma membrane. This function yields 0 in case of complete spatial randomness and gives positive values in case of clustering. The maximum of the L(r)-r curve provides a good estimate for the domain radius. For the analysis, the ROI was divided into square tiles of a side length of 0.8 μm, with typically 60 tiles covering a whole trypanosome. The function was then calculated up to a radius, r, of 0.5 μm for each tile and was averaged over all tiles and all imaged trypanosomes.

4.2.10 Two-color single-molecule fluorescence microscopy

The implementation of an image splitter (OptoSplit II) in front of the EMCCD camera enabled real-time two-color single-molecule imaging. The device was mounted in front of the EMCCD. The central component is a dichroic mirror (F48-635, Chroma) with a cutoff in the range of $\sim$640 nm that facilitates the separation of the emission light and suitable emission filters (F37-551 and F76-635, Semrock). The separated light paths were then projected onto specific areas of the sensor chip of the EMCCD camera via an arrangement of mirrors inside the image splitter. The separation of the emission light paths facilitated a clear distinction of individual fluorophores (ATTO647N and DOPE488) but required additional image processing to register the images of both color channels. First, single-molecule positions were corrected for the large horizontal offset displacements arising from the artificial image path separation. Second, the images were corrected for chromatic aberrations to precisely register both images.

Spreading of multicolor Tetraspeck beads on glass support

Multifluorescent beads (TetraSpeck Microspheres, 100 nm) spread on a glass surface were used as immobile reference objects to superimpose images that were previously separated in an image splitter device (OptoSplit II) and then projected on separate areas of the EMCCD camera sensor chip. The commercially available beads are stained throughout with four different fluorescent dyes and exhibit distinguishable emission peaks after illumination with 515 nm and 640 nm laser lines. For the detection of single beads, 1 μl of a stock solution (1.8 x 10^{11} particles per mL) was diluted in 500 μl mpH_2O. 100 μl of this dilution was then pipetted on a Hellmanex II cleaned glass mounted in a microscopy chamber. The chamber was heated to 80°C (in the dark) until the water was completely evaporated ($\sim$30 min). The chamber was then covered with aluminum foil to avoid light induced

bleaching. Imaging was performed as described before (4.2.8) using low laser powers for the illumination of the samples. Typically, 2 mW output power of both lasers (the laser spot size was ∼200 pixel FWHM at $\lambda_{640\ nm}$ and ∼120 pixels FWHM at $\lambda_{515\ nm}$) resulted in a strong detectable fluorescence signal. Up to 1000 consecutive images were then acquired with 10 ms sample illumination and total image cycle times of 28 Hz in a ROI of 120-300 pixels. The microscopic stage was slowly moved manually above the objective lens while recording the movies. This was conducted to cover a multitude of single-molecule positions within the ROIs. Image processing and single-molecule detection were then preformed as described before 4.2.9.

Image processing in two-color single-molecule microscopy

Image processing for the registration of color channel images from two-color single-molecule microscopy was performed using Matlab. A program was written that generates a transformation matrix from the localization of reference point-source objects (e.g. multi-fluorescent TetraSpeck beads). The transformation mask was then be applied to two-color single-molecule microscopy data in order to interpolate the shift for areas which had not been covered by the beads. The program (Overlay_2_Colors_mainFunc.m) involved the following image processing steps:
1) EstimateInputOverlay_2_Color.m: Plots the distribution of single-molecule intensities and widths derived from Gaussian-fitting (Standardanalysis.m). Visualization of the results facilitates the determination of parameters for data clearing according to the respective single-molecule footprints. This allows the user to manually define the size of the ROIs form both color channels. The program calculates a large-scale horizontal shifting parameter that accounts for the offset arising from artificial image separation. The offset parameter is used as an input parameter in step 2).
2) Overlay_2_Colors.m: Corrects coordinates form localizations in the red color channel according to the offset parameter. Generates close proximity of bead localizations that belong to one physical origin. For every frame the program applies a nearest neighbor distance approach to these localizations to assign reference partners. In a next step, the program generates a transformation matrix. The matrix was generated using a Matlab function that fits a local weighted mean transformation to the set of predefined fixed (localizations from the green channel) and moving (localizations from the red channel) reference data points that are related by a global second degree polynomial across the entire ROI (uses the Matlab built-in function images.geotrans.LocalWeightedMeanTransformation2D.m). Verifies the precision of the transformation process by applying the transformation matrix to offset corrected coordinates from the red channel. Calculates the mean difference between localizations in the green channel and transformed coordinates from the red channel. A graphical output (heatmap) of the remaining small-scale error before and after correction for chromatic aberrations allows the user to verify the transformation precision by the eye.

The following steps are extensions of the program and facilitate the application of the transformation matrix to data derived from SMFM. The results are not part of this work and presented for the sake of completeness:
3) TwoColorROIcut.m: Separates coordinates from SMFM localizations in both color channels.
4) mainFuncClearTwoColors.m: Clears single-molecule data with respect to the specifications.
5) Apply_tformLocalWeightedMean.m: Applies the transformation matrix generated in 2) to localizations from the red channel in SMFM experiments to register both color channels.

5. Bibliography

Bibliography

[1] Hooke R. (1665). Micrographia: or Some Physiological Descriptions of Minute Bodies, Made by Magnifying Glasses with Observations and Inquiries Thereupon. (London: James Allestry)

[2] Van Leeuwenhoek A. (1977). The Selected Works of Antony van Leeuwenhoek Containing His Microscopical Discoveries in Many of the Works of Nature. *Reprint New York: Arno Press*. London, s.p., 1798-1807, 2 vols.

[3] Von Gerlach J. (1858). Mikroskopische Studien aus dem Gebiet der menschlichen Morphologie. *Gazetta Medica Italiana*. (Erlangen: Enke)

[4] Golgi C. (1873). Sulla struttura della sostanza grigia del cervello. (Communicazione preventiva) *Gazetta Medica Italiana*, **33**: 244-246

[5] Giemsa G. (1904). Eine Vereinfachung und Vervollkommnung meiner Methylenblau-Eosin-Färbemethode zur Erzielung der Romanowsky-Nocht'schen Chromatinfärbung. *Centralblatt für Bakteriologie*, Abteilung **32**: 307–313

[6] Herschel J. F. W. (1845). On a case of superficial colour presented by a homogeneous liquid internally colourless. *Phil. Trans. R. Soc. Lond.*, **135**: 143-145

[7] Stokes C.G. (1852). On the change of refrangibility of light. *Phil. Trans. R. Soc. Lond.*, **142**: 463-562

[8] Ehrlich P. (1882). Über provozirte Fluoreszenzerscheinungen am Auge. *Deutsche medizinische Wochenschrift*, 35-37

[9] Kubitschek U. (2013). Fluorescence microscopy. From Principles to Biological Applications (ed. Kubitschek U.) (Wiley-Blackwell)

[10] Heimstädt O. (1911). Das Fluoreszenzmikroskop. *Zeitschr. Wissensch. Mikrosk.*, **28**: 330-337

[11] Lehmann H. (1913). Das Lumineszenz-Mikroskop, seine Grundlagen und seine Anwendungen. *Zeitschr. Wissensch. Mikrosk.*, **30**: 418-470

[12] Shimomura O., Johnson F. H. and Saiga Y. (1962). Extraction, purification and properties of aequorin, a bioluminescent protein from the luminous hydromedusan, *Aequorea*. *J. Cell Comp. Physiol.*, **59**: 233-239

[13] Lippincott-Schwartz J. and Patterson G. H. (2003). Development and use of fluorescent protein markers in living cells. *Science*, **300**: 87-91

[14] Chudakov D. M., Lukyanov S. and Lukyanov K. A. (2007). Tracking intracellular protein movements using photoswitchable fluorescent proteins. *Nat. Protoc.*, **2**: 2024-2032

[15] Baker S. M., Buckheit R. W. 3rd. and Falk M. M. (2010). Green-to-red photoconvertible fluorescent proteins: tracking cell and protein dynamics on standard wide-field mercury arc-based microscopes. *BMC Cell Biol.*, **11**: 15

[16] Keppler A., Gendreizig S., Gronemeyer T., Pick H., Vogel H. and Johnsson K. (2002). A general method for the covalent labeling of fusion proteins with small molecules *in vivo*. *Nat. Biotechnol.*, **21**: 86-89

[17] Bosch P. J., Correa Jr. I. R., Sonntag M. H., Ibach J., Brunsveld L., Kanger J. S. and Subramaniam V. (2014). Evaluation of Fluorophores to Label SNAP-Tag Fused Proteins for Multicolor Single-Molecule Tracking Microscopy in Live Cells. *Biophys. J.*, 107 (**4**): 803-814

[18] Suzuki T., Matsuzaki T., Hagiwara H., Aoki T. and Takata K. (2007). Recent Advances in Fluorescence Labeling Techniques for Fluorescence Microscopy. *JSHE*, 40 (**5**): 131-137

[19] Terai T. and Nagano T. (2013). Small-molecule fluorophores and fluorescent probes for bioimaging. *Arch. Eur. Phys.*, **465**: 283–291

[20] Hartel A. J. W., Glogger M., Guigas G., Jones N. G., Fenz S. F., Weiss M. and Engstler M. (2015). The molecular size of the extra-membrane domain influences the diffusion of the GPI-anchored VSG on the trypanosome plasma membrane. *Sci. Rep.*, **5**: 10394; doi: 10.1038/srep10394

[21] Combs C. A. (2010). Fluorescence Microscopy: A Concise Guide to Current Imaging Methods. *Curr. Protoc. Neurosci.*, **79**: 2.1.1-2.1.25

[22] Schermelleh L., Heintzmann R. and Leonhardt H. (1986). A guide to super-resolution fluorescence microscopy. *J. Cell. Biol.*, 190 (**2**): 165-175

[23] Sheppard C. J. R., Gan X., Gu M. and Roy M. (2006). Signal-to-Noise Ratio in Confocal Microscopes. In: Pawley J. (eds) Handbook Of Biological Confocal Microscopy. Springer Boston, MA

[24] Axelrod D., Koppel D. E., Schlessinger J., Elson E. and Webb W. W. (1976). Mobility measurement by analysis of fluorescence photobleaching recovery kinetics. *Biophys. J.*, **16**: 1055–1069

[25] Soumpasis D. M. (1983). Theoretical analysis of fluorescence photobleaching recovery experiments. *Biophys. J.*, 41 (**1**): 95-97

[26] Kirchhoff H., Haferkamp S., Allen J. F., Epstein D. B. and Mullineaux C. W. (2008). Protein diffusion and macromolecular crowding in thylakoid membranes. *Plant Physiol.*, **146**: 1571–1578

[27] Lorén N., Hagman J., Jonasson J. K., Deschout H., Bernin D., Cella-Zanacchi F., Diaspro A., McNally J. G., Ameloot M., Smisdom N., Nydén M., Hermansson A. M., Rudemo M. and Braeckmans K. (2015). Fluorescence recovery after photobleaching in material and life sciences: putting theory into practice. *Q. Rev. Biophys.*, 48 (**3**): 323-387

[28] Kourkoutis L. F., Plitzko J. M. and Baumeister W. (2012). Electron Microscopy of Biological Materials at the Nanometer Scale. *Annu. Rev. Mater. Res.*, **42**: 33-58

[29] Airy G.B. (1835). On the diffraction of an object-glass with circular aperture. *Trans. Cambridge Phil. Soc.*, **5**: 347-359

[30] Abbe E. (1873). Beiträge zur Theorie des Mikroskops und der mikroskopischen Wahrnehmung. *Archiv für Mikroskopische Anatomie*, **9**: 413–418

[31] Bobroff N. (1986). Position measurement with a resolution and noise-limited instrument. *Rev. Sci. Instrum.*, **57**: 1152-1157

[32] Deschout H., Zanacchi F. C., Mlodzianoski M., Diaspro A., Bewersdorf J., Hess S. T. and Braeckmans K. (2013). Precisely and accurately localizing single emitters in fluorescence microscopy. *Nat. Meth.*, 11 (**3**): 253-266

[33] Ober R. J., Ram S. and Ward E. S. (2004). Localization Accuracy in Single Molecule Microscopy. *Biophys. J.*, **86**: 1185–1200

[34] Abraham A. V., Ram S., Chao J., Ward E. S. and Ober R. J. (2009). Quantitative Study of Single Molecule Location Estimation Techniques. *Opt. Express*, **17**: 23352-23373

[35] Schmidt T., Schütz G. J., Baumgartner W., Gruber H. J. and Schindler H. (1996). Imaging of single molecule diffusion. *Proc. Natl. Acad. Sci. USA*, **93**: 2926-2929

[36] Fenz S., Pezzarossa A. and Schmidt T. (2012). The Basics and Potential of Single-Molecule Tracking in Cellular Biophysics, Comprehensive Biophysics Vol 2. (Cambridge: Academic Press, ed. Egelman Edward H.)

[37] Betzig E., Patterson G.H., Sougrat R., O. W. Lindwasser, Olenych S., Bonifacino J. S., Davidson M.W., Lippincott-Schwartz J. and Hess H. F. (2006). Imaging intracellular fluorescent proteins at nanometer resolution. *Science*, 313 (**5793**): 1642-1645

[38] Hess S. T., Giriaaja T. P. K. and Mason M. D. (2006). Ultra-high resolution imaging by fluorescence photoactivation localization microscopy. *Science*, 91 (**11**): 4258-4272

[39] Rust M. J., Bates M. and Zhuang X. (2006). Sub-diffraction-limit imaging by stochastic optical reconstruction microscopy (STORM). *Nat. Methods*, 3 (**10**): 793-795

[40] Shannon C. E. (1949). Communication in the Presence of Noise. *Proc. Inst. Radio Eng.*, **37**: 10-21

[41] Shaskova S. and Leake M. C. (2017). Single-molecule fluorescence microscopy review: shedding new light on old problems. *Biosci. Rep.*, **37**: DOI: 10.1042/BSR20170031

[42] Baddeley D. and Bewersdorf J. (2017). Biological Insight from Super-Resolution Microscopy: What We Can Learn from Localization-Based Images. *Annu. Rev. Biochem.*, **87**: 3.1-3.25

[43] Hell S. W. and Wichmann J. (1994). Breaking the diffraction resolution limit by stimulated emission: stimulated-emission-depletion fluorescence microscopy. *Opt. Lett.*, 19 (**11**): 780-782

[44] Klar T .A. and Hell S. W. (1999). Subdiffraction resolution in far-field fluorescence microscopy. *Opt. Lett.*, 24 (**14**): 954-956

[45] Donnert G. (2006). Macromolecular-scale resolution in biological fluorescence microscopy. *Proc. Natl. Acad. Sci.*, **103**: 11440-11445

[46] Manzo C. and Garcia-Parajo M. F. (2015). A Review of Progress in Single Particle Tracking: From Methods to Biophysical Insights. *Rep. Prog. Phys.*, **78**: 124601

[47] Semrau S. and Schmidt T. (2007). Particle Image Correlation Spectroscopy (PICS): Retrieving Nanometer-Scale Correlations from High-Density Single-Molecule Position Data. *Biophy. J.*, **92**: 613-621

[48] Slator P. J., Cairo C. W., Burroughs N. J. (2015). Detection of Diffusion Heterogeneity in Single Particle Tracking Trajectories Using a Hidden Markov Model with Measurement Noise Propagation. *PLoS One*, **10**: p.e0140759

[49] Chenouard N., Smal I., de Chaumont F., Maska M., Shalzarini I.F., Gond Y., Cardinale J., Carthel C., Coraluppi S., Winter M. et al. (1996). Objective Comparison of Particle Tracking Methods. *Nat. Methods*, **11**: 281-289

[50] Michalet X. (2010). Mean Square Displacement Analysis of Single-Particle Trajectories with Localization Error: Brownian Motion in an Isotropic Medium. *Phys. Rev. E*, **82**: 041914

[51] Saxton M. J. (1997). Single-Particle Tracking: The Distribution of Diffusion Coefficients. *Biophys. J.*, **72**: 1744-1753

[52] Daumas F., Destainville N., Millot C., Lopez A., Dean D. and Salome L. (2003). Confined Diffusion without Fences of a G-Protein-Coupled Receptor as Revealed by Single Particle Tracking. *Biophys. J.*, **84**: 356-366

[53] Semrau S., Pezzarossa A. and Schmidt T. (2011). Microsecond single-molecule tracking (μsSMT). *Biophys. J.*, **100**: L19-L21

[54] Wieser S., Moertelmaier M., Fuertbauer E., Stockinger H. and Schütz G. J. (2007). (Un)confined diffusion of CD59 in the plasma membrane determined by high-resolution single molecule microscopy. *Biophys. J.*, **92**: 3719-3728

[55] Schmidt T. and Schütz G. J. (2009). Handbook of Single Molecule Biophysics. (Berlin: Springer-Verlag, eds. Hinterdorfer P. and van Oijen A. 19-42)

[56] Kusumi A., Sako Y. and Yamamoto M. (1993). Confined lateral diffusion of membrane receptors as studied by single particle tracking (nanovid microscopy). Effects of calcium-induced differentiation in cultured epithelial cells. *Biophys. J.*, **65**: 2021-2040

[57] Lodish H., Berk A., Zipursky S. L., et al. (2000). Molecular Cell Biology. (New York: Freeman W. H., 4th edition. Section 19.3: Kinesin, Dynein and Intracellular Transport.)

[58] Sako Y., Minoguchi S. and Yanagida T. (2000). Single-molecule imaging of EGFR signalling on the surface of living cells. *Nat. Cell Biol.*, **2**: 168-172

[59] Hern J. A., Asma H. B., Mashanov G. I., Birdsall B., Corrie J. E. T., Lazareno S., Molloy J. E. and Birdsall J. M. (2010). Formation and dissociation of M_1 muscarinic receptor dimers seen by total internal reflection fluorescence imaging of single molecules. *PNAS*, 107 (**26**): 2693-2698

[60] Lommerse P. H. M., Blab G. A., Cognet L., Harms G. S., Snaar-Jagalska E., Hermann P. S. and Schmidt T. (2004). Single-Molecule imaging of the H-Ras Membrane-Anchor Reveals Domains in the Cytoplasmic Leaflet of the Cell Membrane. *Biophys. J.*, **86**: 609-616

[61] Lommerse P. H. M., Vastenhoud K., Pirinen N. J., Magee A. I., Spaink H. P. and Schmidt T. (2006). Single-Molecule Diffusion Reveals Similar Mobility for the LcK, H-Ras, and K-Ras Membrane Anchors. *Biophys. J.*, **91**: 1090-1097

[62] Bakker G. J., Eich C., Torreno-Pina J., Diez-Ahedo R., Perez-Samper G., van Zanten T. S., Figdor C. G., Cambi A. and Garcia-Parajo M. F. (2012). Lateral mobility of individual integrin nanoclusters orchestrates the onset for leukocyte adhesion. *PNAS*, 109 (**13**): 4869-4874

[63] Weigel A. V., Tamkun M. M. and Krapf D. (2013). Quantifying the dynamic interactions between a clathrin-coated pit and cargo molecules. *PNAS*, 110 (**48**): E4591-E4600

[64] Singer L. D. and Nicolson G. L. (1970). The fluid mosaic model of the structure of cell membranes. *Science*, 175 (**4023**): 720-731

[65] Lee S. F., Thompson M. A., Schwartz M. A., Shapiro L. and Moerner W. E. (2011). Super-Resolution Imaging of the Nucleoid-Associated Protein HU in *Caulobacter crescentus*. *Biophys. J.*, **100**: L31-L33

[66] Löschberger A., van de Linde S., Dabauvalle M. C., Rieger B., Heilemann M., Krohne G., and Sauer M. (2011). Super-resolution imaging visualizes the eightfold symmetry of gp210 proteins around the nuclear pore complex and resolves the central channel with nanometer resolution. *J. Cell. Sci.*, **125**: 570-575

[67] Richter R., Mukhopadhyay A. and Brisson A. (2003). Pathways of lipid vesicle deposition on solid surface: A combined QCM-D and AFM study. *Biophys. J.*, **85**: 3035-3047

[68] Blodgett K. B. (1935). Films built by depositing successive monomolecular layers on a solid surface. *J. Am. Chem. Soc.*, **57**: 1007-1022

[69] Ladha S., Mackie A. R., Clark D. C., Lea E. J. A., Brullemans M. and Duclohier H. (1996). Lateral Diffusion in Planar Lipid Bilayers: A Fluorescence Recovery after Photobleaching Investigation of its Modulation by Lipid Composition, Cholesterol, or Alamethicin Content and Divalent Cations. *Biophy. J.*, **71**: 1364-1373

[70] Schubert T., Bärmann M., Rusp M., Gränzer W. and Tanaka M. (2008). Diffusion of glycosylphosphatidylinositol (GPI)-anchored bovine prion protein (PrP^c) in supported lipid membranes studied by single-molecule and complementary ensemble methods. *J. Membr. Sci.*, **321**: 61-68

[71] Castella E. T. and Cremer P. S. (2006). Solid supported lipid bilayers: From biophysical studies to sensor design. *Surf. Sci. Rep.*, **61**: 429-444

[72] Mingeot-Leclerq M. P., Deleu M., Brasseur R. and Dufrene Y. F. (2008). Atomic force microscopy of supported lipid bilayers. *Nat. Protoc.*, 3 (**10**): 1654-1659

[73] Fenz S., Bihr T., Schmidt D. Merkel R., Sengupta K., Seifert U. and Smith A. S. (2017). Membrane fluctuations mediate lateral interaction between cadherin bonds. *Nat. Phys.*, **13**: 906-913

[74] Hu B., Finsinger D., Peter K. Guttenberg Z. Bärmann M. Kessler H., Escherich A., Moroder L. Böhm J., Baumeister W., Sui S. F. and Sackmann E. (2000). Intervesicle crosslinking with integrin alpha IIb beta 3 and cyclic-RGD-lipopeptide. A model of cell-adhesion processes. *Biochem.*, 39 (**40)**: 12284-12294

[75] Erb E. M., Tangemann K., Bohrmann B, Müller B. and Engel J. (1997). Integrin alphaIIb beta3 reconstituted into lipid bilayers is nonclustered in its activated state but clusters after fibrinogen binding. *Biochem.*, 36 (**24)**: 7395-7402

[76] VanHamme L., Paturiaux-Hanocq F., Poelvoorde P., Nolan D. P., Lins L., Abbeele J. V. D. Pays A., Tebabi P., Xong H.V., Jacquet A. et al. (2003). Apolipoprotein L-1 is the trypanosome lytic factor of human serum. *Nature*, **422**: 83-87

[77] Uzureau P., Uzureau S., Locordier L., Fontaine F., Tebabi P., Homble F., Grelard A., Zhendre V., Nolan D. P., Lins L. et al. (2003). Mechanism of *Trypanosoma brucei gambiense* resistance to human serum. *Nature*, **501**: 430-434

[78] Schlitzer M. (2009). Agents for the treatment of African sleeping sickness. Those developed in the last century. *Pharm. Unserer Zeit*, **38**: 552-558

[79] Chappuis F., Lima M.A. Fleuvaud L. and Ritmeijer K. (2010). Human African trypanosomiasis in areas without surveillance. *Emerg. Infect. Dis.*, **16**: 354-356

[80] Vassella E., Reuner B., Yutzy B. and Boshart M. (1997). Differentiation of African trypanosomes is controlled by a density sensing mechanism which signals cell cycle arrest via the cAMP pathway. *J. Cell. Sci.*, **110**: 2661-2671

[81] Field M. C., Horn D., Alsford S., Koreny L. and Rout M. P. (2012). Telomeres, tethers and trypanosomes. *Nucleus*, **3:6**: 478-486

[82] Cooper C., Clode P. L., Peacock C. and Thompson R. C. (2017). Host-Parasite Relationships and Life Histories of Trypanosomes in Australia. *Adv. Parasitol.*, **97**: 47-109

[83] Hemphill A., Lawson D. and Seebeck T. (1991). The cytoskeletal architecture of *Trypanosoma brucei*. *J. Parasitol.*, **77**: 603-612

[84] Bargul J. L., Jung J., McOdimba F. A., Omogo C. O., Adung'a V. O., Krüger T., Masiga D. K. and Engstler M. (2016). Species-Specific Adaptations of Trypanosome Morphology and Motility to the Mammalian Host. *PLoS Pathog.*, 12 (**2**): p.e1005448

[85] Langousis G. and Hill K. L. (2014). Motility and more: the flagellum of Trypanosoma brucei. *Nat. Rev. Microbiol.*, 12 (**7**): 505-518

[86] Overath P. and Engstler M. (2004). Endocytosis, membrane recycling and sorting of GPI-anchored protein: *Trypanosoma brucei* as a model system. *Mol. Microbiol.*, **53**: 735-744

[87] Grünfelder C. G., Engstler M., Weise F., Schwarz H., Stierhof Y. D. Morgan G. W. Field M. C. and Overath P. (2003). Endocytosis of a glycosylphotphatidylinositol-anchored protein via clathrin coated vesicles, sorting by default in endosomes, and exocytosis via RAB11-positive carriers. *Mol. Biol. Cell*, **14**: 2029-2040

[88] Ziegelbauer K. and Overath P. (1992). Identification of invariant surface glycoproteins in the bloodstream stage of *Trypanosoma brucei*. *J. Biol. Chem.*, **267**: 10791-10796

[89] Grünfelder C. G., Engstler M., Weise F., Schwarz H., Stierhof Y. D., Boshart M. and Overath P. (2002). Accumulation of a GPI-anchored protein at the cell surface requires sorting at multiple intracellular levels. *Traffic*, **3**: 547-559

[90] Cross G. A. M. (1975). Identification, purification and properties of clone-specific glycoprotein antigens constituting the surface coat of *Trypanosoma brucei*. *Parasitology*, **71**: 393-417

[91] Bartossek T., Jones N. G., Schäfer C., Cvitković M., Glogger M., Mott H. R., Kuper J., Brennich M., Carrington M., Smith A. S., Fenz S., Kisker C. and Engstler M. (2017). Structural basis for the shielding function of the dynamic trypanosome variant surface glycoprotein coat. *Nat. Microbiol.*, **2**: 1523-1532

[92] Cross G. A., Kim H. S. and Wickstead B. (2014). Capturing the variant surface glycoprotein repertoire (the VSGnome) of Trypanosoma brucei Lister 427. *Mol. Biochem. Parasitol.*, **195**: 59-73

[93] Hertz-Fowler C., Figueiredo L. M., Quail M. A., Becker M., Jackson A., Bason N., Brooks K., Churcher C., Fahkro S. Goddhead I. et al. (2008). Telomeric expression sites are highly conserved in Trypanosoma brucei. *PLoS One*, 3 (**10**): e3527

[94] Macaskill J. A., Holmes P. H., Jennings F. W. and Urquhart G. M. (1981). Immunological clearance of 75Se-labelled *Trypanosoma brucei* in mice. III. Studies in animals with acute infections. *Immunology*, **43**: 691-698

[95] Horn D. (2014). Antigenic variation in African trypanosomes. *Mol. Biochem. Parasitol.*, **2**: 123-129

[96] Seyfang A., Mecke D. and Duszenko M. (1990). Degradation, recycling and shedding of *Trypanosoma brucei* variant surface glycoprotein. *J. Protozool.*, **37**: 546-552

[97] Engstler M., Pfohl T., Herminghaus S., Boshart M., Wiegertjes G, Heddergott N. and Overath P. (2007). Hydrodynamic flow-mediated protein sorting on the cell surface of trypanosomes. *Cell*, **131**: 505-515

[98] Guigas G. and Weiss M. (2016). Effects of protein crowding on membrane systems. *Biochim. Biophys. Acta*, 1858 (**10**): 2441-2450

[99] Engstler M., Thilo L., Weise F., Grünfelder C. G., Schwarz H., Boshart M. and Overath P. (2004). Kinetics of endocytosis and recycling of the GPI-anchored variant surface glycoprotein in Trypanosoma brucei. *J. Cell. Sci.*, **7**: 1105-1115

[100] Bülow R., Overath P. and Davoust J. (1988). Rapid lateral diffusion of the variant surface glycoprotein in the coat of Trypanosoma brucei. *Biochem.*, 27 (**7**): 2384-2388

[101] Schwede A., Macleod O. J. S., MacGregor P. and Carrington M. (2015). How Does the VSG Coat of Bloodstream Form African Trypanosomes Interact with External Proteins? *PLoS Pathog.*, 11 (**11**): e1005259 doi:10.1371/journal.ppat.1005259

[102] Mehlert A., Bond C. S. and Ferguson M. A. (2002). The glycoforms of a Trypanosoma brucei variant surface glycoprotein and molecular modeling of a glycosylated surface coat. *Glycobiology*, 12 (**10**): 607-612

[103] Stellemanns E., Uppaluri S., Hochstetter A., Heddergott N., Engstler M. and Pfohl T. (2014). Optical trapping reveals propulsion forces, power generation and motility efficiency of the unicellular parasites *Trypanosoma brucei brucei*. *Sci. Rep.*, **4**: 6515; DOI:10.1038/srep06515

[104] Hochstetter A., Stellamanns E., Deshpande S., Uppaluri S., Engstler M. and Pfohl T. (2015). Microfluidics-based single cell analysis reveals drug-dependent motility changes in trypanosomes. *Lab Chip*, 8 (**15**): 1961-1968

[105] Hartel A. J. W., Glogger M., Jones N.G., Abuillan W., Batram C., Hermann A., Fenz S. F., Tanaka M. and Engstler M. (2016). N-glycosylation enables high lateral mobility of GPI-anchored proteins at a molecular crowding threshold. *Nat. Commun.*, 3 (**7**): 12870 doi: 10.1038/ncomms12870

[106] Ahmed E.M. (2015). Hydrogel: Preparation, characterization, and applications: A review. *J. Adv. Res.*, **6**: 105-121

[107] Le N. N. T., Zorn S., Schmitt S. K., Gopalan P. and Murphy W. (2016). Hydrogel: Hydrogel arrays formed via differential wettability patterning enable combinatorial screening of stem cell behavior. *Acta Biomater.*, **34**: 93-103

[108] Lin C. C., Ki C. S. and Shih H. (2015). Thiol-norbornene photo-click hydrogels for tissue engineering applications. *J. Appl. Polym. Sci.*, **132**: 8

[109] Stichler S., Jungst T., Schamel M., Zilkowski I., Kuhlmann M., Böck T. Blunk T., Teßmar J. and Groll J. (2016). Thiol-ene Clickable Poly(glycidol) Hydrogels for Biofabrication. *Ann. Biomed. Eng.*, **45**: 273-285

[110] Erdelyi M., Rees E., Metcalf D., Kaminski Schierle T. S., Dudas L., Sinko J., Knight A. E. and Kaminski C. F. (2013). Correcting chromatic offset in multicolor super-resolution localization microscopy *Optics Express*, 21 (**9**): DOI:10.1364/OE.21.010978

[111] Glogger M., Stichler A., Subota I., Bertlein S., Spindler M. C., Teßmar J., Groll J., Engstler M and Fenz S. F. (2017). Live-cell super-resolution imaging of intrinsically fast moving flagellates. *J.Phys.D: Appl.Phys.*, 50 (**7**): 074004 (7pp)

[112] Fölling J., Bossi M., Bock H., Medda R., Wurm C. A., Hein B., Jakobs S., Eggeling C. and Hell S. W. (2008). Fluorescence nanoscopy by ground-state depletion and single-molecule return. *Nat. Methods*, **5**: 943-945

[113] Koyfman A. Y., Schmid M. F., Gheiratmand L., Fu C. J., Khant H. A., Huang D., He C. Y. and Chiu W. (2011). Structure of *Trypanosoma brucei* flagellum accounts for its bihelical motion. *Proc. Natl. Acad. Sci. USA*, 108 (**27**): 11105-11108

[114] Nicastro D., Schwartz C., Pierson J., Gaudette R., Porter M. E. and McIntosh J. R. (2006). The molecular architecture of axonemes revealed by cryoelectron tomography. *Science*, 313 (**5789**): 944-948

[115] Glogger M., Subota I., Pezzarossa A., Denecke A.L., Carrington M., Fenz S.F. and Engstler M. (2017). Facilitating trypanosome imaging. *Exp. Parasitol.*, **180**: 13-18

[116] Resh M. D. (1999). Fatty acylation of proteins: new insights into membrane targeting of myristoylated and palmitoylated proteins. *Biochim. Biophys. Acta*, 1451 (**1**): 1-16

[117] Wirtz E., Leal S., Ochatt C. and Cross G. A. M. (1999). A tightly regulated inducible expression system to the transcriptionally silent minichromosomes of *Tryanosoma brucei*. *Mol. Biochem. Parasit.*, **99**: 89-101

[118] Hartel A. J. W. (2013). Die laterale Diffusion des variablen Oberflächenglykoproteins in Trypanosomen und in artifiziellen Membranen. Doctoral dissertation, Julius-Maximilians-Universität Würzburg

[119] Dempsey G. T., Vaughan J. C., Chen K. H., Bates M. and Zhuang X. (2012). Evaluation of fluorophore for optimal performance in localization-based super-resolution imaging. *Nat. Methods.*, 8 (**12**): 1027-1036

[120] Albrecht D., Winterflood C. M. and Ewers H. (2015). Dual color single particle tracking via nanobodies. *Methods Appl. Fluoresc.*, **3**: 024001

[121] Shen H., Tauzin L. J., Baiyasi R., Wang W., Moringo N., Shuang B. and Landes C. F. (2017). Single Particle Tracking: From Theory to Biophysical Applications *Chem. Rev.*, 117 (**11**): 7331-7376

[122] Ghosh S. and Preza C. (2015). Fluorescence microscopy point spread function model accounting for aberrations due to refractive index variability within a speciman. *J. Biomed. Opt.*, 20 (**7**): 075003

[123] Deschout H., Neyts K. and Braeckmans K. (2012). The influence of movement on the localization precision of sub-resolution particles in fluorescence microscopy. *J. Biophotonics*, 5 (**1**): 97-109

[124] Rudhardt N., Lamb D. C. and Bräuchle C. (2011). Single-particle Tracking as a Quantitative Microscopy-based Approach to Unravel Cell Entry Mechanisms of Viruses and Pharmaceutical Nanoparticles. *Mol. Ther.*, 19 (**7**): 1199-1211

[125] Digman M. A., Brown C. M., Sengupta P., Wiseman P. W., Horwitz A. R. and Gratton E. (2005). Measuring fast dynamics in solutions and cells with a laser scanning microscope. *Biophys. J.*, **89**: 1317-1327

[126] Weimann L., Ganzinger K. A., McColl J., Irvine K. L., Davis S. J., Gay N. J., Bryant C. E. and Klenerman D. (2013). A Quantitative Comparison of Single-Dye Tracking Analysis Tools Using Monte Carlo Simulations. *PLOS*, 8 (**5**): e64287

[127] Briane V., Kervrann C. and Vimond M. (2017). A statistical analysis of particle trajectories in living cells. *arXiv*, arXiv:1707.01838 [stat.AP]

[128] Gal N., Lechtman-Goldstein D. and Weihs D. (2013). Particle tracking in living cells: a review of the mean square displacement method and beyond. *Rheologica Acta*, 52 (**5**): 425-443

[129] Sustr D., Hlavacek A., Duschl C. and Volodkin D. (2018). Multi-Fractional Analysis of Molecular Diffusion in Polymer Multilayers by FRAP: A New Simulation-Based Approach. *J. Phys. Chem. B*, **122**: 1323-1333

[130] Pinger J., Chowdhury S. and Papavasiloiu F. N. (2017). Variant surface glycoprotein density defines an immune evasion threshold for African trypanosomes undergoing antigenic variation. *Nat. Commun.*, **8**: 828

[131] Macháň R. and Hof M. (2010). Lipid diffusion in planar membranes investigated by fluorescence correlation spectroscopy. *Biochim. Biophys. Acta*, **1798**: 1377-1391

[132] Høiberg-Nielsen R., Westh P., Skov L. K. and Arleth L. (2009). Interrelationship of Steric Stabilization and Self-Crowding of a Glycosylated Protein. *Biophys. J.*, **97**: 1445-1453

[133] Trombetta E. S. (2003). The contribution of N-glycans and their processing in the endoplasmic reticulum to glycoprotein biosynthesis. *Glycobiology*, 13 (**9**): 77R-91R

[134] Lee H. S., Qi Y. and Im W. (2015). Effects of N-glycosylation on protein conformation and dynamics: Protein Data Bank analysis and molecular dynamics simulation study. *Sci. Rep.*, **5**: DOI: 10.1038/srep08926

[135] Moraes I., Evans G., Sanchez-Weatherby J., Newstead S. and Stewart P. D. S. (2014). Membrane protein structure determination - The next generation. *Biochim. Biophys. Acta.*, **1838**: 78-87

[136] Kowal J., Biyani N., Chami M., Scherer S., Rzepiela A. J., Baumgertner P., Upadhyay V., Nimigean C. M. and Stahlberg H. (2017). High-Resolution Cryoelectron Microscopy Structure of the Cyclic Nucleotide-Modulated Potassium Channel MloK1 in a Lipid Bilayer. *Cell*, **26**: 20-27

[137] Zanotelli M. R., Ardalani H., Zhang J., Hou Z., Nguyen E. H., Swanson S., Nguyen B. K., Bolin J. et al. (2016). Stable engineered vascular networks from human induced pluripotent stem cell-derived endothelial cells cultured in synthetic hydrogels. *Acta. Biomater.*, **35**: 32-41

[138] Gramlich W. M., Kim I. L., Burdick J. A. (2013). Synthesis and orthogonal photopatterning of hyaluronic acid hydrogels with thiol-norbornene chemistry. *Biomaterials*, 34 (**38**): 9803-9811

[139] McMillan T.J., Leatherman E., Ridley A., Shorrocks J., Tobi S. E. and Whiteside J. R. (2008). Cellular effects of long wavelength UV light (UVA) in mammalian cells. *Biomaterials*, **8**: 969-976

[140] Gould K. M., Vu X. L., Seebeck T., and de Koning H.P. (2008). Propidium iodide-based methods for monitoring drug action in the kinetoplastidae: comparison with the Alamar Blue assay. *Anal. Biochem.*, 382 (**2**): 87-93

[141] King J. W., Jongpaiboonkit L., and Murphy W. L. (2010). Influence of FGF2 and PEG hydrogel matrix properties on hMSC viability and spreading. *J. Biomed. Mater. Res. A.*, 93 (**3**): 1110-1123

[142] Caliari S. R. and Burdick J. A. (2016). A practical guide to hydrogels for cell culture. *Nat. Methods*, 13 (**5**): 415-414

[143] Ichihara Y., Kaneko M., Yamahara K., Koulouroudias M., Sato N., Uppal R., Yamazaki K., Saito S., and Suzuki K. (2018). Self-assembling peptide hydrogel enables instant epicardial coating of the heart with mesenchymal stromal cells for the treatment of heart failure. *Biomaterials*, **34**: 93-103

[144] Courtey S., Luccardini C., Bellaiche Y. Cappello G. and Dehan M. (2006). The N-terminal Membrane Occupation and Recognition Nexus Domain of Arabidopsis Phosphatidylinositol Phosphate Kinase 1 Regulates Enzyme Activity. *J. Biol. Chem.*, 282 (**8**): 5443-5452

[145] Zhang L., Shang X. J., Li H. F., Shi Y. U., Li W., Teves M. E., Wang Z. Q., Jiang G. F., Song S. Z. and Zhang Z. B. (2015). Characterization of membrane occupation and recognition nexus repeat containing 3, meiosis expressed gene 1 binding partner, in mouse male germ cells. *Asian J. Androl.*, **17**: 86-93

[146] Morriswood B., He C. Y., Sealey-Cardona M., Yelinek J., Pypaert M. and Warren G. (2009). Rapid lateral diffusion of the variant surface glycoprotein in the coat of Trypanosoma brucei. *Mol. Biochem. Parasitol.*, **167**: 95-103

[147] Kolomeisky A. B. and Fisher M. E. (2007). Molecular Motors: A Theorist's Perspective. *Annu. Rev. Phys. Chem.*, **58**: 675-695

[148] Bridges D. J., Pitt A. R., Hanrahan O., Brennan K., Voorheis H. P., Herzyk P., de Koning H. P. and Burchmore R. J. S. (2008). Characterisation of the plasma membrane subproteome of bloodstream form *Trypanosoma brucei*. *Proteomics*, **8**: 83-93

[149] Dean S., Sunter J. D. and Wheeler R. J. (2017). TrypTag.org: A Trypanosome Genome-wide Protein Localisation Resource. *Cell*, 33 (**2**): 80-82

[150] Ramakrishnan S., Serricchio M., Striepen B. and Bütikofer P. (2013). Lipid synthesis in protozoan parasites: a comparison between kinetoplastids and apicomplexans. *Prog. Lipid. Res.*, 54 (**4**): 488-512

[151] Denny P. W., Gokool S., Russell D. G., Field M. C. and Smith D. F. (2000). Acylation-dependent Protein Export in *Leishmania*. *J. Biol. Chem.*, **275**: 11017-25

[152] Pezzarossa A., Zosel F. and Schmidt T. (2015). Visualization of HRas Domains in the Plasma Membrane of Fibroblasts. *Biophys. J.*, 102 (**8**): 1870-1877

[153] Lorent J. H. and Levental I. (2015). Structural determinants of protein partitioning into ordered membrane domains and lipid rafts. *Chem. Phys. Lipids*, **192**: 23-32

[154] Levental I., Grzybek M. and Simons K. (2010). Greasing their way: lipid modifications determine protein association with membrane rafts. *Biochem.*, 49 (**30**): 6305-6316

[155] Wu H. M., Lin Y. H., Yen T. C., and Hsieh C. L. (2016). Nanoscopic substructures of raft-mimetic liquid-ordered membrane domains revealed by high-speed single-particle tracking. *Sci. Rep.*, **6**: 20542; doi: 10.1038/srep20542

[156] Kohl L. and Gull K. (1998). Molecular architecture of the trypanosome cytoskeleton. *Mol. Biochem. Parasitol.*, **93**: 1-9

[157] Cho W. and Stahelin R.V. (2006). Membrane binding and subcellular targeting of C2 domains. *Biochim. Biophys. Acta.*, 1761 (**8**): 838-849

[158] Baines A. and Gull K. (2008). WCB is a C2 domain protein defining the plasma membrane - sub-pellicular microtubule corset of kinetoplastid parasites. *Protist.*, 159 (**1**): 115-125

[159] Kabbani A. M., Woodward X. and Kelly C. V. (2017). Revealing the Effects of Nanoscale Membrane Curvature on Lipid Mobility. *Membranes (Basel)*, **7**: 60; doi:10.3390

[160] Holcman D. and Schuss Z. (2013). Control of flux by narrow passages and hidden targets in cellular biology. *Rep. Prog. Phys.*, **76**: 6074601

[161] Deich J., Judd E. M., McAdams H. H. and Moerner W. E. (2004). Visualization of the movement of single histidine kinase molecules in live Caulobacter cells. *Proc. Natl. Acad. Sci. USA*, 101 (**45**): 15921-15926

[162] Haas B. L., Matson J. S., DiRita V. J. and Biteen J. S. (2015). Imaging live cells at the nanometer-scale with single-molecule microscopy: obstacles and achievements in experiment optimization for microbiology. *Molecules*, 19 (**8**): 12116-12149

[163] Arcizet D., Meier B., Sackmann E., Rädler J. O. and Heinrich D. (2008). Temporal analysis of active and passive transport in living cells. *Phys. Rev. Lett.*, 101 (**24**): 248103

[164] Holcman D., Hoze N. and Schuss Z. (2015). Analysis and Interpretation of Super-resolution Single-Particle Trajectories. *Biophys. J.*, 109 (**9**): 1761-1771

[165] Espenel C., Margeat E., Dosset P., Arduise C., Le Grimellec C., Royer C. A., Boucheix C., Rubinstein E., and Milhiet P. E. (2008). Single-molecule analysis of CD9 dynamics and partitioning reveals multiple modes of interaction in the tetraspanin web. *J. Cell. Biol.*, 182 (**4**): 765-776

[166] Pavani S.R.P. and Piestun R. (2008). Three Dimensional Tracking of Fluorescent Microparticles Using a Photon-Limited Double-Helix Response System. *Opt. Express*, **16**: 22048-22057

[167] Holtzer L., Meckel T. and Schmidt T. (2007). Nanometric three-dimensional tracking of individual quantum dots in cells. *Appl. Phys. Lett.*, 90 (**5): 053902**

[168] von Diezmann A., Shechtman Y. and Moerner W. E. (2017). Three-Dimensional Localization of Single Molecules for Super-Resolution Imaging and Single-Particle Tracking. *Chem. Rev.*, 117 (**11**): 7244-7275

[169] Stijlemans B., Conrath K., Cortez-Retamozo V., Xong H. V., Wyns L., Senter P., Revets H., De Baetselier P., Muyldermans S. and Magez S. (2004). Efficient targeting of conserved cryptic epitopes of infectious agents by single domain antibodies. African trypanosomes as paradigm. *J. Biol. Chem.*, 279 (**2**): 1256-1261

[170] Hirumi, H. and Hirumi, K. (1989). Continuous cultivation of *Trypanosoma brucei* blood stream forms in a medium containing a low concentration of serum protein without feeder cell layers. *J. Parasitol.*, **75**: 985–989

[171] Kelly S., Reed J., Kramer S., Ellis L., Webb H., Sunter J., Salje J., Marinsek N., Gull K., Wickstead B. and Carrington M. (2007). Functional genomics in *Trypanosoma brucei*: A collection of vectors for the expression of tagged proteins from endogenous and ectopic gene loci. *Mol. Biochem. Parasitol.*, **154**: 103-109

[172] Subota I., Rotureau B., Blisnick T., Ngwabyt S., Durand-Dubief M., Engstler M. and Bastin P. (2011). ALBA proteins are stage regulated during trypanosome development in the tsetse fly and participate in differentiation. *Mol. Biol. Cell.*, **22**: 4205-19

[173] Best A., Handoko L., Schlüter E. and Göringer H. U. (2005). *In vitro* synthesized small interfering RNAs elicit RNA interference in african trypanosomes: an *in vitro* and *in vivo* analysis. *J. Biol. Chem.*, **280**: 20573-20579

[174] Shu X. Z., Liu Y., Luo Y., Roberts M. C. and Prestwich G. D. (2002). Disulfide Cross-Linked Hyaluronan Hydrogels. *Biomacromolecules*, **6**: 1304-1311

[175] Clarke M. W., Olafson R. W. and Pearson T. W. (1985). Rapid preparative scale purification of myristylated variant surface glycoproteins from African trypanosomes. *Mol. Biochem. Parasitol.*, **17**: 19-34

[176] Carrinton M., Miller N., Blum M., Roditi I., Wiley D. and Turner M. (1991). Variant specific glycoprotein of trypanosoma brucei consists of two domains each having an independently conserved pattern of cysteine residues. *J. Mol. Biol.*, 221 (**3**): 823-835

[177] Holloway P. W. (1973). A simple procedure for removal of triton X-100 from protein samples. *Anal. Biochem.*, **53**: 304-308

[178] Bartlett G. R. (1959). Phosphorus assay in column chromatography. *J. Biol. Chem.*, 234 (**3**): 466-468

[179] Anderson R. L. and Davis S. (1982). An organic phosphorus assay which avoids the use of hazardous perchloric acid. *Clin. Chim. Acta*, 121 (**1**): 111-116

[180] Ripley B. D. (1979). Test of 'Randomness' for Spatial Point Patterns. *J. .R. Stat. Soc. Ser. B Stat. Methodol.*, **41**: 368-374

6. Appendix

6.1 Supporting figures

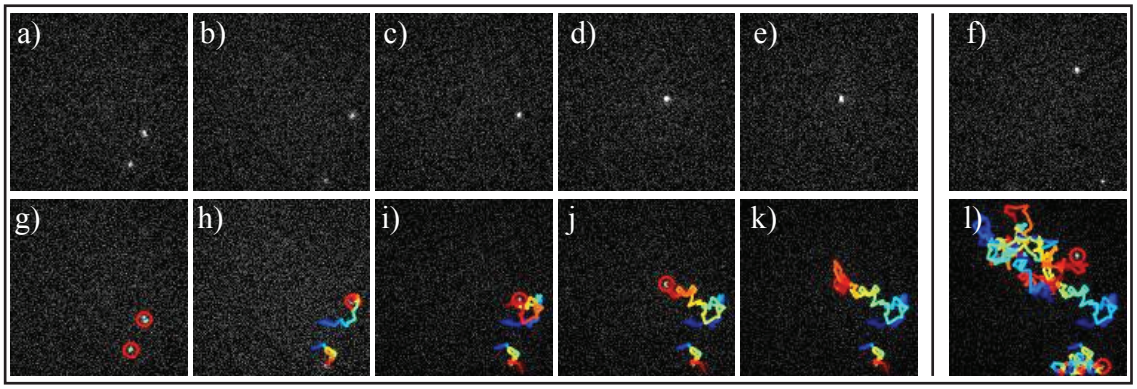

Figure 6.1: Single-molecule trajectories of VSG in SLBs. Exemplary fluorescence snapshots of fluorescently labeled VSGs integrated into a SLB (a-e = frame 1, 30, 60, 90 and 120; f = frame 500 of a movie, respectively) and the overlay of single-molecule positions (red circle) and VSG trajectories are illustrated. The steps within a trajectory are color coded. The trajectories extend from the first frame of the movie until the respective frames indicated in a-f.

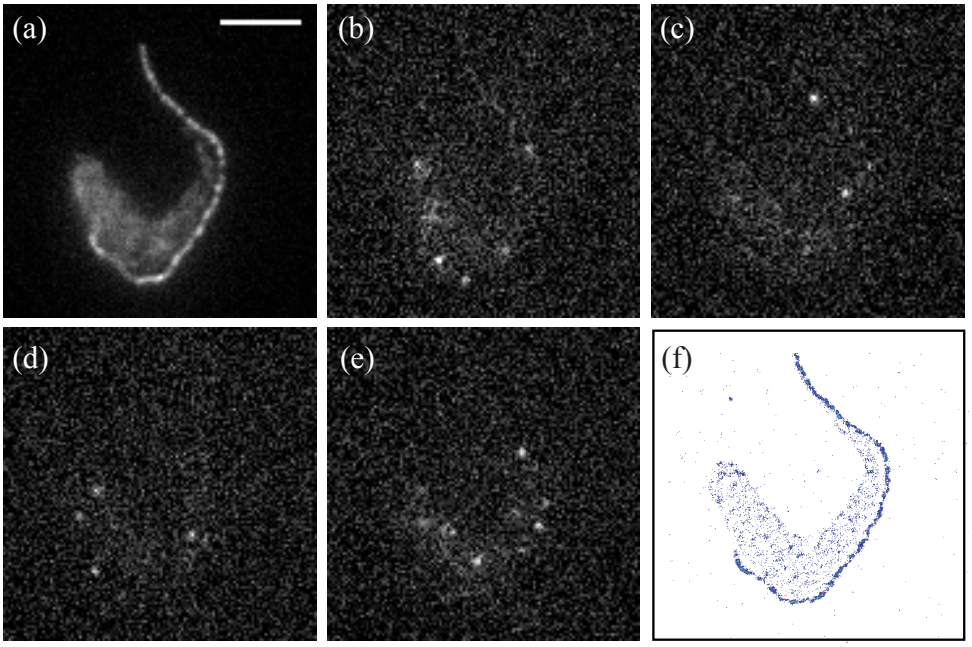

Figure 6.2: Super-resolution imaging of a *T. brucei* cell expressing kinesin-MORN::eYFP. The cell was immobilized in a 10% PEG-VS/HA-SH (w/v) hydrogel. a) Diffraction limited fluorescence snapshot of the eYFP in the flagellum and intracellular signal. b-e) Consecutive fluorescence images of blinking eYFP molecules at high illumination intensities. f) Reconstructed super-resolution image of the kinesin-MORN::eYFP expressing trypanosome. The scale bar is 5 μm and valid for a-f).

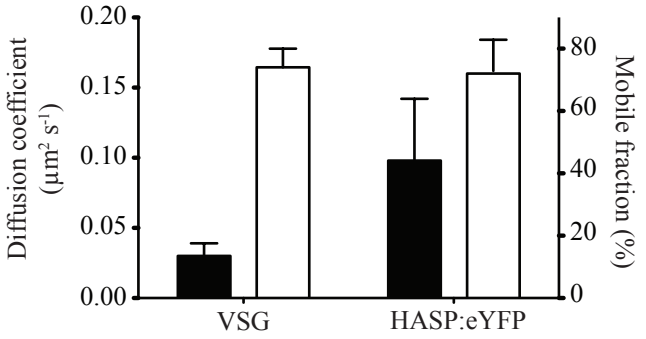

Figure 6.3: FRAP measurements of VSG and HASP:eYFP dynamics in live trypanosomes. HASP:eYFP was constitutively expressed in trypanosomes via stable integration of the vector pLEW82ΔOP. [173]. Transgenic cells were embedded in 8% (w/v) gelatin solution and line FRAP was performed at 20°C to determine VSG (N_{cells} = 21) and HASP::eYFP (N_{cells} = 26) diffusion coefficients. Surface VSGs were stained using ATTO-488 NHS-ester chemistry as described in [118].

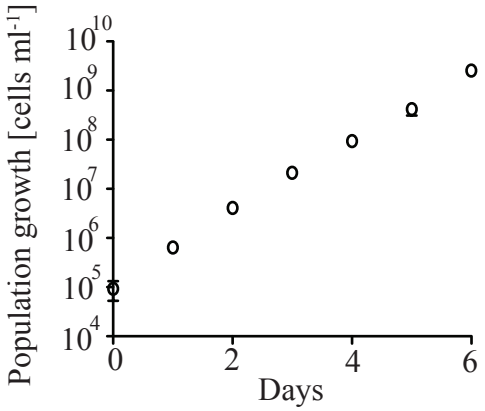

Figure 6.4: Growth curve of HASP::eYFP expressing *T. brucei* cells. The cells were started to count five days after transfection. Three replicates of a clonal population were used for the determination of the growth curve. The cells were cultivated with appropriate antibiotics (see 4.1.3).

6.2 List of abbreviations

λ	lambda, wavelength
μg	microgram
μm	micrometer
μl	micrometer
σ	sigma, localization precision
°C	grad Celsius
%	percent
AOTF	acuosto-optic tunable filter
BSF	bloodstream form
CMOS	complementary metal-oxide-semiconductor
CTD	C-terminal domain
cts	counts
D	diffusion coefficient
DOL	degree of labeling
DOPE	1,2-dioleoyl-sn-glycero-3-phosphoethanolamine
dT	dithiol
e.g.	exempli gratia
EMCCD	electron multiplying charge coupled device
eYFP	enhanced yellow fluorescent protein
FRAP	fluorescence recovery after photobleaching
FWHM	full-width half-maximum
g	gram
g	acceleration due to gravity
GPI	glycosylphosphatidyl-inositol
h	hour
HA-SH	thiol-modified hyaluronic acid
HPLC	high-performance liquid chromatography
Hz	Hertz
kDa	kilodalton
kW	kilowatt
mg	milligram
min	minute
mM	millimolar
ms	millisecond
NB	norbornene
NHS	N-hydroxysuccinimid

MORN	membrane occupation and recognition nexus
MSD	mean-squared displacement
NA	numerical aperture
nm	nanometer
nM	nanomolar
NTD	N-terminal domain
p	probability
P(AGE-*co*-G))	Poly(allyl glycidyl ether-*co*-glycidyl
PALM	photoactivated light microscopy
PCF	procyclic form
PEG	polyethylenglycol
PI	propidium iodide
PSF	point-spread function
px	pixel
ROI	region of interest
RT	room temperature
s	second
s.d.	standard deviation
SE	surface equivalents SLB
supported lipid bilayer	
SNR	signal-to-noise ratio
SMFM	single-molecule fluorescence microscopy
SMLM	single-molecule localization microscopy
SOPC	1-stearoyl-2-oleoyl-sn-glycero-3-phosphocholine
SPT	single-particle tracking
STED	stimulated emission depletion
STORM	stochastic optical reconstruction microscopy
SUV	small unilamellar vesicle
T	temperature
TDB	trypanosoma dilution buffer
TFA	trifluoro acetic acid
V	Volt
VS	vinylsulfone
VSG	variant surface glycoprotein
v/v	volume per volume
w/v	weight per volume

6.3 List of figures

6.4 List of tables

6.5 Publication list

Teile dieser Arbeit sind in folgenden Publikationen enthalten:

Hartel A. J. W., Glogger M., Guigas G., Jones N. G., Fenz S.F., Weiss M. and Engstler M. (2015). The molecular size of the extra-membrane domain influences the diffusion of the GPI-anchored VSG on the trypanosome plasma membrane. *Sci. Rep.* , **5**: 10394; doi: 10.1038/srep10394

Contribution: Performed parts of the experimental research, involved in data analysis

Hartel A. J. W., Glogger M., Jones N. G., Abuillan W., Batram C., Hermann A., Fenz S. F., Tanaka M. and Engstler M. (2016). N-glycosylation enables high lateral mobility of GPI-anchored proteins at a molecular crowding threshold. *Nat. Commun.*, 3 (**7**): 12870 doi: 10.1038/ncomms12870

Contribution: Performed parts of the experimental research, involved in data analysis and writing of the publication

Glogger M., Subota I., Pezzarossa A., Denecke A. L. Carrington M., Fenz S. F. and Engstler M. (2017). Facilitating trypanosome imaging. *Exp. Parasitol.*, **180**: 13-18

Contribution: Performed the experimental research and data analysis. Involved in writing the publication together with co-authors

Glogger M., Stichler S., Subota I., Bertlein S., Spindler M. C., Teßmar J., Groll J., Engstler M. and Fenz S. F. (2017). Live-cell super-resolution imaging of intrinsically fast moving flagellates. *J. Phys. D:Appl. Phys.*, 50 (**7**): 074004 (7pp)

Contribution: Performed the experimental research and data analysis. Involved in writing the publication together with co-authors

Bartossek T., Jones N. G., Schäfer C., Cvitković M., Glogger M., Mott H. R., Kuper J., Brennich M., Carrington M., Smith A.S., Fenz S., Kisker C. and Engstler M. (2017). Structural basis for the shielding function of the dynamic trypanosome variant surface glycoprotein coat. *Nat. Microbiol.*, **2**: 1523-1532

Contribution: Performed parts of the experimental research, involved in data analysis